The Pennsylvania State University

The Graduate School

Department of Astronomy and Astrophysics

GRAVITATIONAL WAVE RADIATION FROM THE GROWTH OF SUPERMASSIVE BLACK HOLES

A Thesis in

Astronomy and Astrophysics

by

Miroslav Micic

Submitted in Partial Fulfillment
of the Requirements
for the Degree of

Doctor of Philosophy

December 2007

The thesis of Miroslav Micic was read and approved* by the following:

Steinn Sigurdsson
Associate Professor of Astronomy and Astrophysics
Thesis Adviser
Chair of Committee

Kelly Holley-Bockelmann
Senior Research Associate
Special Member

Donald Schneider
Professor of Astronomy and Astrophysics

Robin Ciardullo
Professor of Astronomy and Astrophysics

Jane Charlton
Professor of Astronomy and Astrophysics

Ben Owen
Assistant Professor of Physics

Lawrence Ramsey
Professor of Astronomy and Astrophysics
Head of the Department of Astronomy and Astrophysics

---

*Signatures on file in the Graduate School.

Abstract

Understanding how seed black holes grow into intermediate and supermassive black holes (IMBHs and SMBHs, respectively) has important implications for the duty-cycle of active galactic nuclei (AGN), galaxy evolution, and gravitational wave astronomy. Primordial stars are likely to be very massive $\geq$30 $M_\odot$, form in isolation, and will likely leave black holes as remnants in the centers of their host dark matter halos. We expect primordial stars to form in halos in the mass range $10^6 - 10^{10}\,M_\odot$. Some of these early black holes, formed at redshifts $z \gtrsim 10$, could be the seed black hole for a significant fraction of the supermassive black holes found in galaxies in the local universe. If the black hole descendants of the primordial stars exist, their mergers with nearby supermassive black holes may be a prime candidate for long wavelength gravitational wave detectors. We simulate formation and evolution of dark matter halos in ΛCDM universe. We seed high-redshift dark matter halos with early black holes, and explore the merger history of the host halos and the implications of black hole's kick velocities arising from their coalescence. The central concentration of low mass early black holes in present day galaxies is reduced if they experience even moderate kicks of tens of $\mathrm{km\,s^{-1}}$. Even such modest kicks allow the black holes to leave their parent halo, which consequently leads to dynamical friction being less effective on the low mass black holes that were ejected, compared to those still embedded in their parent halos. Therefore, merger rates with central supermassive black holes in the largest halos may be reduced by more than an order of magnitude. Using analytical and illustrative cosmological N–body simulations, we quantify the role of kicks on the merger rates of black holes formed from massive metal free stars with supermassive black holes in present day galaxies.

Most studies of the cosmological growth and merger history of black holes have used semianalytic models and have concentrated on SMBH growth in luminous galaxies. We have developed a "hybrid method" that combines high resolution cosmological N-body simulations for the halos' merger history, with semi-analytical recipes for BH pair dynamics and BH gas accretion. We track the assembly of black holes over a large range of final masses – from seed black holes to SMBHs – over widely varying dynamical histories. We used the dynamics of dark matter halos to track the evolution of seed black holes in three different gas accretion scenarios. We have found that growth of a Sagittarius A* - size SMBH reaches its maximum mass M_{SMBH}=$\sim 10^6$ $M_\odot$ at $z \sim 6$ through early gaseous accretion episodes, after which it stays at near constant mass. At the same redshift, the duty-cycle of the host AGN ends, hence redshift z=6 marks the transition from an AGN to a starburst galaxy which eventually becomes the Milky Way. By tracking black hole growth as a function of time and mass, we estimate that the IMBH merger rate reaches a maximum of R_{max}=55 yr^{-1} at z=11. From IMBH merger rates we calculate the number density of ultra-luminous X-ray sources (ULX) to be N_{ULX}=7 per Milky Way type galaxy per redshift in redshift range $2 \lesssim z \lesssim 6$.

We model gravitational wave signatures for various SMBH growth scenarios and find that the future gravitational observatory LISA, will be able to detect mergers of massive black holes up to redshift z=5. We also analyse how the merger rate changes if various suppression mechanisms are implemented in merger rates and find that low seed formation rate will substantially decrease the overall merger rate to ~ 10 per year; low efficiency in dynamical friction will influence low redshift merger rates; and gravitational recoil from the mergers will eject high redshift black holes from their host halos. All three suppression mechanisms combined reduce merger rate to ~ 1 per year.

Table of Contents

List of Figures

Acknowledgments

This thesis presents the research that was born in Fall 2002 when professors Steinn Sigurdsson and Tom Abel formulated an ambitious six credits Fall Project for me. I am eternally grateful to both of them for everything but mostly for the infinite amount of support and computational power provided to me. I would also like to thank Kelly-Holley Bockelmann who together with Steinn Sigurdsson is responsible for shaping and directing my researh into this thesis in the last two years.

I would like to thank NASA's Columbia High End Computing program for a generous time allocation, and the Center for Gravitational Wave Physics at Pennsylvania State University for sponsoring this research. This research was supported by a grant from the NSF, PHY 02-03046 and from NASA's ATP NNG04GU99G.

At the end I thank my thesis committee, professors Jane Charlton, Donald Schneider, Robin Ciardullo and Ben Owen and thanks to the entire Department of Astronomy & Astrophysics.

Chapter 1

Introduction

1.1 Cosmological Structure Formation

The universe was conceived in the moment of cosmic singularity that we call "Big Bang". At that moment, the universe was in a state of infinite density and infinite curvature, hence, physics can not be applied nor it can be applied until after the Planck time, $t_p \sim 10^{-43}$ s after the Big Bang. Standard Big Bang (SBB) cosmology describes the cosmological evolution at late times (after the period of nucleosynthesis).

One of the biggest successes of SBB cosmology is the prediction of the existence and black body nature of Cosmic Microwave Background (CMB). Observations and measurements of the CMB radiation by COBE (COsmic Background Explorer) show an almost isotropic blackbody radiation with temperature $T_{CMB} = 2.726 \pm 0.010$ K (Mather et al. 1994) (the universe is very smooth on large scales (200 Mpc)) and show temperature anisotropies on angular scales of $\sim 90^\circ$ (Smoot et al. 1992) (the universe is inhomogeneous on small scales represented by planets, stars, galaxies, clusters and superclusters of galaxies). Structures are not uniformly distributed. There are regions of space almost totally devoid of galaxies and high density regions. Although SBB cosmology predicts the CMB radiation, it fails in explaining the spatial flatness of the universe (the flatness problem), the isotropy of CMB to an accuracy of better than 10^{-4} (the horizon problem), the inhomogeneities in the distribution of matter and the small CMB anisotropies (the structure formation problem) and the reason the entropy is large (the entropy problem) (Guth 1981).

Inflationary cosmology (Guth 1981) provides solutions to these problems. Starting with the Robertson-Walker metric, which geometrically describes the homogeneous and isotropic universe:

$$ds^2 = dt^2 - a(t)^2 d\mathbf{x}^2 \tag{1.1}$$

where a(t) is a scale factor. Applying Einstein's equations to it, we can establish the evolution equations for the scale factor a(t):

$$\frac{\dot{a}^2}{a^2} = 8\pi G\rho \tag{1.2}$$

and

$$\frac{\ddot{a}}{a} = -4\pi G(\rho + 3p) \tag{1.3}$$

For $p = -\rho$, the expansion is exponential, $a(t) \sim e^{t/t_f}$, where $t_f \sim 10^{-38}$ s. The universe expands exponentially for a brief period of time, and, at the end of this inflationary period, it is highly homogeneous on large scales, but is locally perturbed as a consequence of quantum fluctuations (Guth 2004).

One second after the Big Bang the synthesis of the light elements starts. In the first three minutes of this radiation-dominated era, light elements D, ^{3}He, ^{4}He, ^{7}Li are synthesized with abundances from ^{4}He/H $\sim$ 0.08 down to ^{7}Li/H $\sim 10^{-10}$ (Olive et al. 2000).

Structures form in the gravitational instability scenario where primordial density perturbations grow through the gravitational Jeans instability. These perturbations originate in the inflation model and the inflationary prediction is that the perturbation field is a Gaussian random field. Inflation also predicts that fluctuations keep growing at the same rate at all times, and that the shape of the power spectrum remains similar to the primordial one, $P(k) \sim k^{n_s} \sim k^1$, where n_s is the spectral index of the primordial density fluctuation. WMAP (Bennett et al. 2003) measured the spectral index, obtaining $n_s = 0.99 \pm 0.04$, and did not detect deviations from gaussianity. Both results are in agreement with inflationary predictions.

The cosmological model adopted today is the ΛCDM model (Spergel et al. 2007; Riess et al. 2001), in which dark matter is composed of cold, weakly interacting, massive particles. This model is specified by: density of the universe, $\Omega_0 = \Omega_m + \Omega_\Lambda$ (where $\Omega_m = 0.3$ and $\Omega_\Lambda = 0.7$ are the contribution from matter and vacuum, respectively), the Hubble constant, $H_0 = 100h$ km s^{-1} per Mpc, baryon density Ω_b =0.04, the rms mass fluctuations on a 8h^{-1} Mpc scale $\sigma_8 = 0.9$, and $n_s = 1$. On large scales, the power spectrum is a pure power-law which follows a simple linear evolution of perturbations. On small scales, perturbations grow non-linearly and this growth is controlled by the σ_8 parameter.

The first objects that grow through non-linear perturbations are those consisting of dark matter, since dark matter is made of collisionless particles that interact very weakly with the rest of matter and with the radiation field (Zwicky 1933; Rubin et al. 1980; Lynden-Bell et al. 1988). The self-gravity of dark matter in overdense regions eventually wins against the expansion of the universe, dark matter collapses, experiences a violent relaxation and quickly reaches virial equilibrium forming bound objects called dark matter halos (DMH) (Bardeen et al. 1986; Eisenstein & Loeb 1995; Sheth et al. 2001). The inner structure of DMH has been investigated through numerical simulations by Navarro et al. (1997) who have found that DMH density profiles have a universal shape, independent of the halo mass, the initial density fluctuation spectrum and the cosmological parameters. The violent relaxation process builds the inner structure of halos with a shallow density profile while the secondary accretion gives rise to a steep outer density profile (Ciardi & Ferrara 2005).

Dark matter halos are the only objects forming as long as the gas is ionized. Recombination (the time at which the electron fraction has dropped to 0.1) occurs at $z_{rec}\sim1250$ and neutral atomic hydrogen forms. When nearly neutral matter decouples from the radiation, perturbations in the gas component finally start growing at the centers of already formed dark matter halos (Peebles 1993). Next, the gaseous component virializes in a way similar to the virialization of dark matter and the first bound gas objects form (Fig. 1.1). During the collapse, the gas develops shocks and gets reheated to a temperature at which pressure support can prevent further collapse. At the same time, dynamical friction acting on clumps of gas, dissipates their orbital energy and deposits it in the dark matter, which gets heated and pushed away from the center (El-Zant et al. 2001; Moore 1994; Flores & Primack 1994).

The mass of the first bound gaseous objects is the Jeans mass which represents only the minimum mass that is able to collapse. This mass is the mass within the radius where competing pressure and gravitational forces cancel (Jeans 1928). This is a necessary but not sufficient condition for collapse. It is also necessary to require that the atomic/molecular cooling time is shorter than the Hubble time so that gas can continue to collapse through cooling until stars are formed. Considering the primordial composition of the gas and low temperatures, the main coolant is molecular hydrogen. When H_2 collides with another H_2 or H atom it gets rotationally or vibrationally excited and the following radiative deexcitation leads to cooling (Lepp & Shull 1984; Hollenbach & McKee 1989; Martin et al. 1996; Galli & Palla 1998). Objects formed in this manner are called Population III objects and their collapse ends with the formation of at least one star at redshifts $z \gtrsim 12$ (Haiman et al. 1996, 1997; Abel et al. 1997; Tegmark et al. 1997; Abel et al. 1998; Omukai & Nishi 1999; Abel et al. 2000).

1.2 Population III stars

First stars or Pop III stars are metal-free stars since they form out of primordial gas. Pop III stars are expected to contribute to the reionization of the universe, formation of the first galaxies, formation of supermassive black holes, etc.

Since the first generation stars form out of pure H/He gas, the relevant physics is significantly simplified. Nevertheless, the collapse and the fragmentation of a primordial gas cloud is still not fully understood which makes it harder to understand the initial mass function (IMF) of the first stars. In general (Schneider et al. 2002), the gas cools and possibly fragments. The mass of the each fragment is approximately the Jeans mass or larger. The fragmentation stops when cooling becomes inefficient because below the critical temperature, at the relevant densities, the emissivity of the gas is low (there are no transitions that provide strong radiation emission in metal free gas). As the subsequent contraction proceeds adiabatically, the temperature increases.

Smooth Particle Hydrodynamics (SPH) simulations by Bromm et al. (1999) and 3D adaptive mesh refinement (AMR) simulations by Abel et al. (2000) reached a similar conclusion that the first protostar forms with mass $\sim 200\,M_\odot$. Since than, various groups (Nakamura & Umemura 2001; Uehara & Inutsuka 2000; Omukai 2000; Ripamonti et al. 2002) tried to better understand fragmentation in order to constrain the mass range for the first stars. Since the core of the first star is surrounded by a reservoir of gas (corresponding to the mass of the initial clump), the protostar can grow by several orders of magnitude in mass by accreting the envelope matter and reach the mass range $30\ M_\odot \lesssim M \lesssim 300\ M_\odot$ (Tan & McKee 2004; Yoshida et al. 2006; O'Shea & Norman 2007). Fig. 1.2 shows the first star forming region in the latest simulation performed with the AMR code called ENZO (Smith & Sigurdsson 2007; Smith et al. 2007).

The primordial fragmentation process is still very poorly understood, hence the IMF of the first stars is still very uncertain. Depending on the density of the collapsing cloud, the IMF could have two peaks at $\sim 10^2$ and $1\ M_\odot$ (Nakamura & Umemura 2001).

If the radiation field from the first stars is included, H_2 in the rest of the cloud would get depleted and the resulting IMF would have peaks at $\sim$40 and 0.3 $M_\odot$ (Omukai & Yoshii 2003). As the first stars, after their death, enrich the gas with metals (Smith & Sigurdsson 2007), more efficient fragmentation produces stars with significantly lower masses as observed in the present-day IMF (Bromm et al. 2001a; Schneider et al. 2002).

Since the first stars are metal free, their energy source is restricted to proton-proton burning. Consequently, they are hotter and live shorter ($\sim$ 3 Myrs) than present-day stars (Bromm et al. 2001b; Tumlinson et al. 2003; Schaerer 2002, 2003). The final fate of the first stars depends on their mass. Stars with masses $10\ M_\odot \lesssim M_* \lesssim 40\ M_\odot$ go through the proton-proton chain and the triple-α process, followed by a supernovae explosion and collapse into a black hole (Woosley & Weaver 1995; Fryer 1999). Stars with $40\ M_\odot \lesssim M_* \lesssim 100\ M_\odot$ collapse into a black hole which could be followed by a jet, and possibly a gamma ray burst (GRB) (Fryer 1999). Stars with $100\ M_\odot \lesssim M_* \lesssim 260\ M_\odot$ form large He cores (Portinari et al. 1998) and encounter the electron-positron pair instability which results in a giant nuclear-powered explosion with no remnant for $M_* \lesssim 140\ M_\odot$ (Fryer et al. 2001). Stars with $M_* \gtrsim 140\ M_\odot$ collapse into a massive black hole after they use up all the energy in photodisintegration instability (Fryer et al. 2001; Bond et al. 1984).

The first stars form at very high redshift $10 \lesssim z \lesssim 50$. They form either in $T_{vir} \lesssim 10^4$ K dark matter halos through H_2 cooling, or in $T_{vir} \gtrsim 10^4$ K halos (which corresponds to $M_{vir} \gtrsim 10^8\ M_\odot[(1+z)/10]^{-1.5}$) through hydrogen atomic line cooling. Being very hot, Pop III stars create a background of UV radiation which photodissociates H_2 molecules, located in the first stars birthplaces. Hence, the formation of new metal free stars is suppressed by the UV radiation from the previous generation of stars (Dekel & Rees 1987; Haiman et al. 1997, 2000; Machacek et al. 2001). Since the first star's IMF is unknown, Wise & Abel (2005) calculated the first star's supernovae rates (primordial SN rate) assuming fixed primordial stellar mass of 100, 200, and 500 $M_\odot$ including the varying star formation efficiency and probability for radiation to escape and ionize the IGM. They predict that the primordial SN rate peaks at $z \sim 14$ - 20 (Wise & Abel 2005). The combination of an increasing UV background reionizing universe, and the disruption of minihalos from primordial SN suppresses all primordial star formation and it ceases at $z\sim$ 10 - 12. Therefore, there are no new massive black hole seeds at $z \lesssim 12$.

If the growth of supermassive black holes we observe today needs to start with a seed black hole, the mechanism described in the previous paragraphs is the most probable theoretical scenario for the formation of seeds. Seeds are expected to be massive since no mass loss is expected for most of the collapsing Pop III stars. Exceptions are at $\sim$ 100 - 140 $M_\odot$ where the pulsational pair-instability ejects the outer layers of the star before it collapses, and above $\sim$ 500 $M_\odot$ where pulsational instabilities in red supergiants may lead to significant mass loss. The hydrogen-rich envelope and parts of the helium core are ejected in a supernova explosion.

1.3 Buildup of Supermassive Black Hole

All of the first stars that form with mass above 260 $M_\odot$ die after $\sim$ 3 Myr and leave massive black holes as their remnants. These black holes are the potential seeds for the later formation of supermassive black holes and they initially contain at least half of the initial stellar mass (Fryer et al. 2001). They form either at the centers of dark matter halos or close to them at z $\gtrsim$ 12 sinking to the gravitational potential of their host halos. As dark matter halos merge later into larger and larger structures, massive black holes at their centers cluster in the cores of more massive halos formed by subsequent mergers (Madau & Rees 2001). If clustering of massive black holes at the centers of halos leads to their merger and an intermediate mass black hole, and if halos experience multiple mergers during their lifetime, than the end product of those mergers could be the supermassive black holes we observe today (Volonteri et al. 2003). Indirect evidence for this scenario can be found in the strong link between the masses of SMBHs and the gravitational potential wells that host them, in particular the dynamics of the stellar component in galaxies, e.g., the remarkably tight correlation between the stellar velocity dispersion of the host bulge and black hole mass (Ferrarese & Merritt 2000; Gebhardt et al. 2000). Another reason it is believed that the structure and kinematics of galactic nuclei are relics of the merger process (Merritt 2004) is the fact that smaller galaxies have steeper stellar cusps naturally formed by SMBH pulling stars in (Peebles 1972), while larger galaxies have shallower cusps as the result of galaxy mergers (Merritt 2004).

Two important questions in the the previously described scenario of SMBH growth are the efficiency of forming massive black holes binaries and the efficiency of gas accretion onto the black hole. The first one can be divided into three phases (Begelman et al. 1980) assuming that every dark matter halo in the merger, hosts a galaxy with a SMBH/IMBH at its center: 1. After galaxies merge, the SMBHs sink toward the center of the new galaxy via dynamical friction; 2. The binary continues to decay via gravitational slingshot interactions (Saslaw et al. 1974) in which stars on orbits intersecting the binary are ejected at velocities comparable to the binary's orbital velocity, while the binary's binding energy increases. 3. If the binary's separation decreases to the point where the emission of gravitational waves becomes efficient at carrying away the last remaining angular momentum, the MBHs coalesce rapidly (more on gravitational radiation in the following section). The transition from (2) to (3) marks the "final parsec problem" (Milosavljević & Merritt 2003b). A black hole binary will quickly eject all stars on intersecting orbits, thus cutting off the supply of stars. Other mechanisms for extracting energy and angular momentum from a binary have been introduced: accretion of gas onto the binary system (Armitage & Natarajan 2002), refilling of the loss cone via star-star encounters (Yu 2002; Milosavljević & Merritt 2003a), and triaxial distortions (Merritt & Poon 2004; Holley-Bockelmann & Sigurdsson 2006).

Observations also support the argument that coalescence occurs relatively quickly, since there would be more examples of multiple X-Ray source at the centers of galaxies. The fact is that although there are examples of "dual SMBHs" (two widely separated supermassive black holes in a single system) (Komossa 2003), none are at separations below 1 kpc, even though a 1 kpc separation would be resolvable at distances of several hundred Mpc. One of the examples of a dual SMBH is in this case of a pair of interacting galaxies near the center of the galaxy cluster Abell 400. The associated radio source 3C75 consists of a pair of twin radio cores separated by $\sim$ 7 kpc (Owen et al. 1985). Many galaxies in the late stages of a merger have double nuclei. One clear example is NGC

6240 (Komossa et al. 2003) where nuclei are separated by $\sim$ 1.4 kpc, as well as NGC 5643 with nuclei separated by $\sim$ 1.8 kpc (Guainazzi et al. 2004).

1.3.1 SMBH Growth by Gas Accretion

Mergers of massive black holes alone are not enough to account for the entire growth of a supermassive black hole (Kauffmann & Haehnelt 2000). This is especially true in the cases of high luminosity quasars at high redshift, e.g., $M_{SMBH} = 3 \times 10^9$ $M_\odot$ in the quasar SDSS 1148+5251 at redshift z=6.43 (Fan et al. 2003; Willott et al. 2003). Various models of gas and dark matter accretion have been introduced to explain the rapid SMBH growth including: 1. Direct formation of a SMBH through the collapse of large gas clouds ($M \gtrsim 10^5$ $M_\odot$); 2. Massive seed black holes either from the collapse of supermassive stars (Shapiro 2004) or from the accretion of low angular momentum baryons in the early Universe (Koushiappas et al. 2004); 3. More frequent black hole mergers (Yoo & Miralda-Escudé 2004; Shapiro 2005); 4. Rapid mass growth via a sustained super-Eddington accretion (Ruszkowski & Begelman 2003; Volonteri & Rees 2005); and 5. Sustained accretion of self-interacting dark matter (SIDM) particles (Ostriker 2000; Spergel & Steinhardt 2000; Hu et al. 2006) onto a seed black hole followed by sustained baryon accretion at the Eddington limit. While most of these models are more or less speculative, sustained Eddington accretion of baryons is the most probable mechanism during the quasar phase of the SMBH (Soltan 1982). In that case, the mass growth rate is $\dot{M}_{\rm BH}=M_{\rm BH}/t_{\rm Sal}$, where $t_{\rm Sal}$ is the Salpeter time-scale, $t_{\rm Sal}{\sim}4{\times}10^7$ yr (Hu et al. 2006).

1.3.2 Intermediate Mass Black Holes

Intermediate mass black holes are considered to be a missing link between massive and supermassive black holes. The natural environment for IMBH is AGNs in dwarf galaxies but their observation is very difficult, both by kinematics, since their gravitational influence is small, and from their possible AGN activity, since the expected luminosity is weak. A good candidate is NGC 4395 (Filippenko & Ho 2003), where the BH mass is likely to be 10^4 - 10^5 $M_\odot$ (radiating much below the Eddington limit). The difficulty of this search is that dwarf galaxies frequently host nuclear star clusters of 10^6 $M_\odot$, hiding the weak AGN. They are best observed in the Local Group; a famous example, M33, does not host any BH more massive than 10^3 $M_\odot$ (Gebhardt et al. 2001b). At the same time, the globular cluster G1 in M31 has a 1.8×10^4 $M_\odot$ black hole (Gebhardt et al. 2005) with 97% significance. There are two conclusions of great importance that involve the G1 globular cluster. First, there is evidence for a disrupted galaxy centered on the G1 (Ibata et al. 2005). Also, compared to other globular clusters, G1 has the highest measured velocity dispersion. These are observational arguments that G1 is a stripped nucleus of a dwarf galaxy that has been tidally disrupted by a merger with the M31 galaxy, thus confirming the current picture of structure formation. Second, there are no obvious differences between the surface brightness profiles of G1 and the nucleus of M33. It is clear that the data for G1, compared to that of M33's nucleus, would favor the presence of a black hole. One way of explaining this difference is that a M33's IMBH has been kicked out of the nucleus through gravitational recoil (kick) after a IMBH/IMBH merger, although this conclusion is highly speculative. The coalescence of massive black hole binaries under gravitational radiation may give the resulting black holes a significant kick velocity (Fitchett 1983; Fitchett & Detweiler 1984; Wiseman 1992; Favata et al. 2004; Blanchet et al. 2005; Baker et al. 2006; Damour & Gopakumar 2006).

Ultraluminous X-ray sources (ULX) are also candidates for hosts of intermediate mass black holes. They have been detected in nearby galaxies by Chandra (Zezas & Fabbiano 2002; Kong et al. 2005) and XMM-Newton (Foschini et al. 2002), but these measurements depend on uncertain models for accretion disks, and stellar-mass black hole models may fit as well (King et al. 2001). ULXs are off center (from the nucleus) X-ray sources with 0.5 - 8.0 keV luminosities exceeding 10^{39} ergs s^{-1} (Colbert & Ptak 2002). Because of the increase in the observed global star formation rate with redshift (Madau et al. 1998; Ghosh & White 2001) and the increase in the mean X-ray luminosity for field galaxies (Hornschemeier et al. 2002) with redshift, it is expected that the number of ULXs will increase too, since ULXs are associated with a regions of star formation. An intermediate mass black hole can form in the ULX either as a remnant of a Pop III star (Madau & Rees 2001), or through runaway merging of young stars in sufficiently dense globular clusters (Portegies Zwart et al. 2004; Gürkan et al. 2004; Freitag et al. 2006). We will show that the first process becomes very important at higher redshifts z $\sim$ 2 - 6, and if ULX sources form in this manner, they could substantially contribute to the X-ray luminosity of distant, star-forming galaxies such as Lyman break galaxies (LBGs). In that case, it has been estimated that the average LBG would have $\sim$ 510 off-nuclear sources each with $L_x \sim 10^{39.9}$ ergs s^{-1}. Generation-X is the proposed future X-ray mission with subarcsecond imaging capabilities. It will be able to observe these kind of objects with offset of $\sim$ 0.6 kpc at z $\sim$ 4 (Lehmer et al. 2006).

1.3.3 Mechanisms for SMBH Growth Suppression

Most of the SMBH growth is expected to come from gas accretion (Soltan 1982), but black hole mergers dominate SMBH growth at higher redshifts (Micic et al. 2007). Hence, it is of great importance to understand the efficiency of the mergers of seed black holes. As mentioned in the previous paragraph, mergers of massive black holes might be followed by kicks. These recoils are caused by anisotropic emission of gravitational waves which carry away linear momentum. Recent work in numerical relativity leads to an estimate that the expected recoil is below 200 $\mathrm{km\,s^{-1}}$ for Schwarzschild, i.e., nonspinning, black holes (González et al. 2007a), and a similar range is expected for black holes with low spin, or with spins (anti)aligned (Herrmann et al. 2007) with the orbital axis. However, when the spin vectors have opposite directions and are in the orbital plane, the recoil velocity can be as large as a few thousand kilometers per second (Campanelli et al. 2007b,a; González et al. 2007b).

The gravitational potential of dark matter halos increase with decreasing redshift and the escape velocity from the center of dark matter halos is $v_{esc} \sim 100\ \mathrm{km\,s^{-1}}$ for $M_{halo} \sim 10^9\ M_\odot$ at z $\sim$ 8 (Micic et al. 2006). Mergers of seed black holes are the dominant mechanism for black hole growth at z $\gtrsim$ 8 where the escape velocity from dark matter halos is lower than 100 $\mathrm{km\,s^{-1}}$. If the magnitude of the kick is larger than the escape velocity, the final black hole after coalescence will be ejected from its host halo.

One of the unknowns in models of SMBH growth that include seed black holes is the first stars' IMF. It is important to know how many first stars are in the mass range that produces seed black holes. If the IMF is not top heavy, the fraction of first stars that produce a black hole will be small and dark matter halos will not be seeded. This effect, combined with kicks substantially reduce the contribution of mergers to the SMBH growth.

1.3.4 Growth of Structures Through Analytical Methods

The hierarchical "bottom-up" mechanism of structure formation, where dark matter halos merge to form larger bound objects is statistically treated in the Extended Press-Schechter (EPS) theory (Press & Schechter 1974; Lacey & Cole 1993). EPS combines the Press-Schechter (PS) (Press & Schechter 1974) halo mass function with the halo merger rates derived by (Lacey & Cole 1993).

If a halo at redshift z_0 has mass M_0 (parent), this mass was distributed within smaller halos (progenitors) in the range M to $M + dM$ at earlier times. The ratio of the density at which a halo is virialized to the background density in the universe at a specific redshift is called the critical overdensity ($\delta_c(z)$ at z and $\delta_c(z_0)$ at z_0). The number of progenitors of halo mass M is then:

$$\frac{dN}{dM}(z = z_0) = \frac{1}{\sqrt{2\pi}} \frac{M_0}{M} \frac{1}{S^{3/2}} \frac{d\delta_c}{dz} \frac{d\sigma_M^2}{dM} \delta z. \tag{1.4}$$

where σ_M^2 is the linear theory rms density fluctuations smoothed with a 'top-hat' filter of mass M at redshift z, and $S \equiv \sigma_M^2(z) - \sigma_{M_0}^2(z)$ (Bower 1991; Lacey & Cole 1993).

Volonteri et al. (2003) uses this expression to build a binary merger tree (each halo has exactly two progenitors in Δz time). The tree starts from the present day and runs backward in time 'disintegrating' a parent halo into its progenitors until progenitors reach the mass resolution $\mathrm{M}_{\mathrm{res}}$ set as initial parameter. For halos with $M \lesssim M_{\mathrm{res}}$, the number of progenitors with $M_{\mathrm{res}} \lesssim \mathrm{M} \lesssim \mathrm{M}_0$ is:

$$N_p = \int_{M_{\mathrm{res}}}^{M_0} \frac{dN}{dM} \, dM, \tag{1.5}$$

The fundamental EPS limitation is that the EPS halo mass function over-predicts the number of dark matter structures and is mathematically inconsistent (Erickcek et al. 2006). Beside the above, mostly technical, issue of constructing the DMH merger tree, another more physical problem appears.

SMBH merger rates also depend on the method used to seed a DMH. Both the mass ranges used to seed dark matter halos with massive black holes and the redshift ranges at which the seeding took place, defined in an ad hoc way, with little physical motivation. As the result, many EPS based works calculate substantially different merger rates which span over three orders of magnitude.

DMH in the EPS approach can not lose mass. Each halo can be identified as a progenitor of a single halo at the next output line. In reality, halos can lose mass. Tidal forces by nearby halos and ejections through mergers of halos are just two examples how some particles can be found beyond the boundary of the halo at the next time-step. Consequently, halos can not be treated as a simple combination of their two progenitors. As mentioned before, the merger tree constructed in EPS is a binary tree based on the assumption that all mergers during Δz are binary mergers. In reality two or more halos can merge simultaneously and form one halo during Δz, or, the halo does not have to go through merger at all. All of this makes the approach that uses numerical simulations more accurate in studying the evolution of galaxies. With numerical simulations, the evolution of density fluctuations is followed in complete generality, since besides cosmological parameters, there are no other constraints placed on formation of halos, the DMH shape, tidal effects, or number of mergers. The problem is that the resolution of the numerical simulations needs to be high, so that the dynamics can be followed as generally as possible. High resolution simulations are computationally very expensive ($\sim$ 100,000 CPU). More on numerical simulations is presented in section 1.5.

1.4 Gravitational Wave Radiation

Assuming that the first stars were very massive and leave black holes as remnants, the gravitational waves emitted during each collapse (Schneider et al. 2000; Fryer et al. 2002) would be seen as a stochastic background, with spectral strain h $\sim 10^{20}$ - 10^{19} Hz$^{-1/2}$ in the frequency range 5×10^{-4} - 5×10^{-3} Hz, and might be detected by LISA (Laser Interferometer Space Antenna) (Fig. 1.4).

After the collapse of the first stars, when their remnants (massive black holes) form hard binaries at the centers of dark matter halos, the last remaining angular momentum is carried away by the gravitational waves during a coalescence. These gravitational waves are detectable by space-based interferometers (LISA) with high SNR $\sim 10^4$. The process of coalescence can be divided up into three phases: inspiral, merger and ringdown. Gravitational waves emitted during adiabatic inspiral (described by the post-Newtonian approximation to general relativity Blanchet (2003)) carry information about the masses and spins of the two black holes, some of the orbital elements of the binary, and the distance to the binary (Thorne 1989, 1995b). At the end of inspiral, black holes go through free-falling plunge (Kidder et al. 1993; Ori & Thorne 2000; Lai & Wiseman 1996). This is the merger phase and the gravitational waves from this phase may be rich in information about the dynamics of relativistic gravity in a highly nonlinear, highly dynamic regime. The final stages of the merger (when the final black hole is formed) can be described as oscillations of this final black hole's quasinormal modes (Teukolsky & Press 1974; Chandrasekhar & Detweiler 1975) with the strongest mode for l=m=2. The waves from the ringdown carry information about the mass and spin of the final black hole and these waves are described by using perturbation theory on the Kerr spacetime background (Chandrasekhar 1984).

LISA is a future space observatory ($\sim$ 2017) for the detection of gravitational waves at frequencies (below 10 Hz) which can not be detected on Earth since they fall in the range of seismic noise. LISA will consist of three pairs of interferometers in the vertices of an equilateral triangle. The arm length is 5×10^6 kilometers for the purposes of detecting $\sim$ 1 mHz gravitational waves (Araújo et al. 2007) (Fig. 1.5). It will be primarily guided by the interplanetary gravitational field, i.e., the field of the Sun and the other solar system bodies in the optimized configuration: the three spacecraft constellation rotates clockwise around its barycenter with a period of one year, while the barycenter follows the ecliptic 20° behind the Earth (45 million kilometers) (Araújo et al. 2007). The plane of the three satellites is inclined 60° relative to the ecliptic. LISA is thus not pointing to a fixed location. Each of the three spacecrafts will be in an orbit which is very circular (eccentricity = 0.01), and inclined 1° to the ecliptic. LISA measures changes in the path length between the spacecrafts due to the motion of the mirrors induced by the oscillations of gravitational radiation. This leads to the shift in the fringes of the interferometer due to time delay.

Gravitational radiation from the coalescence of massive black holes will be a prime signal for LISA. The maximum rest frame frequency f_r, occurs when the black hole binary is in a circular orbit at 3 Schwarzschild Radii:

$$f_{max} = \frac{c^3}{14.7\pi G}\frac{(M_1+M_2)^{1/2}}{M_1^{3/2}} \tag{1.6}$$

where M_1, and M_2 are the black hole masses, G is the gravitational constant, and c is the speed of light. The minimum f_{min} is:

$$f_{min} = \frac{1}{\pi}\frac{G(M_1+M_2)^{1/2}}{a_{gw}^3} \tag{1.7}$$

where $a_{gw} \lesssim 0.2$ pc is the binary separation where gravitational radiation dominates, expressed by:

$$a_{gw} = 0.0014\text{pc}[\frac{M_1M_2(M_1+M_2)}{10^{18.3}{M_\odot}^3}]^{1/4}{t_g}^{1/4} \tag{1.8}$$

where ${t_g}^{1/4}$ is the coalescence timescale in Gyr ($t_g \sim 1$ Gyr). The change in the rest frame frequency is:

$$\dot{f_r} = \frac{96}{5}{f_r}^{5/3}\frac{G^3M_1M_2(M_1+M_2)}{c^5a^3}[\frac{G(M_1+M_2)}{\pi^2}]^{-1/3} \tag{1.9}$$

Thus, for each merger at a comoving distance d(z), gravitational radiation is emitted with a characteristic strain, $h_c(f_r)$

$$h_c(f_r) = \frac{8\pi^{2/3}G^{5/3}{M_{chirp}}^{5/3}{f_r}^{2/3}}{10^{1/2}c^4d(z)} \tag{1.10}$$

where $\mathrm{M_{chirp}} = (\mathrm{M_1M_2})^{3/5}(\mathrm{M_1}+\mathrm{M_2})^{-1/5}$ and $h_c \sim 10^{-17}$.

LISA has a low-frequency window (10^{-4} Hz $\lesssim$ f $\lesssim$ 0.1 Hz) (Araújo et al. 2007). The main sources of gravitational waves will be massive black hole binaries in the range 10^3 $M_\odot \lesssim m \lesssim 10^7$ $M_\odot$. With a 3 year observation, LISA will resolve the Gravitational Wave Background (GWB) into discrete sources including binaries caught in their final inspiraling phase. It is expected that most of the observable events will be at redshifts 2 $\lesssim$ z $\lesssim$ 7 (Sesana et al. 2004). This means that LISA can be used to map the distribution of black holes as the universe evolves.

1.5 Numerical Methods

Numerical simulations are a powerful tool for studying the formation and evolution of structures in the universe (dark matter halos, galaxy clusters, galaxies, intergalactic gas, etc.). Initially, numerical simulations depended on the direct summation method for the gravitational N-body problem (Peebles 1970; White 1976, 1978; Aarseth et al. 1979), but the computational cost increases rapidly with large N. More recently, new techniques have been developed to deal more efficiently with large particle numbers: PM, P^3M, and AP^3M codes use direct N-body summation on small-scales, and compute the large-scale gravitational field by means of Fourier techniques (Bertschinger & Gelb 1991; Couchman 1991; Efstathiou et al. 1985; Hockney & Eastwood 1981; Hohl 1978; Macfarland et al. 1998); tree algorithms arrange particles in groups, and compute the gravitational force at a given point by summing over multipole expansions of these groups (Barnes & Hut 1986; Jernigan & Porter 1989). PM and tree algorithms have also been combined into tree-PM codes (Bode et al. 2000; Xu 1995). Simulations incorporate gas dynamics through properties of fluid dynamics in SPH simulations (Smoothed Particle Hydrodynamics) (Lucy 1977; Gingold & Monaghan 1977) and AMR simulations (Adaptive Mesh Refinement) (Klein et al. 1999; Norman & Bryan 1999).

1.5.1 Generating Initial Conditions

As mentioned in Section 1.1, the homogeneous and isotropic universe is described with a Robertson-Walker metric upon which perturbations of dark matter and baryons, specified as a power spectrum, are imposed. The inflation model predicts that linear fluctuations in the density of dark matter and baryons appear at the epoch of decoupling and that these fluctuations obey Gaussian statistics. Gaussian fluctuations are fully specified by the single function, the power spectrum P(k).

The first step in creating a Gaussian density field is to specify a power spectrum at redshift z in a matter dominated era:

$$\frac{k^3}{2\pi^2}P(k,z) = (\frac{ck}{H_0})^{3+n}\delta_H^2 T^2(k) D_g^2(z)/D_g^2(0) \tag{1.11}$$

where the function T(k) describes the processing of the initial density perturbations during the radiation dominated era (Padmanabhan 1993), $D_g(z)$ is the linear growth factor (Peebles 1980), and δ_H is the amplitude of density fluctuations. δ_H is obtained from observations the CMB.

Density fluctuations in k space will have complex values, $\delta_k = Ae^{i\Theta}$, where the amplitude A is randomly selected from P(k) with R as a uniform random number in the interval [0,1]:

$$A = (-\log R \times P(k))^{1/2} \tag{1.12}$$

and phase Θ is randomly selected uniformly from $[0,2\pi]$.

Next, the Fourier transform of δ_k is performed on the cubic grid with N^3 points, giving δ_x, the density fluctuations at each grid point. The physical dark matter density is then:

$$\rho_{DM}(x) = (1 + \delta_x(x))\rho_{DM.mean}, \tag{1.13}$$

where $\rho_{DM.mean}$ is the mean dark matter density in the simulation. As mentioned in section 1.1, perturbations in baryon density behave the same way as perturbations in dark matter, so:

$$\rho_b(x) = \frac{\Omega_{DM}}{\Omega b}\rho_{DM}(x) \tag{1.14}$$

where Ω_{DM} and Ω_b were defined in section 1.1.

The last step is to perturb the actual dark matter particles so that they reflect the density fluctuations previously described. This is done by using the Zeldovich approximation for positions:

$$x = q + D(a)\psi(q) \tag{1.15}$$

and velocities:

$$v = aHfD\psi \tag{1.16}$$

where vectors x and v are the positions and velocities of the particles, q are the old grid positions, a is the cosmological scale factor, f = dlnD/dlna, and ψ is the displacement field:

$$\Delta\psi = -\frac{\delta_x}{D(t)} \tag{1.17}$$

In this manner, the initial positions and velocities are set for dark matter particles (or baryons) at some higher redshift. The simulation starts with these initial conditions and is performed by the code GADGET described in the following section.

1.5.2 GADGET

Different versions and combinations of these codes have been used in cosmology. One of the most widely used cosmological N-body codes is GADGET (GAlaxies with Dark matter and Gas intEracT) (Springel et al. 2001b). GADGET has a broad range of scientific applications, from studies of self-gravitating systems which include gas, to cosmological N-body/SPH simulations. There are two versions of this code. One is serial and it uses for gravity calculations either a tree algorithm or GRAPE (described in the last subsection). The parallel version works with a tree code only.

All the simulations we report in this thesis have been conducted with the cosmological N-body tree method in GADGET. Dark matter in GADGET is modeled as collisionless self-gravitating particles. Gas is modeled with SPH but we are not using this part of the code. Particle dynamics are followed by implementing Newton's equations of motion for a large number of particles. At small separations between particles, the softening length is introduced to prevent large-angle scattering in two-body collisions, hence, the softening length defines the spatial resolution in the simulation.

GADGET uses Barnes & Hut (1986) tree construction. In the tree algorithm, particles are arranged in a hierarchy of cubes called nodes. Each cube splits into eight smaller cubes, each with half the side length of the parent cube. Each node has either one particle only, or it hosts more nodes (Fig. 1.3). When the gravitational force on a particular particle is computed, the particle asks the node a question: Are you close enough for direct force calculation or are you far enough for multipole expansion? An opening criterion (r $\gtrsim$ l/θ) controls whether the node is far enough for multipole expansion, where r is the distance to the node, l is the size of the node, and θ is a free parameter, also called the opening angle. In this manner, the gravitational force between close particles is calculated directly, while for distant particles, the force is calculated through multipole expansion. When multipole expansion is used instead of direct summation, the computational cost is reduced to order $\mathcal{O}(N \log N)$. Calculations are not allowed for particles separated by less then the softening length (h). If the code has more than one type of particle (i.e, when dark matter and stars need to be separated), different softening lengths are specified for each group. In this case, GADGET constructs separate trees for each species of particles. The performance does not change as long as the species are spatially separated.

For a group of particles with total mass M, center of mass $\vec{s}$, at the distance $\vec{r}$, the gravitational potential is expanded in a multipole series up to quadrupole order:

$$\vec{f}(\vec{r}) = G\left\{-\frac{M}{y^3}\vec{y} + \frac{3\mathbf{Q}}{y^5}\vec{y} - \frac{15}{2}\frac{\vec{y}^T\vec{Q}\vec{y}}{y^7}\vec{y} + \frac{3}{2}\frac{\mathbf{P}}{y^5}\vec{y}\right\}. \tag{1.18}$$

where $\vec{y}$=$\vec{r}$-$\vec{s}$ and the tensor terms of the multipole expansion (Springel et al. 2001b) are:

$$\mathbf{Q} = \sum_k m_k(\vec{x}_k - \vec{s})(\vec{x}_k - \vec{s})^T = \sum_k m_k\vec{x}_k\,\vec{x}_k^T - M\vec{s}\,\vec{s}^T, \tag{1.19}$$

and

$$\mathbf{P} = \mathbf{I}\sum_k m_k(\vec{x}_k - \vec{s})^2 = \mathbf{I}\left[\sum_k m_k\vec{x}_k^2 - M\vec{s}^2\right], \tag{1.20}$$

where $\mathbf{I}$ is the unit matrix .

Multipole expansion of the gravitational force in the tree algorithm provides fast calculations ($\mathcal{O}(N \log N)$), but if the number of particles is $\gtrsim 10^7$, the speed reduces to $\mathcal{O}(N)$. This is the result of the need for calculation of the node properties in double-precision while the storage of the results is in single-precision, for large numbers of particles.

Once the gravitational potential is calculated for all the nodes, the position of each particle can be evolved in time. If the timestep is Δt, the position of the particle at the middle of this timestep is:

$$\tilde{\vec{r}}^{(n+\frac{1}{2})} = \vec{r}^{(n)} + \vec{v}^{(n)}\frac{\Delta t}{2}, \tag{1.21}$$

and acceleration at this position is :

$$\vec{a}^{(n+\frac{1}{2})} = -\,\nabla\Phi|_{\tilde{\vec{r}}^{(n+\frac{1}{2})}}\,. \tag{1.22}$$

The velocity of the particle is then evolved as:

$$\vec{v}^{(n+1)} = \vec{v}^{(n)} + \vec{a}^{(n+\frac{1}{2})}\Delta t, \tag{1.23}$$

and position as:

$$\vec{r}^{(n+1)} = \vec{r}^{(n)} + \frac{1}{2}\left[\vec{v}^{(n)} + \vec{v}^{(n+1)}\right]\Delta t. \tag{1.24}$$

The timestep Δt for the collisionless dynamics in cosmological simulations is set to:

$$\Delta t = \frac{\mathrm{ErrV}}{a} \tag{1.25}$$

where ErrV=5 is some fraction of the typical velocity of the particle (with dimensions of velocity), and a is the intensity of the acceleration of the particle.

1.5.3 Analysis Tools

Output files which store information on particles masses, positions and velocities at desired redshifts are called snapshots. These are raw simulation data that need to be transformed into real physical objects which have counterparts in observations. We observe galaxies as either isolated objects or in mergers with other galaxies. We also observe galaxies as virialized objects. We use similar ideas to what defines a galaxy, to define structures in numerical simulations.

The most common method for identifying and defining structures (we focus on dark matter halos) in data from numerical simulations has been the Friend-Of-Friends algorithm (FOF) (Davis et al. 1985; Audit et al. 1998). FOF defines a group of particles to represent a single object when the separation between the neighbors is less than some fraction of the mean interparticle separation (l_{mean}). It links the particles with distances less than l_{FOF} which is usually set to $0.2 l_{mean}$. For a theoretical spherically symmetric object with an isothermal density profile, $l_{FOF} = 0.2$ gives a mean density contrast of 178 (Porciani et al. 2002), and this defines a virialized halo (overdensity criterion). The problem is that numerical objects are not spherical, hence, using $l_{FOF} = 0.2$ will produce a wide range of mean density contrasts for halos with various morphologies. The solution is to apply an overdensity criterion (Lacey & Cole 1994; Warren et al. 1992) independently by forming concentric spheres around the halo's density center, and looking for the sphere which encapsulates a mean density contrast of 178. $l_{FOF} = 0.2$ has been used traditionally (and wrongly) since Davis et al. (1985) introduced the FOF method. Although the method is correct, the value of the linking length depends on halo morphology which changes with redshift. It is also limited by the resolution of the simulation (the linking length must be larger than the softening length described in the previous subsection). The value of 0.2 for the linking length in Davis et al. (1985), was obtained from a low-resolution simulation (though it was the highest at that time). As the resolution in numerical simulations increased, it has become possible to decrease the linking length to ~ 0.1. Most of the cosmological simulations still focus on large scale structure formation where $l_{FOF} = 0.2$ is valid (i.e., clusters of galaxies). However, on smaller scales (high redshift halos $\lesssim 10^9$ M$_\odot$), where structures form in sheets and filaments, $l_{FOF} = 0.2$ is too large to separate elongated objects in the streams of unbound particles in the filaments (Gao et al. 2005). Hence, the FOF algorithm must always be used in combination with other halo finding methods, e.g, a spherical overdensity algorithm (SO) (Lacey & Cole 1994; Warren et al. 1992). Another argument for using l_{FOF} = 0.2 has come from EPS theory. The halo mass function obtained with l_{FOF} = 0.2 proved to be consistent with observations at low redshifts and mass functions obtained from EPS theory. However, very little is known about dark matter halos mass functions at high redshifts ($z \gtrsim 10$) and low masses ($M \lesssim 10^9\,M_\odot$), or about the validity of this linking length.

In the analysis of our simulations we combine two algorithms mentioned previously (FOF and SO) with a method for extracting gravitationally bound structures. P-GroupFinder is a parallel code for identifying halos and subhalos in large cosmological simulations. The code is a combination of the FOF and SUBFIND algorithms (Springel et al. 2001a). SUBFIND is applied to each FOF group where it looks for gravitationally bound substructures. SUBFIND starts by calculating a local estimate of the density for all particles in the group. If a local region is overdense, it is a candidate to be a substructure. Particles are then sorted in order of decreasing density. By comparing density and separation between pair of particles, the local density center is identified. All particles which are candidates for one subhalo are subjected to a self-boundedness requirement and all particles with positive total energy are eliminated until only bound particles remain. The subhalo's center is defined at the position of the center of mass and if more than a minimum number of particles ($\sim$ 32) in the subgroup survive the unbinding, these particles represent a subhalo.

1.5.4 GRAPE

GRAPE (GRAvity PipE) (Sugimoto et al. 1990; Makino & Taiji 1998) is hardware attached to a standard workstation for one purpose only, accelerating particles with Newtonian force. Since GRAPE chips are designed for only one specific purpose, this system has enormous computational speed which keeps direct summation competitive with pure software solutions. In a large-scale gravitational N-body calculations, almost all the instructions of the corresponding computer program are performed on a standard workstation, while only the gravitational force calculations, in the innermost loop, are replaced by a function call to the GRAPE.

There has been a constant improvement in performance with every new GRAPE system. The latest model is GRAPE6 (Makino et al. 2003) with a peak speed of 64Tflops (in comparison GRAPE1 has a speed of 240Mflops). Because of continuing development of tree algorithms, it has become obvious that GRAPE6, although computationally fast, is too expensive. By replacing direct N-body summation with a tree algorithm and GRAPE6 with a cluster of GRAPE6A boards (Fukushige et al. 2005), the production cost is minimized and the computing speed is optimized.

A 32-node GRAPE cluster at the Rochester Institute of Technology (RIT) is the largest facility of its kind in the USA. We have constructed a large N-body cosmological simulation with $\gtrsim 10^8$ particles in collaboration with Prof. David Merritt at RIT. This simulation is designed to test large cosmological volume ($\sim$ 100 Mpc) and broad dynamical range ($100\ M_\odot \lesssim M \lesssim 10^{13}\ M_\odot$) for evidence of "downsizing" in a build-up of SMBHs. The goal is to reproduce the AGN luminosity function for a range of SMBH masses ($10^6\ \mathrm{M}_\odot \lesssim \mathrm{M}_{\mathrm{SMBH}} \lesssim 10^{10}\ \mathrm{M}_\odot$) and study its behavior at various redshifts.

In the following chapter we will use cosmological N-body simulations to study the evolution of the first massive black holes on large cosmological scales and the possibility for formation of supermassive black holes at redshift z=1, if kicks from gravitational recoil are introduced to a large population of black holes at the redshift of their formation. In chapter 3. we address the problem of seeding dark matter halos with massive black holes. We study in detail the identification of dark matter halos and the redshift range for massive black hole formation, and introduce the new "hybrid method" that combines high resolution cosmological N-body simulations for the halos' merger history with semi-analytical recipes for BH pair dynamics and BH gas accretion. We track the assembly of black holes over a large range of final masses – from seed black holes to SMBHs – over widely varying dynamical histories and present the first numerical merger rates for massive black holes. In chapter 4. we reproduce the expected gravitational wave signal from the mergers of massive black holes in our simulation for various black hole growth scenarios. In particular, we show how well LISA observations will be able to distinguish between these scenarios. We also study the change in black hole merger rates and the expected gravitational signal when the mergers are suppressed by the efficiency in black hole formation, in kicks from gravitational recoil during mergers, and in the dynamical friction time scale for mergers of dark matter halos. Finally, in chapter 5. we discuss the results and future work.

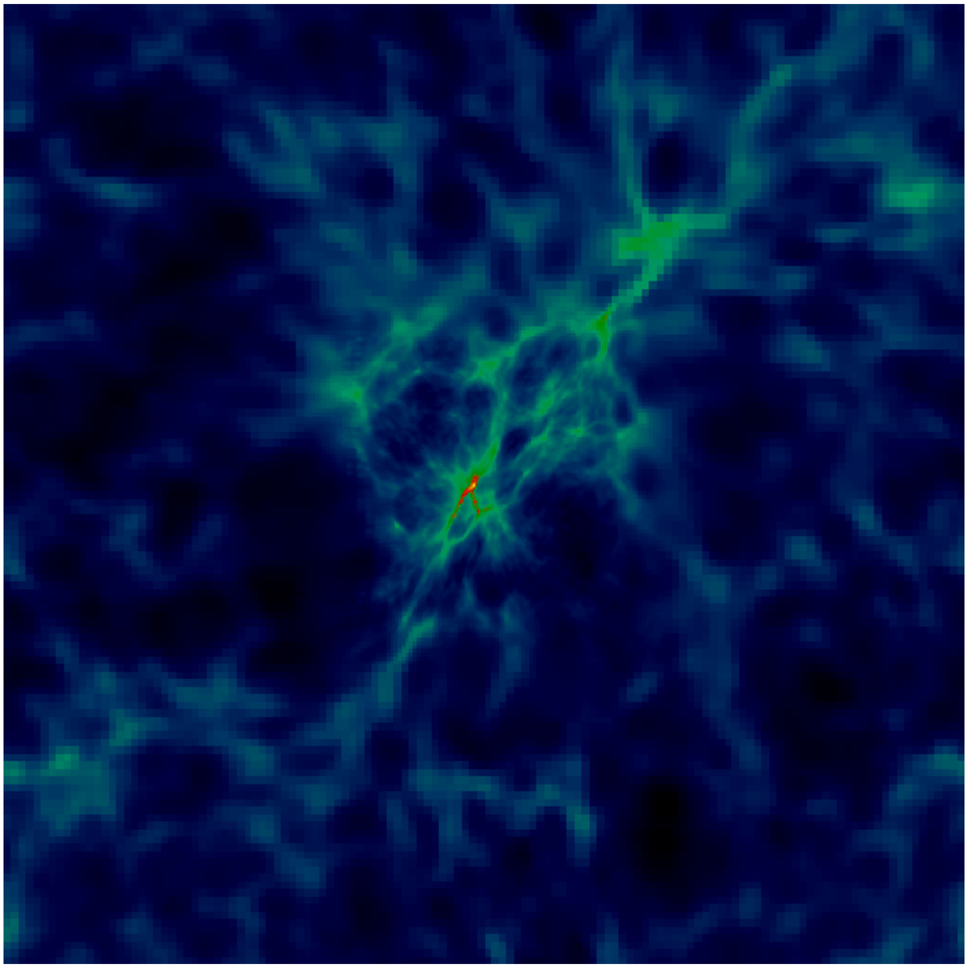

Fig. 1.1 Two dimensional density plot of first baryon structures forming at redshift z=24, courtesy of Britton D. Smith. Red indicates an H_2 cloud is forming at the center of a dark matter halo, the birthplace of the first stars. The simulation box is 17 kpc in length.

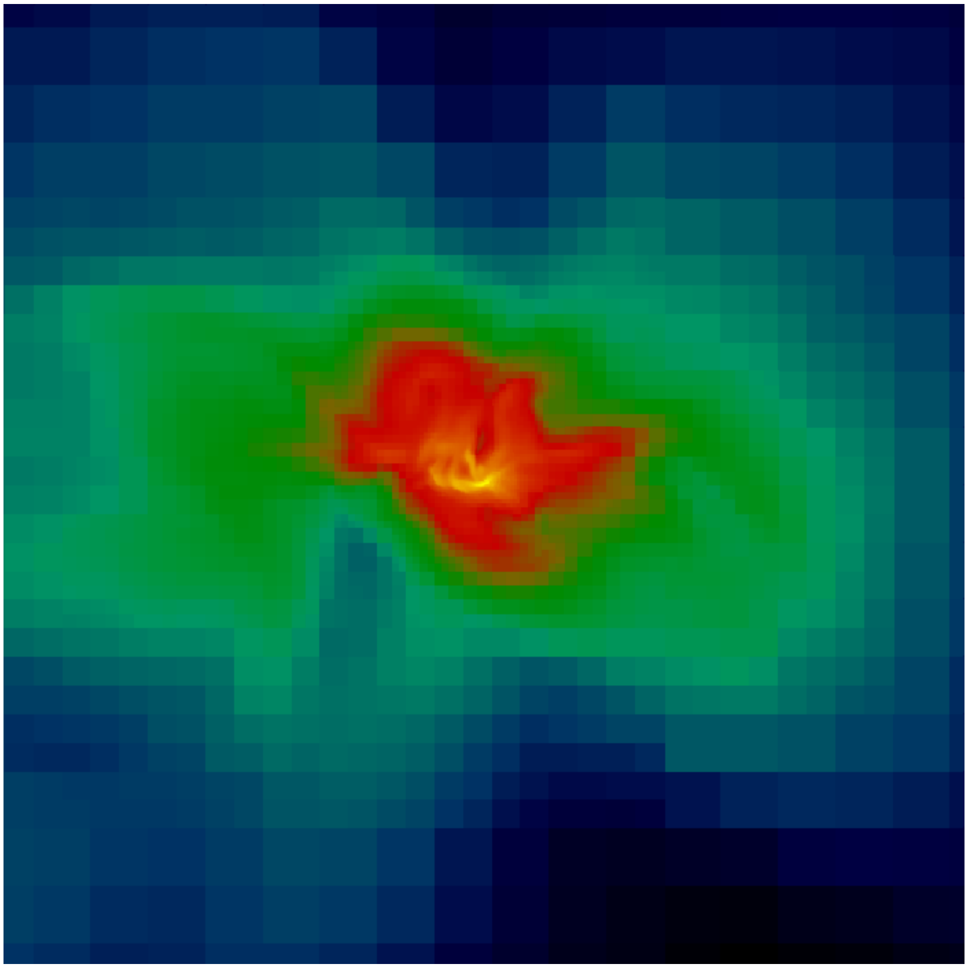

Fig. 1.2 Two dimensional density plot of the formation of a Population III star at redshift z=24 at the center of an H_2 cloud, courtesy of Britton D. Smith. The length of the box is 3,500 AU and the density at the center (yellow) is $\rho = 4 \times 10^{-13} \sim 10^{12}$ cm^{-1}.

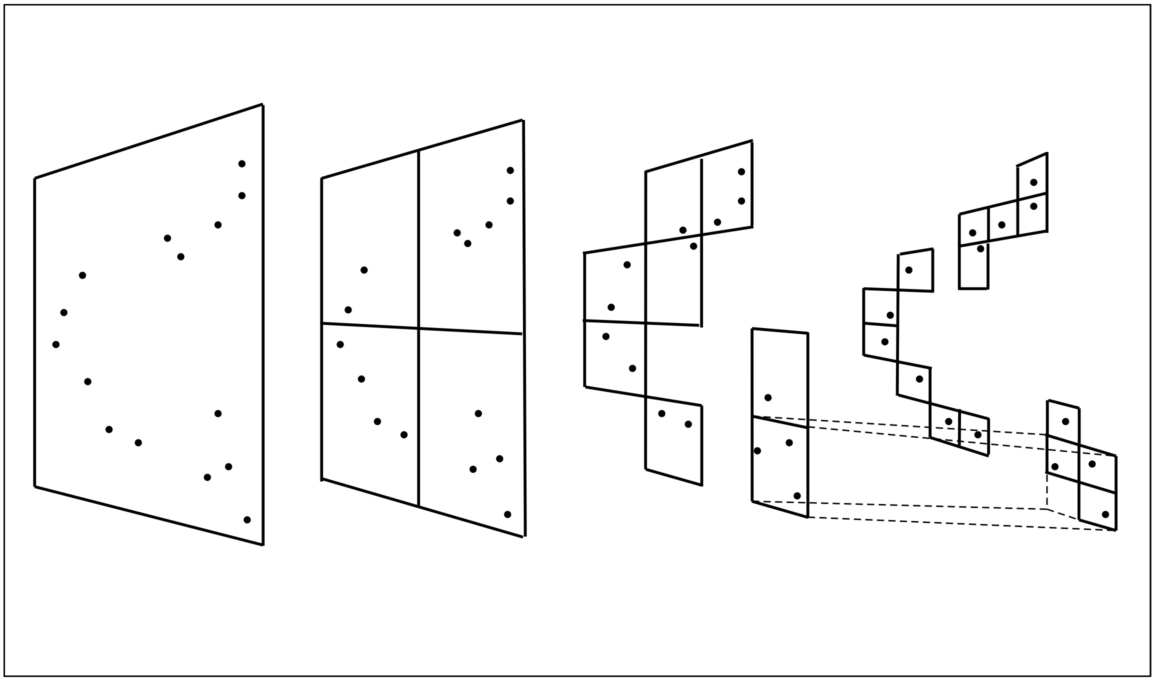

Fig. 1.3 Two dimensional illustration of tree structure used in GADGET. Each cube is subdivided into smaller cubes until there is only one particle left in each cube corresponding to the leaves of the tree.

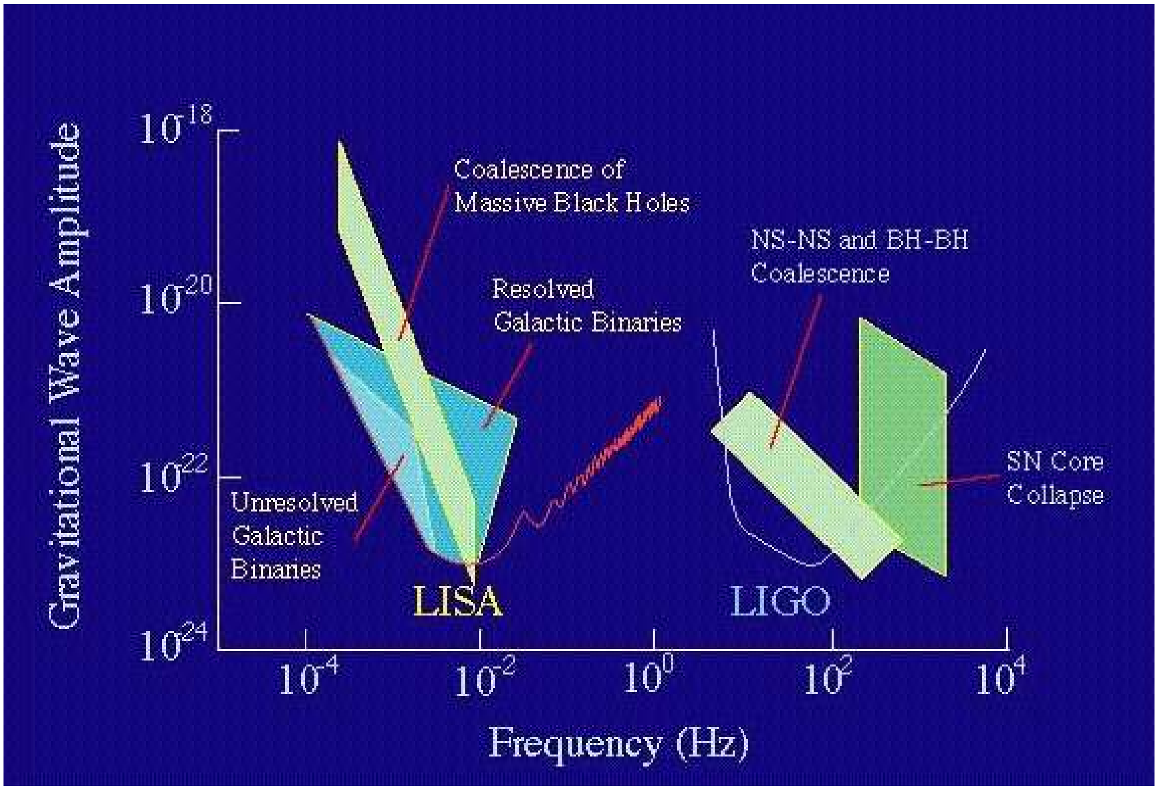

Fig. 1.4 LISA and LIGO sources, from http://imagine.gsfc.nasa.gov/. Mergers of massive, intermediate and supermassive black holes are in the LISA frequency range $10^{-4} \lesssim f \lesssim 10^{-2}$ with expected gravitational wave amplitude between 10^{-23} and 10^{-18}.

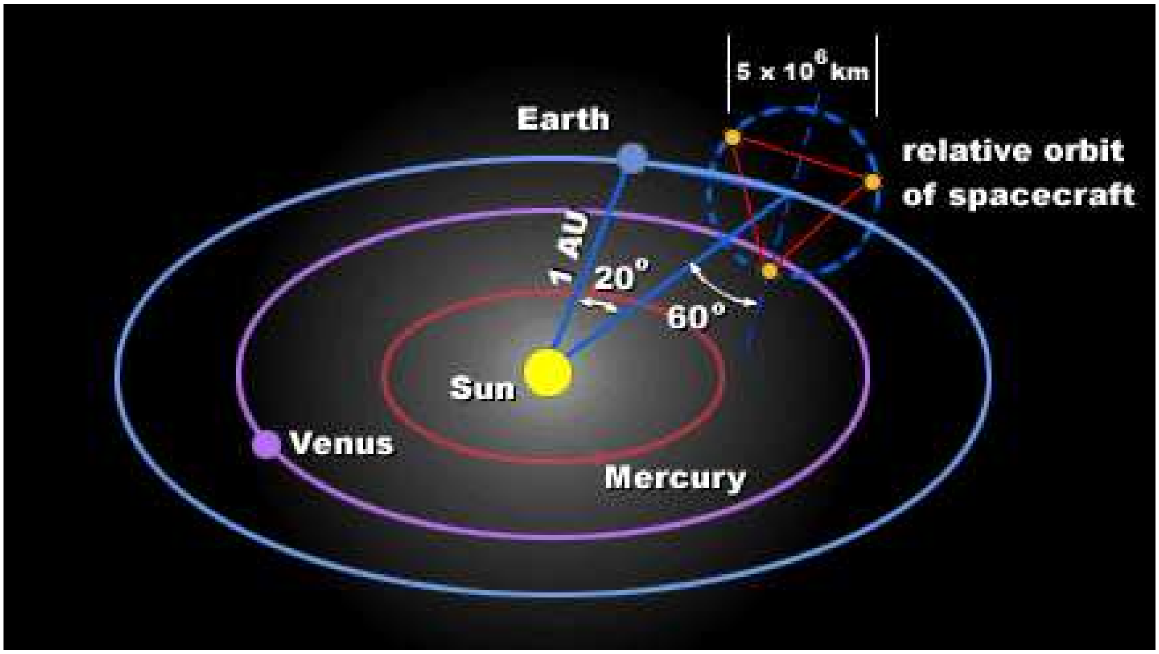

Fig. 1.5 LISA orbit specifications from http://lisa.nasa.gov/. Three spacecrafts in an equilateral triangle with the arm length of 5×10^6 kilometers will follow the Earth's orbit, trailing 20° behind (45 million kilometers).

Chapter 2

The Role Of Primordial Kicks on Black Hole Merger Rates

This chapter has been published as paper “The role of primordial kicks on black hole merger rates”, Micic, M., Abel, T., Sigurdsson, S., 2006, MNRAS, 372, 1540M.

Work described in this chapter predates recent works in numerical relativity which gave us a new insight in gravitational recoil placing the value for kicks to be as large as 4000 km−1. However, the arguments about orbital configuration of black hole binary (Bogdanović et al. 2007) reduces expected kick magnitude significantly. Hence, our work is relevant.

2.1 MOTIVATION

It is firmly established that most galaxies have super-massive black holes (SMBH) at their centers. Their observed masses are in the range 10^6 $M_\odot \lesssim M \lesssim 10^9$ $M_\odot$ and it appears that there are correlations (Kormendy & Gebhardt 2001; Gerhard 2001) between their masses and the bulk properties of the galactic bulges hosting them (Laor 2001; Merritt & Ferrarese 2001a; Tremaine et al. 2002; Gebhardt et al. 2001a; Graham et al. 2001). These correlations point to a link between the formation of SMBHs and the evolution of their hosts. It also appears that SMBHs are linked to the properties of the host dark matter halos (Buyle et al. 2004). If the SMBH precursors were present from very early on, then their mergers, together with growth by accretion, could account for the abundance of the SMBHs today (Soltan 1982; Schneider et al. 2002).

Ab initio numerical simulations of the formation of the first luminous objects within the standard structure formation framework, finds that metal free stars form in isolation, and may have masses 30 $M_\odot \lesssim m \lesssim 300$ $M_\odot$ (Abel et al. 2000, 2002; Bromm et al. 2002). In current models of structure formation, dark matter initially dominates and pregalactic objects form from small initial density perturbations. As they assemble via hierarchical merging, the metal-free primordial gas cools slowly through the rotational lines of hydrogen molecules. As the gas cools, it sinks to the center of the dark matter potential well. However, as the cooling rates are small, the clumps fail to fragment as they collapse. This leads to a top-heavy initial stellar mass function (IMF) and to the production of very massive stars, unlike the modern stellar IMF which declines rapidly with increasing mass.

Metal-free, high mass Population III stars lose only a small fraction of their mass in their lifetime of $\sim$3 Myr. This suggests that a large population of primordial massive black holes (MBH, with mass $\lesssim 10^3 M_\odot$) could be an end product of such pregalactic star formation (Heger et al. 2003). Since they form in rare high-σ density peaks (Couchman & Rees 1986; Madau & Rees 2001), relic MBHs are predicted to cluster in the cores of more massive halos (Abel et al. 2002) which in turn are formed by subsequent mergers of the original parent dark matter halos. It has been suggested (Volonteri et al. 2003; Islam et al. 2003) that mergers of massive halos and clustering of these MBHs should start at redshifts as large as z$\sim$20. Subsequent growth of MBHs would proceed through accretion of baryonic gas and coalescence, possibly leading to the formation of intermediate mass black holes (IMBH, with mass in range 10^3 $M_\odot \lesssim m \lesssim 10^6$ $M_\odot$). In the most optimistic scenario (Haiman & Loeb 2001), 10^9 $M_\odot$ black holes could form as early as z$\sim$10.

Here we will explore the evolution of the seed black hole in dark matter halos. Mergers of dark matter halos hosting at least one black hole (Bromm & Loeb 2003) at high redshift form black hole binaries, and their subsequent coalescence under gravitational radiation may give them a significant kick velocity (Fitchett 1983; Fitchett & Detweiler 1984; Wiseman 1992; Favata et al. 2004; Blanchet et al. 2005; Baker et al. 2006; Damour & Gopakumar 2006).. These recoils are caused by anisotropic emission of gravitational waves which carry away linear momentum. The recoil velocity is highly controversial requiring full general relativistic calculations. However, recent estimates place most recoils in the range 10-100 $\mathrm{km\,s^{-1}}$, although kicks of a few hundred $\mathrm{km\,s^{-1}}$ are not unexpected, and the largest recoils should not be above 500 $\mathrm{km\,s^{-1}}$ (Favata et al.

2004; Blanchet et al. 2005; Baker et al. 2006). Recent works in numerical relativity calculate kicks to be as large as 4000 $\mathrm{km\,s^{-1}}$ (Campanelli et al. 2007b). The amplitude of the kick determines if the black hole will be ejected from its host dark matter halo. Even the most massive dark matter halo at redshift $z \geq 11$ can not retain a black hole that receives $\geq 150\ \mathrm{km\,s^{-1}}$ kick, while at redshift of $z \geq 8$, kicks of 300 $\mathrm{km\,s^{-1}}$ are required to cause ejection (Merritt et al. (2004), Fig 3.). This is valid for black holes with masses $10^3\ \mathrm{M_\odot} \lesssim \mathrm{m} \lesssim 10^8\ \mathrm{M_\odot}$. Kicks of 40 $\mathrm{km\,s^{-1}}$ at high redshift should be sufficient to: eject IMBHs from globular clusters; displace IMBHs from the centers of dwarf galaxies; and perhaps provide a sufficient population of IMBHs for merging at the centers of spiral galaxies (Merritt et al. 2004).

We use N-body TREEcode simulations (GADGET; Springel et al. (2001b)) to investigate the *observational implications* of black hole kicks through the asymmetric emission of gravitational radiation during the merger. In this academic exercise, we assume that Population III stars collapse to form massive black holes at high redshifts. These black holes grow through gas accretion and mergers at the centers of dark matter halos. We use collisionless particles at the centers of dark matter halos as tracers of IMBHs. If kicks are important, the growth of IMBHs into supermassive black hole will be suppressed. We test two extreme scenarios for this behaviour and whether there are predictable consequences. In the first scenario, kicks do not occur in any dark matter halo at any redshift. In the second, kicks occur in every dark matter halo at an initial redshift and we introduce a prescription for assigning kicks to our tracer particles. As a result, these two scenarios set limits to the IMBHs' merger rate. The first scenario provides a maximum merger rate, and the second scenario provides a lower bound on the merger rate (the absolute lower bound is that no mergers occur, for example if black hole formation is suppressed and primordial stars leave no compact remnants). A better approach would be to track every individual merger, and assign kicks when mergers occur. We will explore this in later chapter. Our approach is computationally less expensive and provides only constraints. We have chosen z=8 as an initial redshift for assigning kicks to our tracers for IMBHs. At redshift $z{\sim}12$ supernovae rates for Pop III stars fall to zero (Wise & Abel 2005). The massive black holes resulting from Pop III collapse have already settled in the centers of dark matter halos by redshift $z{\sim}8$, the initial redshift for kicks. As mentioned before we are calculating constraints for the merger rates and not studying individual mergers. The MBH tracers are tracked from the initial to the final redshift and used to quantify the changes in distributions of IMBHs in these two scenarios. Through detailed analysis of their trajectories, we study how IMBHs respond to the dynamical evolution of dark matter halos, testing extreme ranges of outcome to check for the plausible scope for detection. Our results also apply to black holes ejected by the gravitational slingshot mechanism. The slingshot velocities fall in the recoil range (Aarseth 2005).

Our numerical simulations are followed by an analytical treatment of dynamical friction. As long as the dark matter halos have a bound core with density greater than the local galactic density and have "many" particles in them, the numerical dynamical friction will mimic "real" dynamical friction with reasonable fidelity (Vine & Sigurdsson 1998). If the halo density becomes smaller than the local galactic density, or if the secondary halo structure is down to being resolved by only "few" bound particles, then the dynamical friction prescription breaks down and relaxation due to numerical noise and large scale potential fluctuations dominate; integration of the dynamical friction term then becomes meaningless. This happens basically where we stop the simulations, and that is where we analytically estimate a conservative lifetime to coalescence.

We are exploring the effects of kicks on IMBH merger rates and the formation of SMBHs that are detected in the nuclei of luminous galaxies. Knowledge of IMBH merger rates is essential for the future experiments such as LISA (Danzmann 2003) and BBO (Big Bang Observer) (Crowder & Cornish 2005). LISA will be able to study much of the last year of inspiral of IMBH into SMBHs, as well as the waves from the final collision and coalescence of IMBH binaries. For binary black holes with masses in the range $100\,\mathrm{M}_\odot \lesssim \mathrm{M} \lesssim 10^4\,\mathrm{M}_\odot$, LISA can observe the last few years of inspiral, but not the final collision even at cosmological distances. Equal-mass black hole binaries enter LISA's frequency band roughly 1000 years before their final coalescence, independent of their masses, for the range $100\,\mathrm{M}_\odot \lesssim \mathrm{M} \lesssim 10^6\,\mathrm{M}_\odot$ (Thorne 1995a; Cornish & Levin 2002; Vecchio et al. 2004). Third generation gravitational wave observatories, such as BBO mission will have arcsecond-arcminute precision in identifying and localizing every merging black hole binary independent of redshift, anywhere in the universe over the years to months before their actual merger. In combination with ground-based detectors at higher frequencies, BBO could measure the mass, angular momentum, and dynamic spacetime structure of these compact objects with unprecedented precision.

In §2.2 we present a straightforward analytical treatment of dynamical friction. In §2.3 we describe the simulation setup, the codes used for analysis, and present results for 3 different high resolution simulations with varying kick parameters for early black holes. In §2.4 we describe the post-merger evolution through dynamical friction based on the arguments in §2.2, before we conclude in §2.5.

2.2 ANALYTICAL EXPECTATIONS

Clustering of MBHs and their consequent mergers creates a population of IMBHs at the centers of dark matter halos. In this section we outline the physical principles acting on a seed black hole over one Hubble time. The early stages of the merger are driven by the hierarchical cold collapse of sub–halos (gravitationally bound substructures of larger dark matter halos) within a primary halo. We focus our analysis on the single dark matter halo that naturally emerges from the numerical simulations as the structure largest in mass in our simulation volume; hence, the primary halo. Subsequent dynamical evolution of the IMBH population occurs through dynamical friction, and secular orbital evolution in the presence of any residual triaxiality after virialization (Madau & Rees 2001; Holley-Bockelmann et al. 2001; Zhao et al. 2002).

We assume that IMBHs embedded in their parent sub–halos experience dynamical friction acting collectively upon the entire compact sub–halo containing the IMBH; at least until tidal stripping significantly reduces the effective sub–halo mass to that of the central mass only (Weinberg 1989; Vine & Sigurdsson 1998; White 1983; Holley-Bockelmann & Richstone 1999). Tidal dissolution becomes effective only where the density of the primary halo is comparable to that of the sub–halo. With characteristic length scales of $\sim 100\,\mathrm{pc}$ and masses of $\sim 10^6\,\mathrm{M}_\odot$, sub–halo densities are of order

$10^{0\pm1}\,\mathrm{M}_\odot/\,\mathrm{pc}^3$, and the primary halo density reaches such densities only in the inner few kpc, at radii r $\lesssim 0.01$ r_{vir} (Fig. 2.6).

The primary halo is well-approximated by a singular isothermal sphere for radii of order $0.1\,\mathrm{r}_{vir}$ (Madau & Rees 2001), the dispersion is near constant and isotropic over a range in radii, and the density profile is close to isothermal, with a steeper fall off at larger radii and flattening at smaller radii. Approximating density interior to r, the distance of the sub–halo from the center of the primary halo, with associated circular velocity v_c to the center of the halo, the density distribution is well fit with:

$$\rho(r) = \frac{\mathrm{v_c}^2}{4\pi \mathrm{G r}^2}. \tag{2.1}$$

The frictional force on a host-halo (Binney & Tremaine 1987) of mass M moving on a circular orbit is:

$$F = -0.428 \ln\Lambda \frac{\mathrm{GM}^2}{\mathrm{r}^2}, \tag{2.2}$$

where lnΛ is the usual Coulomb logarithm:

$$\Lambda = \frac{\mathrm{b_{max} v_c}^2}{\mathrm{G(M+m)}}, \tag{2.3}$$

and $\mathrm{b}_{max} \sim r_{vir}$ is the maximum impact parameter. For a circular orbit, the force is tangential and thus causes the host-halo to lose angular momentum per unit mass L at a rate:

$$\frac{dL}{dt} = -0.428 \ln\Lambda \frac{\mathrm{GM}}{\mathrm{r}}. \tag{2.4}$$

Trivially, taking the time derivative of the expression $\mathrm{L=rv}_c$, and substituting into equation (4) gives an upper bound on the timescale for dynamical friction to bring the sub–halo and associated IMBH to the primary halo center:

$$r\frac{dr}{dt} = -0.428 \ln\Lambda \frac{\mathrm{GM}}{\mathrm{v_c}}. \tag{2.5}$$

Using the mean density interior to r, the distance of the sub–halo of mass M from the center of the primary halo, with associated circular velocity v_c, the timescale for dynamical friction to bring the sub–halo and associated IMBH to the primary halo center (Binney & Tremaine 1987), Eq. 7.26) is:

$$t_{fric} = \frac{1.17}{\ln\Lambda}\frac{\mathrm{r^2 v_c}}{\mathrm{GM}}, \tag{2.6}$$

$\ln\Lambda = 10$ is the Coulomb logarithm ((Binney & Tremaine 1987), table 7.1).

This is a conservative estimate for the time scale for early stages of dynamical friction; the orbits of the sub–halos are not circular and can therefore sink faster than we estimate, and coupling of the dynamical friction to internal degrees of the sub–halo also accelerates the evolution, possibly by more then factor of two (Weinberg 1989; Vine & Sigurdsson 1998). At small radii, mass loss from tidal disruption becomes significant.

Nevertheless, we expect the IMBHs to continue sinking towards the center of the primary halo, once they get inside r $\leq$ 0.01 r_{vir}. Typical mass ratios of early black holes and their host halos are $\geq 10^{-4}$.

Consequently for kicks that expel the IMBH from its host-halo at large redshifts, the dynamical friction time scale is at least 10^4 times larger since the IMBH is not embedded in a bound sub-halo. From equation (1), we can calculate the radius, r_{sink}, that allows the sub–halo to sink to the center in less than a Hubble time for a given velocity dispersion and sub–halo mass. If every sub–halo carries one IMBH at its center, then the merger rate for IMBHs will be a function of the number of sub–halos inside r_{sink}. If kicks at higher redshifts supply an IMBH with enough velocity to escape from its sub–halo, the expected number of IMBHs at r $\leq r_{sink}$ will be smaller, leading to a significant decrease in the IMBH merger rate. We also note that, stopping the growth of IMBH via gas accretion (by ejection into lower density regions) changes the X-ray population predictions (Agol & Kamionkowski 2002). We illustrate these effects with N-body simulations in the following sections.

2.3 ILLUSTRATIVE SIMULATION

2.3.1 Simulation Setup

We simulated a 10^3 Mpc^3 comoving volume in a ΛCDM universe with Ω_M=0.3, Ω_Λ=0.7 and h=0.7 from redshift z=40 to z=1. From initially low resolution simulations we selected a halo with 1.52×10^{12} M$_\odot$ at redshift z=1. Around that halo we selected a sphere of 2 Mpc comoving radius in the initial conditions and reran the simulations from z=40. Using 128^3 on the top level and a refinement factor of 4 in the high resolution region, we attain 4.9×10^6 high-resolution particles (softening length 2 kpc comoving) for the simulation and 2.0×10^6 low-resolution particles (softening length 4 kpc comoving) in the rest of the box. The mass of each high resolution particle in these simulations is 8.85×10^5 M$_\odot$ and the mass of each low-resolution particle is 5.66×10^7 M$_\odot$.

2.3.2 Analysis Tools

Every snapshot consists of masses, positions, and velocities of all types of particles at a specific redshift. Plots of their positions show clumps of particles that need to be associated with real-world objects. We used the HOP algorithm (Eisenstein & Hut 1998) to divide the particles into distinct sets such that particles in individual high-density regions are grouped together and are separate from those in other regions. HOP assigns density estimates to each particle by using a Gaussian smoothing algorithm and then determines which of the particles has the highest density. Each particle is then associated with its highest density neighbour and the process continues to higher and higher densities until the highest density particle is reached. All particles that hop to the same maximum are placed into the same group. Every particle is assigned to one and only one group. We set a density threshold in order to distinguish between the dense halo and its surroundings and we cut out of the group all particles with densities less than 5% of the density of the densest particle. We define a halo as a group of more than

50 particles. The HOP output is a list of halos with IDs, coordinates, density of the densest particle, and number of particles in each halo.

Further analysis is performed by Ganyl, Gadget Analysis Code and P-GroupFinder (Springel et al. 2001a). Ganyl analyzes spherical profiles for GADGET data, taking both the list of centers from the HOP analysis and a snapshot of the particle data that matches it. It converts units from comoving to proper and sorts according to their gadget IDs. Then, it identifies the centers of mass in the snapshot, searches in expanding spherical shells until it finds the virial radius r_{200}, and thereafter calculates the total halo mass m_{200}, velocity dispersion, and angular momentum.

P-GroupFinder uses a different approach to find halos. The particle distribution is segmented into groups using the friends-of-friends (FOF) algorithm. A fraction of the mean interparticle separation is used as the linking length, and halos are defined with distance criteria only. Gravitationally self-bound substructures are then extracted from each FOF group by using the SUBFIND algorithm. The bound part of FOF halo counts as a subhalo as well, so every FOF halo has its bound counterpart.

The advantage of Ganyl is in its cosmological approach of defining halos using over-densities, but since Ganyl uses density centers from the HOP algorithm, it finds over-densities more than once for the same object thereby creating artificial halos. Since P-GroupFinder checks for the gravitationally bound structures, it can isolate artificial halos as real world objects. Virial radii in kpc are calculated from the total mass in particles and their values are slightly larger than virial radii calculated by Ganyl. We use P-GroupFinder to identify black holes as the most-bound particles in their host halos.

We construct a merger tree from all 33 snapshots. The most massive halo incorporates hundreds of subhalos inside its virial radius. We examine all mergers and select a sample of the most massive halos from each group of mergers together with a sample of isolated halos that do not merge. For this new list we locate the GADGET IDs for the particles at the centers of every halo, and, by tracing IDs in different snapshots, we identify coordinates and velocities to get trajectories.

Density plots were made with code provided by Naoki Yoshida that applies a spline SPH kernel to derived densities and then projects them along a specified axis to produce a two dimensional smoothed image.

2.3.3 Black Hole Trajectories

After identifying a large dark matter halo and its associated substructure, we can track the dynamical behaviour of the purported IMBHs in each halo. We follow the evolution of the IMBH population to estimate their final present day distribution.

We identify the most massive halo in our simulation (SIM1 from now on) at z=1. This halo (the "primary") has a virial radius R_{vir}=370 kpc and a virial mass $M_{vir} = 1.52 \times 10^{12}\ M_{\odot}$. We tracked the primary and its substructure as it assembled and tracked the mass and trajectories of the seed black holes.

If IMBHs are Pop III remnants, then by $z > 8$, enough time should have passed to allow an IMBH to sink to the center of every halo. From the simulation point of view this population can be selected by choosing the most-bound particle in all the halos identified by P-GroupFinder. There were 2869 dark matter halos with masses in range

10^7 $M_\odot \lesssim M \lesssim 10^{10}$ $M_\odot$, and we label the most bound particle in each halo as an IMBH. By connecting particles' coordinates through 33 snapshots, we obtain IMBHs trajectories from z=8.16 to z=1.00. From 2869 IMBHs at z=8.16, 1958 of them can be found inside the primary halo at z=1.00. Fig. 2.1 shows a density plot of XY-projection of the SIM1 box at z=8.16. Density peaks (in yellow) are the centers of dark matter halos selected by P-GroupFinder (labeled as IMBH). The trajectories of the IMBHs for the most massive 100 halos as they spiral inside the primary halo, is overplotted. It is suggested (Miralda-Escudé & Gould 2000) that clusters of IMBHs might exist inside the inner kpc of every galaxy, spiraling towards the SMBH at the center. Our results are consistent with that point of view.

2.3.4 Black Hole Kick Velocity

As mentioned in the introduction, coalescence accompanied by gravitational radiation may give an IMBH a significant kick velocity. To explore the effect of such kicks on the underlying distribution of IMBH masses, velocities, and occupation fraction within forming galaxies, we model these kicks using existing estimates in current literature (Favata et al. 2004). We model the distribution of kicks with a truncated Gaussian in the interval $\{0, 150\}$ $\mathrm{km\,s^{-1}}$, with a mean kick of 75 $\mathrm{km\,s^{-1}}$. Recall that by IMBH, we are referring to the 2869 particles which are located at the centers of sub–halos at $z = 8.16$; 3/4 of which are destined to eventually merge with the primary halo in the absence of kicks. This sets an upper limit to the number of IMBHs within this representative large dark matter halo.

We add this presumed kick velocity, with a random direction, to the velocity of the IMBH at $z = 8.16$. In this way, we create a new snapshot file with changed velocities for the group of black holes only. We use this snapshot file as an initial condition file for a new simulation (SIM2a from now on) that starts at $z = 8.16$ to examine the differences in trajectories of the IMBH particle, with and without kick velocities. The same procedure was repeated for a different kick velocity interval $\{125, 275\}$ $\mathrm{km\,s^{-1}}$, with a mean kick of 200 $\mathrm{km\,s^{-1}}$ which was used for simulation - SIM2b. These are the most likely ranges suggested in related works (Favata et al. 2004).

Notice the fundamental difference between SIM1 and SIM2. In the case without kicks, black holes embedded in subhalos reach the center of the primary halo as dynamical friction siphons energy from the subhalo orbit. The main contribution to this process comes from the total mass of their halos which remain mostly bound throughout our simulation. In SIM2, IMBHs are generally ejected from their subhalos. Dynamical friction is not efficient on a black hole once it is stripped from a halo, due to its much lower mass (Hansen & Milosavljević 2003; Gerhard 2001; Portegies Zwart et al. 2003). Fig. 2.2 and Fig. 2.3 show the density plot of XY-projection of SIM2a box (middle) and SIM2b box (bottom) at redshift z=8.16. Once again the trajectories (from z=8.16 to z=1) of a sample of IMBHs are over-plotted. This same population of IMBHs in these three scenarios differ only in the IMBHs' velocities and different trajectories depending on the assigned kick. In the first place, kicks have to be large enough to provide IMBHs with a velocity larger than the escape velocity of the host halo. If not, an IMBH will not escape the gravitational potential of the host halo leading to a scenario quite similar to SIM1 (compare Fig. 2.1 and Fig. 2.2). Larger kicks, as in SIM2b, change the IMBHs' trajectories dramatically (compare Fig. 2.1 and Fig. 2.3). Fig. 2.4 explains the difference. Marked as pluses are the maximum escape velocities calculated from the gravitational potential of every dark matter halo selected at z=8.16. Escape velocity decreases with halo radius and reaches its maximum at the center. Hence, the maximum escape velocity is the escape velocity of the IMBH since the IMBH is the particle at the halo center. Escape velocity increases with the halo mass. Shown as circles are the velocities of IMBHs relative to their host halos at z=8.16 after assigning them kicks centered at 75 $\mathrm{km\,s^{-1}}$. The plot shows that IMBHs from less massive host halos have velocities larger than the corresponding escape velocities. With the increase of host halo mass, IMBHs need to acquire larger velocities in order to escape from the host halo gravitational potential. For some of them the assigned kicks are not large enough (all the IMBHs that lie below the data set represented with pluses). These IMBHs fall back and continue the host halo original path toward the primary halo (as when they receive no kicks). This process is demonstrated by the IMBHs in SIM2a (Fig. 2.4 circles), hosted by the most massive halos (kick velocities less than escape velocities). Since we plotted trajectories in Fig. 2.1, 2.2 and 2.3 only for IMBHs hosted by the hundred most massive halos, trajectories in Fig. 2.1 and Fig. 2.2 are almost identical. For this same set of IMBHs, but now with kick centered at 200 $\mathrm{km\,s^{-1}}$ in SIM2b (diamonds), almost all have enough velocity to escape host halos. As a result, trajectories in Fig. 2.1 substantially differ from the trajectories in Fig. 2.3. Unlike Fig. 2.1 and Fig. 2.2, the IMBHs in Fig. 2.3 leave their host halos at z=8.16 and as a result do not form binaries on their path to the primary.

Even though a substantial kick is assigned to the IMBHs, and dynamical friction does not play an important role for them anymore, they still manage to merge with the primary halo. Some fraction of them sink to the center to coalesce with the SMBH at the center of the halo. As the gravitational potential of dark matter halos increases at lower redshifts (Fig. 2.5), kicked IMBHs are captured and sink to the primary. Fig. 2.5 shows the maximum escape velocity as a function of dark matter halos' mass at different redshifts for all the halos identified in our simulation. The primary halo (thick line) goes through a large increase in gravitational potential at lower redshifts. The maximum escape velocity for the primary halo increases from $\sim$250$\mathrm{km\,s^{-1}}$ at z=8.16 to $\sim$700$\mathrm{km\,s^{-1}}$ at z=1. Hence, the growth of the primary halo and the deepening of its gravitational potential well is responsible for the capture of IMBHs originally ejected from their host halos. However, the final spatial distribution of the IMBHs is quite distinct (Fig. 2.6), and their subsequent rate of coalescence with the central SMBH consequently may be different by orders of magnitude depending on kics.

The number of IMBHs inside the primary halo at z=1 is 1958 and in SIM2a the number is only smaller by 14 IMBHs. This is a coincidence, caused by the fact that we changed the velocities of all the IMBHs identified at z=8.16 and not just of those identified inside the primary halo at z=1. This means that some fraction of the IMBHs that did not reach the primary halo originally, reached it in this new simulation because of the changed velocities. Clearly the new IMBH arrive "naked", without being enveloped in the dark matter sub–halos in which they formed originally. The number of IMBHs inside the primary halo in both SIM1 and SIM2a originating from the same sub–halos, is 1851. Thus, 5.4% of the original population found in the primary halo will not be found there due to a change in their velocities at z=8.16. Similarly, a comparable number of the IMBHs that originally did not reach the primary halo, will do so in the new simulation.

The change in the IMBH trajectories in the simulation with larger kicks (SIM2b) is more pronounced (Fig. 2.3). With larger kicks, more IMBHs attain velocities large enough to leave their host halos. Although they need more time to sink into the potential well of the primary halo, 1795 of them reach the primary halo at z=1. The number of IMBHs originating from the same subhalos as in SIM1 is 1630. Thus, 16.7% of the original population is lost due to the kicks, but for the same reason, a new population of IMBHs is kicked into the primary halo, which in total gives 1795 IMBH; implying that the primary halo in SIM2b will have only 8.3% fewer IMBHs than the primary halo in SIM1.

2.4 Post-merger evolution

We find that significantly more black holes sink to the center of the primary halo when they are embedded in their dark matter sub–halos. However, we find that even large kicks cannot prevent the accumulation of IMBHs at the center of a large dark matter halo. Fig. 2.6 shows the number density of the IMBHs inside the primary halo from SIM1, SIM2a and SIM2b. Although the total number of black holes in the primary halo differ from SIM1 by 0.7% for SIM2a and 8.3% for SIM2b, there is a decrease in the number of IMBHs in SIM2 for the inner 10% (in radius) of the primary halo.

We now estimate the dynamical friction time scale for the IMBH and subhalo sinking in the gravitational potential of the halo. From Eqn (1), for a singular isothermal sphere with circular velocity v_c, the velocity dispersion is $\sigma = v_c/\sqrt{2}$; the mass inside the virial radius is 1.52×10^{12} $M_\odot$. For the primary halo these values are $r_{vir} = 370$ kpc comoving, velocity dispersion $\sigma = 157$ km s^{-1}, and impact parameter $b_{max} = r_{vir}$. We calculate a radius (r_{sink}) which IMBHs have to reach in order to merge to the center in less than one Hubble time. We distinguish two cases. First, when the IMBHs are inside sub–halos with a minimum mass of 10^7 $M_\odot$ (SIM1). Second, when an IMBH has been ejected from its parent sub–halo (SIM2). In the first case, the IMBH is brought to some radius inside the primary halo by the parent sub–halo and will continue sinking toward the center while being embedded within the sub–halo. This will occur for the IMBHs at less then $r_{sink} = r_{vir}/30$ when the halo collapse virialises. We find that 4% of the IMBHs formed are at radii less then r_{sink}. So for this model we predict that, in the absence of kicks, 83 IMBHs reach the center and coalesce with the central SMBH (or the seed SMBH formed in the subhalo that became the center of the primary halo). More generally, this predicts $O(10^2)$ IMBH mergers per Milky Way-like halo over one Hubble time; even for the cases shown here where only halos with masses $\geq 2.83 \times 10^7$ $M_\odot$ were allowed to form black holes. Since there are $\sim 10^{10}$ galaxies in the observable universe in this mass range, LISA merger rates will be $\sim 10^{12}$ per Hubble time or R$\sim$100 per year.

In the second case, the kicked IMBHs have a significantly flatter spatial distribution, partly because they get decoupled from their parent subhalos, so there are fewer inside $r_{vir}/30$. Fig. 2.6 shows that there are 2.2% of IMBHs from SIM2a and 0.95% of

IMBHs from SIM2b inside this radius. Fig. 2.7 shows the ratio of IMBHs with kicks and IMBHs without kicks. There is a large drop in the central population of IMBHs with kicks. This can also be seen in the density plots in Fig. 2.8. By repeating the same calculation for dynamical friction as in the previous case, with the only difference in the value for mass in the equation for dynamical friction (8.85×10^5 $M_\odot$ instead of 10^7 $M_\odot$), we calculate that in order to merge at the center, IMBHs in SIM2 have to be at radii less than $r_{sink}=r_{vir}/100$. Notice that while we use particles as tracers of the IMBHs, in reality IMBHs have smaller masses and need to get to smaller radii for dynamical friction to be efficient.

Only 0.25% of the SIM2a IMBHs are inside $r_{sink}=r_{vir}/100$. Thus, under the same assumptions while allowing kicks, only about 4 to 6 IMBHs merge with the central SMBH over a Hubble time—a factor of 20 lower merger rate. In SIM2b there are no IMBHs inside $r_{vir}/100$ except for the one originating from the ancestor of the primary halo at z=8.16. These numbers can increase since, in reality, σ is lower at small radii resulting in smaller t_{fric}. The merger of 83 IMBHs in SIM1 leads to the formation of 7×10^7 $M_\odot$ SMBH inside the dark matter halo with a velocity dispersion $\sigma = 157$ km s^{-1}. From cosmological Monte Carlo realizations of the merger hierarchy (Volonteri et al. 2003), SMBHs of the same mass and halo velocity dispersion can form only when mergers are accompanied with gas accretion as growth mechanisms. However, both the results are below empirical values (Ferrarese 2002). We note that the primary halo is not actually spherical and if a halo is triaxial, then some fraction of the IMBHs can "walk" into the inner halo ($r \ll 10^{-2} r_{vir}$) region on time scale ~ 10 $t_{orbital}$ due to centerphilic box or boxlet orbits (de Zeeuw 1985; Zhao et al. 2002; Holley-Bockelmann et al. 2001). In such cases, dynamical friction becomes effective in bringing the IMBHs to the halo center. Also, some of the IMBHs are being assigned with kick velocities that direct them toward the center. Due to this, some additional IMBHs from SIM1 and SIM2 could reach orbits in the center of the primary halo.

Kicks are also responsible for ejecting IMBHs from gas-enriched regions of the halos. Since gas accretion is one of the main mechanisms for black hole growth, dumping black holes into regions of lower gas densities would prevent AGN-formation. Gas accumulates where the gravitational potential wells are deepest and where dark matter densities are highest. Therefore we may get a crude estimate of the ability of IMBHs to accrete gas by tracing the dark matter density at their positions. Fig. 2.9 shows average local density of dark matter traced by our set of IMBHs vs. redshifts. IMBHs get ejected from their host halos into the regions with lower density. From z=7.75 to z=2.80, kicked IMBHs are in an environment 1-6 times less dense than in the no-kick case. This could suppress formation of AGNs. Note that around z=3.00, the average IMBHs in all three cases start tracing similar density distributions. The number density of AGNs at z=8.16 is $n_{AGN} \sim 1$ Mpc^{-3} assuming that every dark matter halo in SIM1 has formed at least one AGN. Ejecting IMBHs in SIM2a results in a lower number density of AGNs, $n_{AGN} \sim 10^{-2}$ Mpc^{-3} ($n_{AGN} \sim 10^{-3}$ Mpc^{-3} for SIM2b). This implies that for $z \geq 3$, the contribution of faint AGNs to the ionizing background would be decreased if kicks of IMBHs were important.

2.5 DISCUSSION

We have performed and analyzed high-resolution collisionless simulations of the evolution of structure in a ΛCDM model. We have followed the formation and evolution of dark matter halos, and by assuming that each halo hosts an IMBH, we have studied the formation of SMBHs. We focussed on two specific cases. First, IMBHs together with their host halos merge through dynamical friction. Then, we explored the effect of kicks on the IMBH distribution. We found that kicks lead to the ejection of IMBHs from their host halos in many cases. Analytically, it is clear that the dynamical friction will act more efficiently on the host halos than on the less massive black holes formed within them. Our illustrative calculations highlight some of the expected differences in the final density distribution of the black holes. They can be quite different, even in the presence of the modest kick velocities we have imposed. We note that, in general, IMBHs ejected from their parent sub-halos at high redshift still get bound to the most massive dark matter halo at later times but they form a "hot population" with a flatter density profile than the underlying dark matter.

In order for dynamical friction to work accurately in numerical simulations, the density of the background (in this case, the primary halo density) needs to be resolved well. Higher resolution gives smaller softening lengths for particles and smaller softening lengths give more realistic dynamical friction. With the resolution of our current simulations, dynamical friction can not be efficiently realized in the model after $z \sim 1$ and $r \lesssim r_{vir}/30$, because the background density of the parent halos is not resolved well enough. However, our simulations are able to account for effects of dynamical friction on the sub-halos at high z (Vine & Sigurdsson 1998). Subsequent papers will track the dynamical evolution of the sub-halos and IMBHs at late times, using higher resolution simulations and semi-analytic implementations of dynamical friction (Binney & Tremaine 1987). A little over 4% of IMBHs merge with the SMBH at the center in less than one Hubble time. If this is the dominant way of creating SMBHs, then it is efficient even if the IMBHs are ejected from their parent halos, with merger numbers only reduced by a factor of two or so for modest kicks. LISA observations should strongly constrain any kick on IMBHs formed from very massive Pop III stars in low mass proto-galactic sub-halos.

If these IMBHs accrete from the interstellar medium they may also be found by deep X–ray observations (Agol & Kamionkowski 2002) in the Milky Way. The observational signature will depend sensitively on the spatial distribution of these black holes in our galaxy. Similarly, the next generation of micro-lensing searches may be able to constrain high mass black holes from the longest events (Agol et al. 2002).

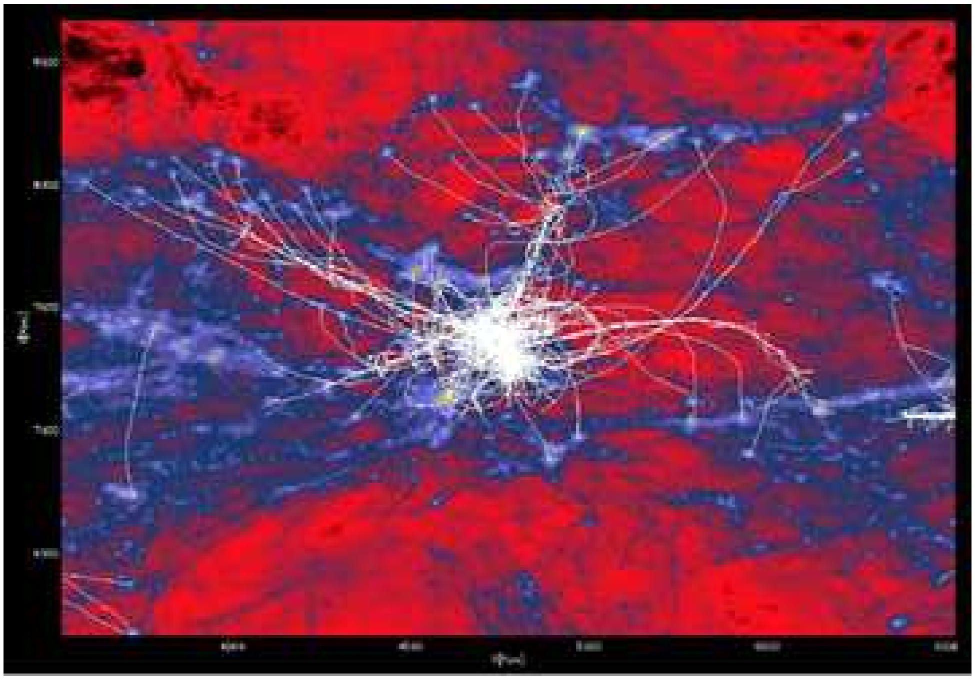

Fig. 2.1 Sample of hundred IMBHs selected from most massive host halos at z=8.16 and their trajectories (white) from z=8.16 to z=1 overploted on a 2D density projection. Density peaks in yellow correspond to host halos centers at z=8.16 and to the positions of the IMBHs. Kick has not been assigned in the SIM1 case.

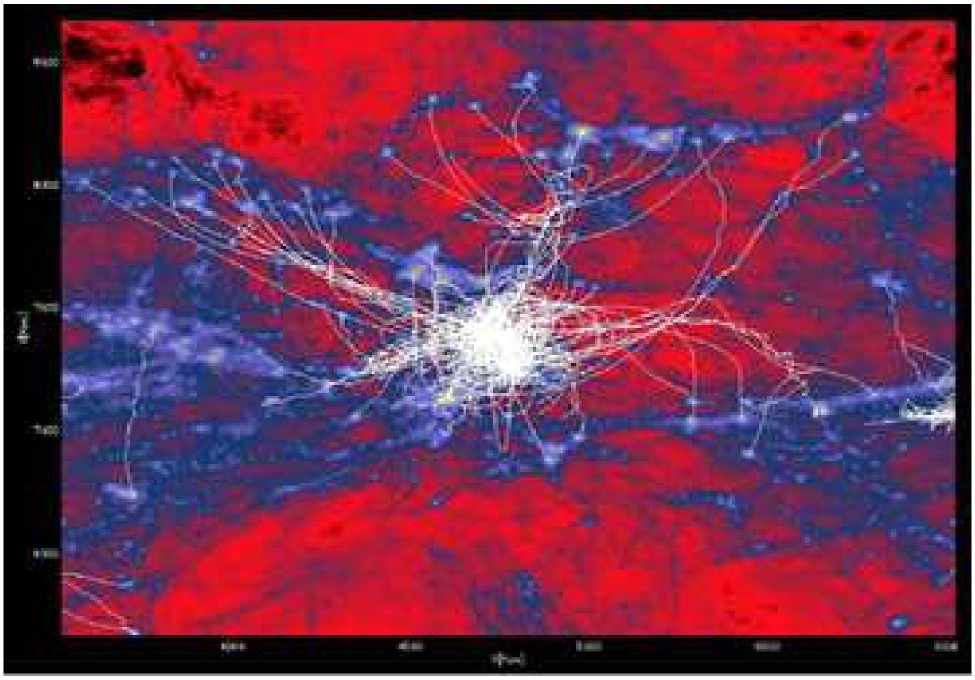

Fig. 2.2 In SIM2a kick has been assigned in the range [0,150] km/s, centered at 75 km/s. With large kicks IMBHs overcome the host halos' gravitational potential resulting in a change of their trajectories and the final distribution of IMBHs (the smearing of the trajectories at the center is quantified in the later plots). Observe, e.g., the upper right corner where two IMBHs form a binary. In SIM2a, IMBHs are trying to escape but the growing dark matter gravitational potential recaptures them.

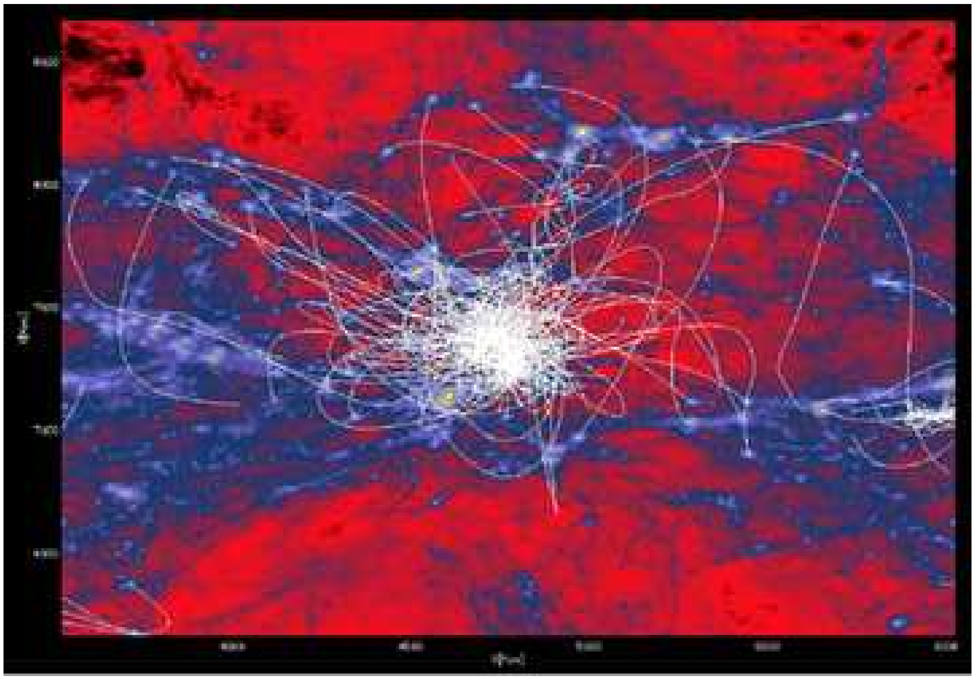

Fig. 2.3 In SIM2b kick has been assigned in the range [125,275] km/s, centered at 200 km/s. The assigned kick is larger than in SIM2a and also large enough to prevent binary formation. Underneath the binary discussed in the previous figure, at the coordinates [5700,7000]kpc, a dense halo center hosts an IMBHs. In less than 100 kpc, this halo captures three more IMBHs. This small "cluster" of IMBHs spirals in toward the center. The picture clearly resolves IMBHs orbits around the center of mass up to the point, [5200,7400] kpc, where the orbital separation is smaller then the softening length. This point is reached later in SIM2a because of the kicks, and in SIM2b binaries never form.

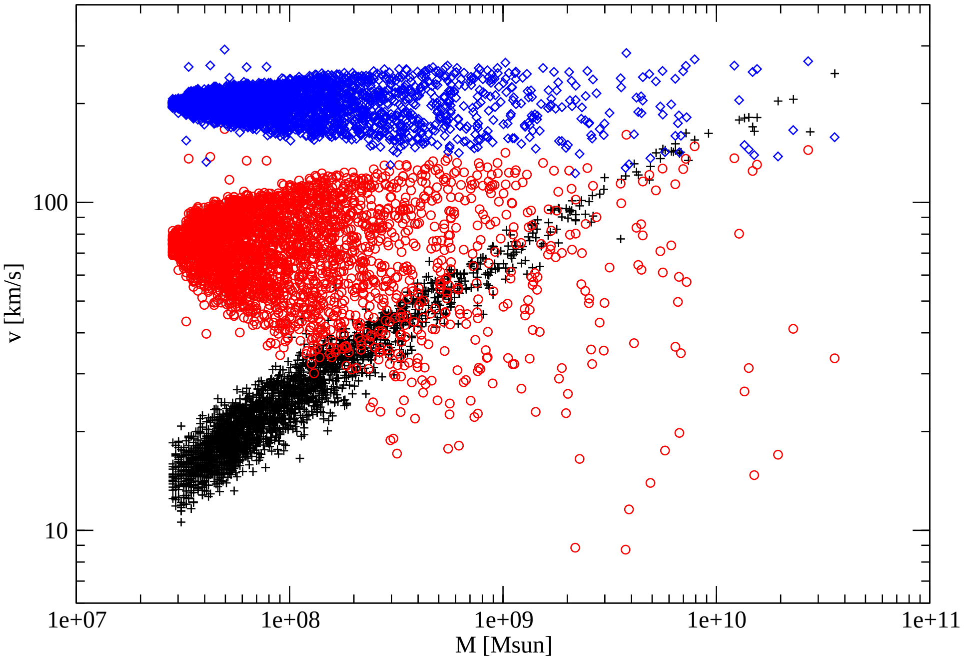

Fig. 2.4 Black holes' escape velocity as a function of halo mass (z=8.16) as pluses, calculated from gravitational potential of the host halo set consisting of 2869 members. Kicks: [0,150] km/s centered at 75 km/s repesented as circles and [125,275] km/s centered at 200 km/s represented as diamonds. Lower mass host halos have lower maximum escape velocities enabling their IMBHs to escape. IMBHs in more massive host halos demand larger kicks in order to escape. As a result, some of them stay captured in their host halo gravitational potential.

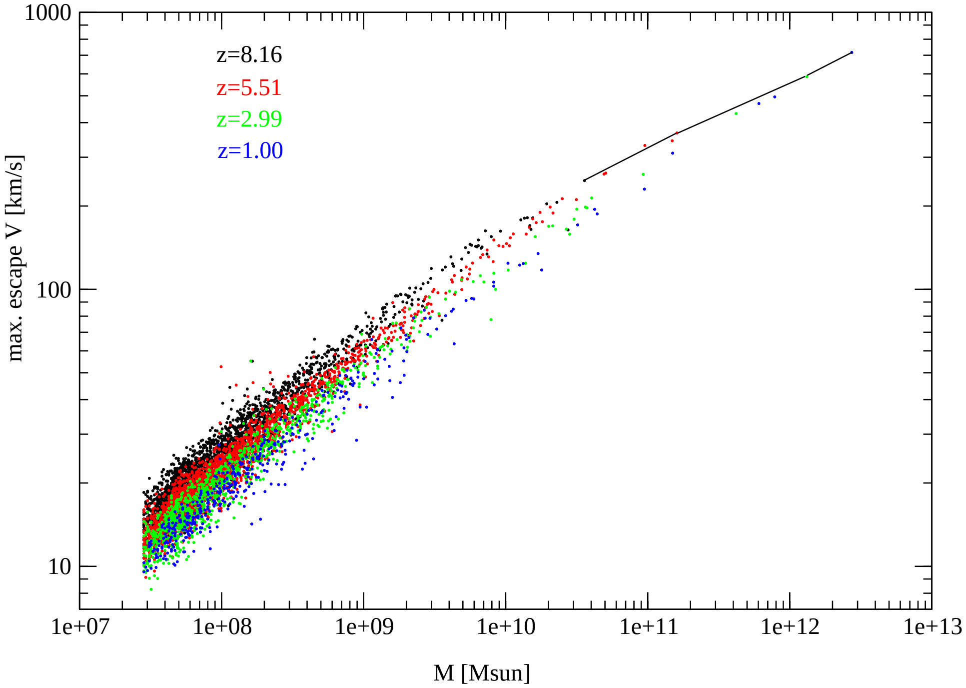

Fig. 2.5 Maximum escape velocity (corresponding to the central gravitational potential) of dark matter halos at different redshifts as a function of dark matter halos' masses. The gravitational potential of the primary halo (thick line) increases at lower redshifts, capturing even the IMBHs which have been assigned with highest kick velocities.

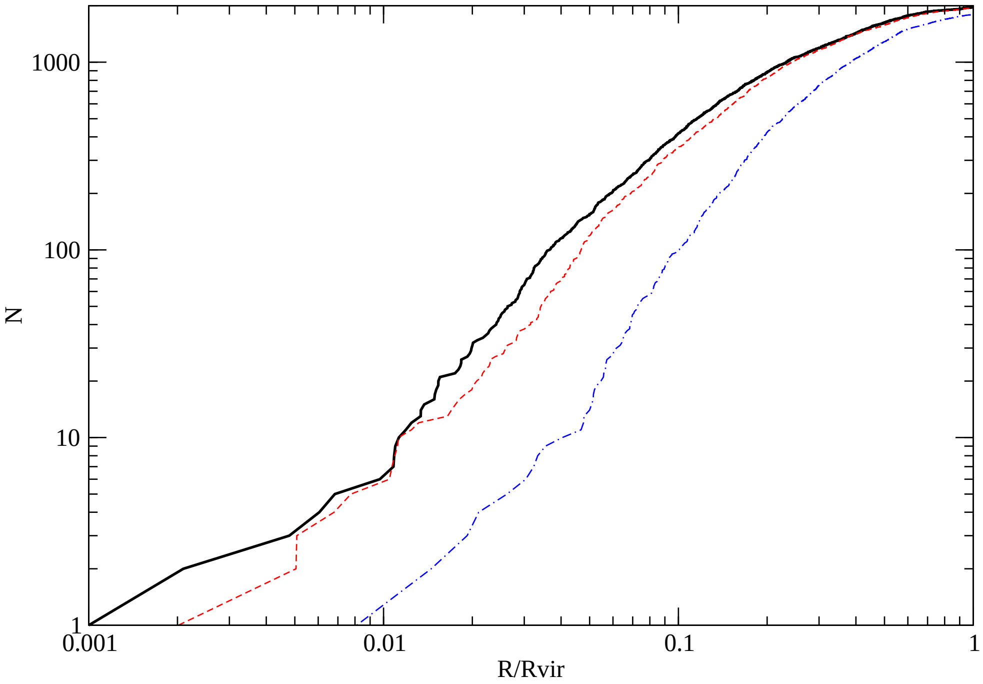

Fig. 2.6 Number of black holes as a function of primary halo radius at z=1. No kick case (thick); [0,150] km/s kick centered at 75 km/s (dash) and [125,275] km/s kick centered at 200 km/s (dash-dot). Although the number of IMBHs entering primary halo is comparable in all three cases, the difference in their interior distribution is well pronounced.

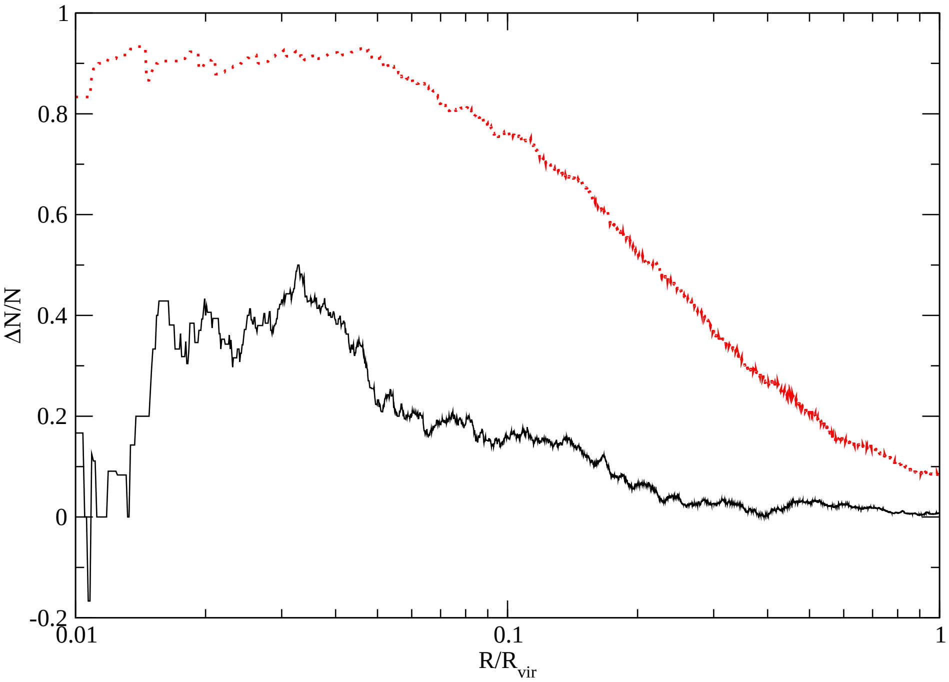

Fig. 2.7 Fraction of SIM1 black holes in SIM2a and SIM2b as a function of radius. ΔN is N - N_{kick} where N is number of black holes in SIM1 (no kick). Thick line for [0,150] km/s kicks centered at 75 km/s and dots for [125,275] km/s kicks centered at 200 km/s.

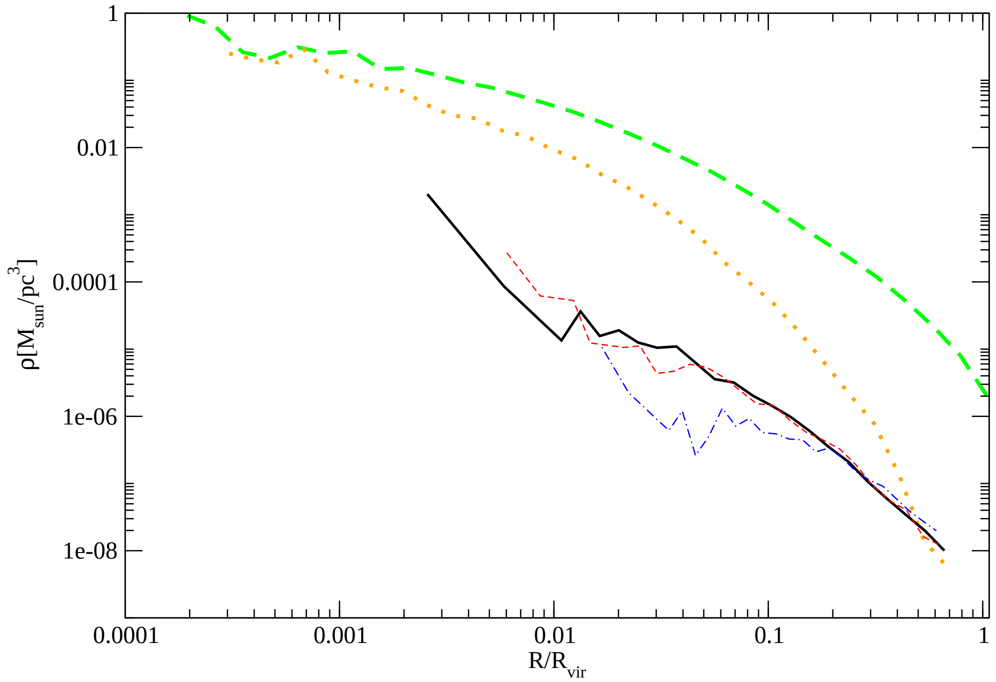

Fig. 2.8 Density of the primary halo at z=1 (thick dash) and its most massive progenitor from z=8.16 (dots) as a function of radius. Also, density in hosted black holes for no kick (thick); [0,150] km/s kick centered at 75 km/s (dash) and [125,275] km/s kick centered at 200 km/s (dash-dot).

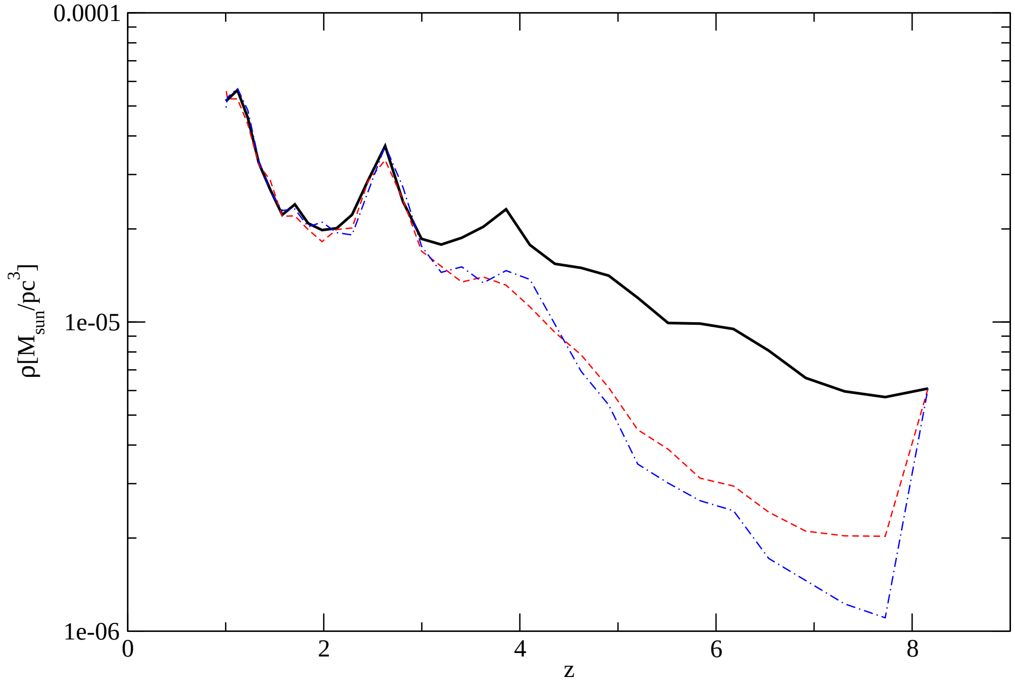

Fig. 2.9 Local density of dark matter traced by black holes as a function of redshift. No kick (thick); [0,150] km/s kick centered at 75 km/s (dash) and [125,275] km/s kick centered at 200 km/s (dash-dot). Ejection of IMBHs from gas enriched regions of galaxy influences AGNs formation rates while reducing their numbers and their contribution to the ionizing background.

Chapter 3

Supermassive Black Hole Growth and Merger Rates from Cosmological N-body Simulations

The following chapter has been accepted for publishing in the MNRAS and can be found on ASTRO-PH under the name "Supermassive Black Hole Growth and Merger Rates from Cosmological N-body Simulations", Micic, M., Holley-Bockelmann, K., Sigurdsson, S., Abel, T., 2007, astro-ph/0703540.

3.1 INTRODUCTION

Supermassive black holes (SMBH) are thought to dwell at the centers of most galaxies (Kormendy & Richstone 1995), with masses between 10^6 $M_\odot \lesssim M \lesssim 10^9$ $M_\odot$. In principle, the abundance of SMBHs today can be explained if they grow through mergers and early accretion (Schneider et al. 2002), from a gaseous disk. The most likely candidates for SMBH seeds are black holes that form as remnants of Population III stars at redshifts $z \gtrsim 12$-20 (Heger et al. 2003; Volonteri et al. 2003; Islam et al. 2003; Wise & Abel 2005). These relic seeds are predicted to form in the centers of dark matter halos (DMH), and have masses $\lesssim 10^3$ $M_\odot$ (Abel et al. 2000, 2002). DMHs form in the early universe and hierarchically merge into larger bound objects. As DMHs merge into massive halos, the seed black holes sink to the center through dynamical friction and eventually coalesce.

Although the seed formation stops at $z \sim 12$ as Population III supernovae rates drop to zero (Wise & Abel 2005), SMBH growth continues as DMH mergers proceed to low redshifts. From a combination of gas accretion and binary black hole coalescence, seeds can grow to intermediate mass black holes (IMBHs, with masses 10^2 $M_\odot \lesssim m \lesssim 10^5$ $M_\odot$). With continued mergers and gas accretion, it is thought that these IMBHs may form the SMBHs we observe today. The detection of IMBHs is a matter of debate, but possible candidates are ultraluminous X-ray sources in young star-forming regions (Fabbiano 1989; Roberts & Warwick 2000; Ptak & Colbert 2004; Fabbiano & White 2006) and nearby extragalactic star clusters.

Although this scenario works in general, the real detailed understanding of how seed black holes grow is a remaining challenge. For example, there are still debates on the seed black hole masses, on the mass of halos that can host seeds, on the seed formation redshift, on the type and efficiency of gas accretion, and on the dynamics of the black hole mergers. All of these compound to yield a huge range in black hole merger rate estimates. Recent black hole merger rate calculations span over three orders of magnitude: Haehnelt (1994) calculates the merger rate to be $R \sim 0.1$ - 100 events per year; Menou et al. (2001), $R \sim 1$ - 100 yr^{-1}; Wyithe & Loeb (2003), $R \sim 15$ - 350 yr^{-1}; Sesana et al. (2004), $R \sim 10$ yr^{-1}; and Rhook & Wyithe (2005), $R \sim 15$ yr^{-1}.

There are two general approaches to the problem: direct cosmological N-body simulations and analytical techniques based on a Press-Schechter (PS) formalism (Press & Schechter 1974). Both methods extract merger rates from the DMHs' merger tree. N-body simulations have the advantage that the evolution of density fluctuations is followed in complete generality, without the need for any of the assumptions involved in creating PS merger trees. Extended Press-Schechter theory (EPS) combines the PS halo mass function with halo merger rates derived by (Lacey & Cole 1993), and it stands as the most widely used method for calculating merger rates. Unfortunately, EPS is mathematically inconsistent (Erickcek et al. 2006) since it provides two equally valid merger rates for the same pair of DMHs. It is also unclear whether EPS reproduces the DMH mass function at high redshifts (Reed et al. 2007). With N-body simulations, there are, in principle, no constraints on the halo mass, structure or kinematics. Unfortunately, the mass and spatial resolution needs to be extremely high, and even in the best resolved N-body simulations of a large volume ΛCDM universe (Nagashima et al. 2005), the mass resolution sets the minimum DMH mass to 3×10^9 $M_\odot$ for halos with as few as ten particles. Hence using direct N-body simulations to track the dynamics of seed black holes as they grow within a large comoving volume is out of reach of our current technology.

In this paper, we have developed a hybrid method to follow the merger history of seed black holes as they grow. We performed a high resolution cosmological N-body simulation in the unexplored parameter space of a *small cosmological volume* but with very high mass resolution to achieve well-resolved halos with a minimum of 32 particles and mass as low as $M_{\rm halo}=2.8\times10^7$ $M_\odot$. The goal was to look at a representative "Local Group" structure, comparable to the one which hosts the Milky Way, and to resolve as low a mass as feasible. We improved the algorithms for identifying dark matter structures and developed set of physically-motivated criteria for seeding DMHs. We then constructed the DMH merger tree, which provides a testbed to study the effects of different gas accretion scenarios. In addition to the merger rate, we extracted observables such as the black hole mass function over cosmological time. This method is a major improvement in calculations of MBH merger rates and presents the first step toward a full treatment of the black hole growth problem. Massive black holes mergers will be one of the prime signals for future space-based gravitational wave observatories like LISA (Laser Interferometer Space Antenna) and BBO (Big Bang Observer). Possible detection depends on a number of parameters: the mass ratio of merging black holes, the total mass of the black hole binary, and the redshift.

We describe our simulation and DMH seeding criteria in Section 3.2; obtaining DMH and black hole merger trees in Section 3.3 and 3.4 together with description of black hole growth models; black hole merger rates in Section 3.5. Finally, we discuss our results in Section 3.6.

3.2 SIMULATION

3.2.1 Simulation Setup

In our numerical simulations, we use GADGET (Springel et al. 2001b) to evolve a comoving 10 Mpc^3 section of a ΛCDM universe (Ω_M=0.3, Ω_Λ=0.7, σ_8=0.9 and h=0.7) with periodic boundary conditions from $z = 40$ to $z = 0$. We refine a sphere of 2 Mpc in the box to simulate at a higher resolution with 4.9×10^6 high-resolution particles (softening length 2 kpc comoving). The rest of the box has 2.0×10^6 low-resolution particles (softening length 4 kpc comoving). The mass of each high resolution particle in this simulation is $8.85\times10^5 M_\odot$, and the mass of each low-resolution particle is $5.66\times10^7 M_\odot$. A detailed description of this simulation can be found in the previous chapter.

3.2.2 Linking Length Problem

Identifying and following a real DMH in a cosmological simulation is technically challenging. If the minimum number of particles in a halo is set too low, the DMH identified at one time-step might later disperse. In the widely used Friends-of-Friends algorithm (FOF), if the linking length (b) is too large, large dark matter structures might bridge through a small number of tidally stripped particles. When this occurs, the FOF algorithm can not properly identify DMHs. A linking length of 0.2 has traditionally been used (Davis et al. 1985) since the DMH mass function obtained with it proved to be consistent with observations at low redshifts and mass functions obtained by PS theory. However, very little is known about DMH mass functions at high redshifts, $z\gtrsim10$, and low masses, $M\lesssim10^9$ $M_\odot$, or about the validity of this linking length. For example, (Gao et al. 2005) noted that the first massive halos are found in regions containing many smaller halos which line up along filaments and sheets and can not be identified by the FOF algorithm when a linking length of b=0.2 is used. The only criterion for initializing the linking length comes from the spatial resolution in the performed numerical simulation: the linking length has to be larger than the softening length. High resolution simulations have small softening lengths, which allow the linking length to be smaller as well. Consequently, in our high resolution simulation, we set b=0.1. With this value for linking length we eliminated all the problems in identification of dark matter structures.

3.2.3 Analysis Tools

We used P-GroupFinder algorithm (Springel et al. 2001a) to identify DMHs in each of our 104 GADGET output files. The analysis starts with a FOF algorithm (b=0.1) which spatially separates dark matter halos. The minimum number of particles per halo is set to 32. The minimum DMH mass resolved with 32 particles in our simulation is $M_{halo}=2.8\times10^7$ $M_\odot$. Then, we find a gravitationally bound counterpart for each FOF halo and continue with the SUBFIND algorithm to identify substructures in every DMH. We require that halos and subhalos be virialized to be considered real. This requirement is met when the DMH density is above 200 times the average density of the universe at a specific redshift. Since we are studying merger rates for Pop III massive black holes, we then select those halos that are capable of hosting Pop III stars, using primordial supernova rates (Wise & Abel 2005). Primordial stars can form in DMHs with a minimum mass of 4×10^6 $M_\odot$ if H_2 cooling is the primary mechanism and if the UV background has a negative feedback. They can also form through hydrogen atomic line cooling in halos with mass $M_{vir}\gtrsim10^8$ $M_\odot[(1+z)/10]^{-1.5}$. The lifetime of Pop III stars is ~3 Myrs and the end product is a population of seed black holes with 100 $M_\odot\lesssim M_{BH}\lesssim1000$ $M_\odot$. The first Pop III seed black holes form at redshift $z\sim20$ and the last Pop III stars die at redshift $z\sim12$. We select the interval $12\lesssim z\lesssim19$ to seed those DMHs which have masses $M_{vir}\gtrsim10^8$ $M_\odot[(1+z)/10]^{-1.5}$. At z=19 all DMHs with mass above $M_{halo}=3.5\times10^7$ $M_\odot$ and at z=12 all of the DMHs with mass above $M_{halo}=6.7\times10^7$ $M_\odot$ are seeded. We point out that we will run new simulations with new WMAP2 cosmological parameters and new values for POP III supernovae rates.

3.3 Dark Matter Halos' Merger Tree

Starting with the first snapshot i , we identify DMHs with the set of criteria described above. The most bound particle at the center of each DMH that satisfies the criteria is set to be a seed black hole. At the following snapshot i+1 , we identify halos from the previous i snapshot. At i+1 we again seed new halos that satisfy our criteria. By "new" halos we consider only those halos that do not have any particles that were part of any already seeded halo. This is because once a halo is seeded it can not form a new black hole due to feedback from the UV background of Pop III stars (Machacek et al. 2001). Meanwhile, we also trace the parent DMH at i for every particle in every DMH at i+1, thus constructing a complete merger history. The method is repeated through the redshift range $12 \lesssim z \lesssim 19$. Seeding stops at redshift z=12 but we continue with creating a merger history until redshift z=0. In total we have 1447 seed black holes.

3.4 Assembling a Black Hole

After constructing the DMH merger tree, we turn our attention to the evolution of the seeds. The N-body simulation tracks all the seed black holes and their host halos from z=19-0. In order to study black hole growth as a function of time, environment, and merger type, we constructed three black hole merger models which we detail below.

We parameterize the degree of gas accretion involved in growing the black hole and the efficiency of binary coalescence. In the fiducial case, we modeled black hole mergers in the simplest possible way. We assume that the hardening timescale (the time for two black holes to form hard binary) is rapid, that the loss cone is full (Berczik et al. 2006; Sigurdsson 2003; Holley-Bockelmann & Sigurdsson 2006), that no black holes are ejected, and that there is no gas accretion involved. This gives us a strawman model with which to compare more realistic black hole growth scenarios. We assign seed black hole masses of $200\,\mathrm{M}_\odot$. When two DMHs merge, their seeds form a binary and merge at the center of the remnant with the total combined mass of its progenitors. If more than two DMHs merge, as often happens early on, the merger is sorted by DMH mass, since dynamical friction is stronger on higher masses. We assume that dynamical friction is very efficient in merging the black holes one the parent halos merge. Again, this yields an upper limit on the merger rate derived for this halo; we will explore the effects that can supress this rate in our next paper. However, in a gas rich, triaxial, and/or highly non-equilibrium galaxy, the black hole merger timescale may be quite small ; Kazantzidis et al. (2005) shows that dynamical friction is efficient even in unequal-mass mergers because gaseous dissipation compactifies the companion galaxy, enabling it to survive complete tidal disruption to more quickly shepard the host SMBH to the center of the remnant. This can lead to very high pairing efficiencies of SMBHs. Escala et al. (2005) suggest that equal mass black hole binaries will merge within a few times 10^7 yr. Since DMHs typically merge in 10^8 yr, the MBHs will coalesce soon after the DMHs merge in this model. As the halos evolve to the present day, black holes can only grow in mass through mergers, and in our (small cosmological volume) simulation reached a maximum mass of $\mathrm{M}_{\mathrm{BH}}=3\times10^5\ \mathrm{M}_\odot$. We find that this value is too small to match observations.

For a sustained Eddington accretion, the mass growth rate is:

$$\dot{M}_{\mathrm{BH}} = \frac{M_{\mathrm{BH}}}{t_{\mathrm{Sal}}}, \tag{3.1}$$

where $\mathrm{t}_{\mathrm{Sal}}$ is the Salpeter time-scale, $\mathrm{t}_{\mathrm{Sal}} \sim 4\times10^7$ yr from the recent observations (Hu et al. 2006). In our models, we assume that accretion is triggered by galaxy mergers and lasts $\sim\mathrm{t}_{\mathrm{Sal}}$. During this time, the black holes approximately double their mass. However, we do not assume that every merger supplies enough gas for the black hole to double its mass. For example, during minor galaxy mergers (mass ratios much larger than 10:1), the more massive galaxy will shred the satellite (e.g. White (1983); Holley-Bockelmann & Richstone (1999)), and the black hole will sink toward the central black hole without a large reservoir of gas. On the other hand, the merger of comparable (mass ratios less than 10:1) galaxies will generate ample gas accretion onto the central black hole, as the satellite triggers a central starburst (Mihos & Hernquist 1994). Here we distinguish two cases, depending on the mass ratio of merging DMHs. The first is a more conservative criterion that allows black holes to accrete gas if the mass ratio of host DMHs is less than 4:1 (4:1 accretion). The second case sets an upper constraint on the mass of the final black hole by allowing seeds to accrete gas as long as the merging DMHs have a mass ratio less than 10:1 (10:1 accretion). In the following section, we compare all three growth scenarios: black hole growth through mergers only (dry growth); growth through mergers combined with 4:1 gas accretion (4:1 growth); and finally, growth through mergers combined with 10:1 gas accretion (10:1 growth). These are simplifying assumptions made to explore parametrically the range of solutions in our scenario.

3.5 RESULTS

From z=19 to z=12, we identified all of the DMHs in the manner described in the previous section. With this approach, we obtained the initial positions and formation redshifts for 1477 seed black holes, approximately 100 new MBHs per snapshot. We assigned an initial mass of 200 $M_\odot$ to each MBHs and traced their merger history from $0 \lesssim z \lesssim 19$. Fig. 3.1 shows that the mass density of SMBH in our models is smaller then the values obtained from observations at low z, i.e. $\rho_{\rm BH}(z = 0) \sim 35 \times 10^5\ M_\odot\ {\rm Mpc}^{-3}$, (Aller & Richstone 2002). Most of the mass is in the $\sim 10^8\ M_\odot$ black holes. Our values are smaller since we are exploring low mass end of SMBH that contributes little to total mass density.

3.5.1 Growth of Sagittarius A*

Throughout the simulation, one DMH emerges as the largest in mass and dominates the dynamics of its group. Its mass at z=0 is $M_{\rm primary} = 4.5 \times 10^{12}\ M_\odot$ which roughly corresponds to Andromeda's DMH, and is somewhat higher than estimates for the Milky Way's halo (Dehnen et al. 2006). This halo grows through the smooth accretion of dark matter particles as well as DMH mergers. Meanwhile, the central black hole grows through gas accretion (if we included it) and mergers. We traced the growth of both the primary halo and its massive black hole as a function of redshift (Fig. 3.2). Fig. 3.2 compares the growth of both the black hole (dry) and its host DMH. Overplotted is a descriptive redshift dependence because it exists only where the curve has a negative slope. Initially, the primary halo grows in mass only through smooth accretion and reaches $M_{\rm primary} = 10^9\ M_\odot$ by z=15 (Fig. 3.2). During this period, the black hole remains at its initial mass. At all other redshifts, the growth of the primary halo and any other DMH can be described as a cycle of steady accretion of the surrounding dark matter punctuated by rapid growth through mergers with incoming DMHs.

We present the DMH merger rates in Fig. 3.3. In comparing Fig. 3.2 and Fig. 3.3, notice that changes in merger rate catalyze both the MBH and primary halo mass growth. Fig. 3.3 presents merger rates as the number of mergers per unit time per unit redshift for all halos, while Fig. 3.2 traces the merger history for the primary halo only. Nevertheless, since the primary halo participates in 90% of all DMH mergers, Fig. 3.3 essentially follows the evolution of the primary halo. At z$\sim$11, the central black hole with mass $M_{BH} \sim 3000\ M_{\odot}$ has reached the IMBH range. At this redshift, the merger rate reaches maximum (Fig. 3.3). Consequently, the IMBH grows quickly from $\sim 3000\ M_{\odot}$ to $\sim 10,000\ M_{\odot}$ although surprisingly the bound DMH mass decreases.[1] Merger rates decrease at z$\lesssim$10 but experience two more peaks with periods of violent mergers around z=6 and z=3 (Fig. 3.3). Note that these two peaks in merger rates need to be tested for cosmic variance in order to establish that they are physical. We intend to do this by running a new simulation in a larger cosmological volume.

At z=0, there is one SMBH with mass $M_{SMBH}=2.9\times10^5\ M_{\odot}$ at the center of the primary halo (Fig. 3.2 and Fig. 3.4 thick line). This mass is too small to match present day observations, so we know, as has been stated, that mergers alone can not create a SMBH. As described before, we used the Salpeter approximation to model different gas accretion scenarios where the accretion efficiency depends on the mass ratio of merging DMHs. In all three scenarios, the black hole reaches the IMBH range at z$\sim$12 (Fig. 3.4). As the number of DMH mergers increases, the IMBH continues growing – faster, naturally, if gas accretion is more efficient. In a 4:1 growth scenario, the IMBH grows to a $2.3 \times 10^6\ M_{\odot}$ SMBH by z=5.5. At these redshifts, low mass ratio mergers of DMHs are depleted and SMBH growth through gas accretion stops. Therefore, the duty cycle of the active galactic nucleus (AGN) hosting this SMBH dies at z=5.5, too. In this model, the SMBH mass remains essentially constant for $\lesssim$5.5, because it only experiences very high mass ratio mergers with 200-1000 $M_{\odot}$ black holes. Finally, at z=0 the AGN has evolved into galaxy hosting a $2.3 \times 10^6\ M_{\odot}$ SMBH at its center, strikingly similar to the mass of the Milky Way SMBH (Schödel et al. 2002; Ghez et al. 2003, 2005). A highly efficient 10:1 growth scenario yields an upper constraint of $3.4 \times 10^7\ M_{\odot}$ – comparable to the SMBH observed in M31 (Bender et al. 2005).

Fig. 3.5 shows the SMBH mass as a function of central velocity dispersion and redshift for our three growth scenarios. We obtained the velocity dispersion for dark matter at 10 kpc comoving from the halo center. Recall that 10 kpc comoving corresponds to 700 pc at z=19 and 14 kpc at z=0. Similar to Fig. 3.4, every decrease in dark matter velocity dispersion is a consequence of high merger rates at a specific redshift. The maximum value for the velocity dispersion obtains at z=0, σ = 120 km^{-1}. When compared to the M-σ relation from (Gebhardt et al. 2001a; Merritt & Ferrarese 2001b), a SMBH of $\sim3\times10^7\ M_{\odot}$ has a stellar velocity dispersion of σ = 120 km^{-1} at z=0, which matches the SMBH mass in the 10:1 growth scenario. Of course our M-σ relation is derived only from the dark matter and at much larger radii, but this may give us a hint

---

[1] In DMH mergers, the outskirts can become unbound for a short period of time, but may be reaccreted as the structure grows. The large number of DMH mergers between 10$\lesssim$z$\lesssim$12 (Fig. 3.3), increases the number of unbound dark matter particles, since there is not enough time for reaccrete before another merger.

that the M-σ relation is tied to the dynamics of the global potential (Ferrarese 2002). Exploring the formation of more massive SMBHs under this set of assumptions, including the redshift at which growth occurs and the merger rate as a function of redshift is beyond the scope of this paper.

3.5.2 Black Hole Merger Rates and ULXs

Although there are no studies of AGN duty cycle for z>6 and $M_{SMBH} \lesssim 10^6$ $M_\odot$ (Wang et al. 2006), it is probable that the AGN fueling mechanism – gas accretion – is similar to that of higher mass galaxies. The SMBH in 4:1 and 10:1 growth scenarios grows to its final mass of $M_{SMBH} \sim 10^6 M_\odot$ - $few \times 10^7 M_\odot$ in the redshift range $5.5 \lesssim z \lesssim 6$. As major mergers dictate the growth at z>6, the SMBH evolves as a low luminosity AGN with the duty cycle governed by on and off switching of accretion onto the black hole. The AGN duty cycle drops to zero at z∼6 as the host galaxy becomes too large for major mergers to occur and both the SMBH and its host galaxy enter a quiet phase of their growth through mergers with much smaller galaxies.

Interestingly, all incoming small galaxies at z∼6 in our model carry an IMBH ∼1000 $M_\odot$. This sets the stage for a phase where each new galaxy merger can be characterized as a dwarf starburst galaxy with a central IMBH accreting gas while sinking toward the SMBH at the center. In other words, in these later phases the lower mass incoming black hole may accrete gas, but we assume no significant gas accretion onto the central SMBH because of the high mass ratio of the black holes. With the exception of the largest black hole in our simulation, all other black holes fall into the IMBH range: $200 M_\odot \lesssim M_{IMBH} \lesssim 10^4 M_\odot$. These black holes are of the special interest as candidates for ULX sources (Mii & Totani 2005). ULXs are interpreted as massive black holes accreting gas in starburst galaxies, although this is still a matter of debate (King et al. 2001).

Fig. 3.6 shows the merger rates for different mass ratio ranges and total binary masses. When deconstructed into ranges of mass ratios and log total binary mass (defined as $p = \log(m_1 + m_2)$), these merger rates can be used to predict the number of ULX sources in starburst galaxies throughout the galaxy evolution, assuming that merging galaxies are reasonably gas rich. For the mass ratio $1 \lesssim m_1/m_2 < 10$, we see only minor differences between the three growth scenarios for any range of binary mass (Fig. 6a, 6b, 6c). For $z \gtrsim 10$ black holes grow mostly through mergers. For z∼8, mass ratio <10 and binary mass $10^3 M_\odot < m_{BH} < 10^4 M_\odot$ ($3 \lesssim p < 4$) the merger rate is $R \sim 10$ yr^{-1} in all three growth scenarios – and it reaches a maximum $R_{max} \sim 30$ yr^{-1} for p<3. At lower redshifts the merger rates decrease rapidly (Fig 6a, 6b, 6c), and gas accretion becomes important (Fig. 3.4). Nevertheless, there are no changes in Fig 6a, 6b, 6c for z<10 since the mass ratio of merging black holes becomes very large as the higher mass black holes gain mass preferentially (Fig. 3.7). In our scenario, only the black holes at the centers of merging DMHs grow through gas accretion; a large number of DMHs remain isolated for most of the simulation and merge late in high mass ratio encounters (middle and bottom panels of Fig. 3.6). The difference between the top and bottom panels in Fig. 3.6 shows that most of the black hole mergers at high redshifts are with $1 \lesssim m_1/m_2 < 10$ mass ratio.

Since black holes grow faster with more efficient gas accretion, the merger rates for mass ratio $10 \lesssim m_1/m_2 < 100$ and total binary mass 10^4 $M_\odot < m_{BH} < 10^6$ $M_\odot$, shift toward higher redshifts in our accretion models (Fig 6d, 6e, 6f). In this mass ratio range, $3 \lesssim p < 4$ mergers peak at $8 \gtrsim z \gtrsim 10$, with a merger rate of ~ 10 depending on the growth scenario. Very high mass ratio mergers $10^2 \lesssim m_1/m_2 < 10^4$ are of special interest (Fig. 3.6 bottom panels). At $z<6$, high mass ratio DMH mergers correspond to a dwarf galaxy or globular cluster being consumed by a massive galaxy. The IMBH carried by smaller counterpart will eventually coalesce with SMBH at the center by first forming a binary with total mass $p>5$ and high mass ratio $10^2 \lesssim m_1/m_2 < 10^4$. This is an ideal LISA source, as will be explored in more detail in our next paper.

As a result, the merger rates in Figure 6d, 6e, 6f and Fig. 3.8 for the above total binary mass and mass ratio ranges directly correspond to the number of IMBHs per galaxy per redshift. Since the accretion timescale is approximately half the merger time scale, the ULX number density is $N_{ULX}=R/2$. In the case of dry growth (Fig 6g), a black hole binary with mass 10^5 $M_\odot < m_{BH} < 10^6$ $M_\odot$ has an approximately constant and high merger rate of $R \sim 15$ yr^{-1} for $2<z<6$. This corresponds to ~ 7 ULX sources per starburst galaxy at $2<z<6$. Similarly, the 10^5 $M_\odot < m_{BH} < 10^6$ $M_\odot$ binary in the 4:1 growth scenario has $R \lesssim 10$ yr^{-1} (Fig 6h) and $N_{ULX}=5$. More importantly, Figure 6h shows $N_{ULX}>2$ at $2<z<10$. For even higher mass ratios $10^4 \lesssim m_1/m_2 < 10^5$, the merger rate is $R \lesssim 12$ yr^{-1} for $z \lesssim 3$.

Fig. 3.8 shows merger rates for the 10:1 growth scenario and high mass ratio $10^4 \lesssim m_1/m_2 < 10^6$ for 10^6 $M_\odot < m_{BH} < 10^8$ $M_\odot$ mergers. ULX sources in Fig. 3.8 and Figure 6g, 6h have constant number density of ~ 10 per starburst galaxy at $z> 2$. The ULX number density drops rapidly at $z=2$. Note that these ULX sources are not the same as the ULXB sources seen in local universe with much shorter accretion lifetimes.

3.5.3 Comparison to Results from Press-Schechter theory

We compare our results with those obtained by various black hole merger models from EPS theory. Fig. 3.9 shows the merger rates for four Press-Schechter models decribed in (Sesana et al. 2007). In the VHM model, massive DMHs ($M_{DMH}=10^{11}$ - 10^{15} $M_\odot$) are seeded with $m_{BH} \sim 200$ $M_\odot$ black holes at $z=20$; in the KBD model, low mass halos ($M_{DMH}=10^6$ - 10^7 $M_\odot$) are seeded with $m_{BH} \sim 5 \times 10^4$ $M_\odot$ at $15 \lesssim z \lesssim 20$; and the BVR models explore different redshift ranges for seeding black holes in halos: $m_{BH}=10^4 - 10^5$ $M_\odot$ at $15 \lesssim z \lesssim 20$ in the BVRhf model and $18 \lesssim z \lesssim 20$ in the BVRlf model. Figure 9a superimposes their merger rates with our results. Considering that these two methods have different choices for the seeding redshift range, the mass of the seeds, the mass of dark matter halos, and constraints on number of mergers per halo, the results match remarkably. At $z \lesssim 10$ our merger rates match the KBD model. However, we have an overall higher merger rate, with multiple peaks at $z=6$ and $z=3$ from episodes of violent DMH dynamics (if proven not to be the consequence of cosmic variance) that is not depicted by EPS theory (Figure 9a). In numerical simulations, there is no limit on number of progenitors for each halo, while in a standard EPS treatment, every halo is the end-product of a merger of exactly two progenitors. Therefore, an N-body simulation may naturally obtain a larger merger rate, black hole growth rate, and mass ratio for typical mergers than an EPS study. On the other hand, our black holes do not experience dynamical friction properly, so this *artificially* increases our merger rate with respect to EPS.

In order to achieve 10^4 $M_\odot$ $\lesssim m_{BH} \lesssim 10^6$ $M_\odot$ (Figure 9c) with EPS models, one must start at higher redshifts and assume higher initial black hole masses. The KBD model starts with high mass seeds, and as a result the KBD merger rates peak for 10^4 $M_\odot$ $\lesssim m_{BH} \lesssim 10^6$ $M_\odot$, and are larger than the N-body rates, both in this mass range and at z>5. We "spend" BH seeds naturally during mergers so in this mass range our peak is $m_{BH} \lesssim 10^4$ $M_\odot$ at z>5.

3.6 DISCUSSION

We used a high-resolution cosmological N-body simulation to study the formation and growth of seed black holes into SMBHs and derived black hole merger rates. We used physically-motivated formalisms for seeding DMHs with black holes. Better understanding of the initial mass function for Population III black holes will improve the accuracy of our results in the future. Of course, black hole seeds do not necessarily have to be Population III black holes. We can use our approach to test different seeding scenarios. For example, it can be used to set constraints for primordial black hole formation (Mack et al. 2006).

Depending on the assumed growth scenario, we showed that gas accretion (90% of SMBH mass growth) combined with hierarchical mergers of massive black holes (10% of SMBH mass growth) leads to the formation of a Sagittarius A* type black hole in the center of a Milky Way-sized DMH. In the case of very efficient gas accretion, an M31-sized SMBH can form. In both cases, SMBH growth is consistent with Soltan's argument (Soltan 1982) that SMBH grow mostly through gas accretion. In our models, the SMBH reaches its final mass at z∼6. We showed that z=6 may be a critical redshift for the transition from the AGN duty cycle dominated by high mass ratio DMH mergers to a starburst galaxy phase, where low mass ratio DMH mergers supply a galaxy with a constant population of ULXs up to z=2. We argue that the z=6 turning point is consistent with the maximum of the AGN luminosity function at z=2 since the SMBHs in our simulation have masses and luminosities below the currently observable range. Also note that potential ULX sources in our simulation are at z>2. They may correspond to nuclear clusters at the centers of dwarf galaxies, and therefore may be likely sites of IMBHs formation. This population is different from the low redshift ULX population which may form from globular cluster dynamics and are likely undergoing short lived binary accretion. Our results are consistent with Lehmer et al. (2006) who predict ∼5-10 ULX sources per galaxy at z∼3. Future very large aperture x-ray satellites, such as Generation-X, may be capable of resolving these sources.

The final stages of the black hole merger are followed by an emission of gravitational radiation, low in frequency but relatively high in amplitude. In one of our follow up papers, for each binary black hole inspiral and merger, the expected gravitational wave signal for the LISA will be determined, and the LISA event rate as a function of time calculated. In particular, we will study whether LISA observations will be able to distinguish between different assembly scenarios. One interesting source we will be able to constrain will be IMBH/SMBH mergers. We will calculate LISA detectability of

IMBH mergers for different mass ranges and binary mass ratios. At this point, rough estimates can be made from Fig. 3.6, considering the known ranges for LISA sensitivity. In case of dry growth (Fig 6g), a black hole binary with mass $10^5\ \mathrm{M}_\odot < \mathrm{m_{BH}} < 10^6\ \mathrm{M}_\odot$ is in the LISA range with a very high merger rate of $\sim$15 yr^{-1}. Interestingly, just as SMBHs dim electromagnetically at z=6, they turn on in the gravitational wavebands.

There are a number of processes that might suppress massive black hole merger rates. We assumed that every first star will produce black hole as opposed to neutron star or pair detonation with no remnant. We also assume that black holes merge efficiently and that recoil ejection which is a function of spin, orientation, eccentricity, and mass ratio of merging black holes is negligible. All of these processes will be addressed in the follow up paper.

Finally, since our $O(10^6)\,\mathrm{M}_\odot$ black hole was in place so early, it might be tempting to interpret our results as an indictment against downsizing, the recent observation that the number density of low mass AGNs peaks at $z < 1$ (Cowie et al. 2003; Merloni 2004; Heckman et al. 2004). However, we caution that in order to achieve such high mass resolution, we simulated a small volume, and are therefore plagued by small number statistics. In fact, if we were to scale our simulation up in mass, so that the most massive SMBHs were $O(10^{10})\,\mathrm{M}_\odot$, we find some indication that the more isolated DMHs will host low mass SMBHs that gain most of their mass at late redshifts compared to the most massive SMBH. We are exploring the growth of black holes as a function of environment and smooth accretion efficiency in a follow up paper.

This simulation has not been tested for cosmic variance which can change the merger rate's profiles dramatically. In order to do this, we are planing a new simulation in a larger cosmological volume. In this manner, we will also test if our results are dependent on the size of simulated cosmological volume.

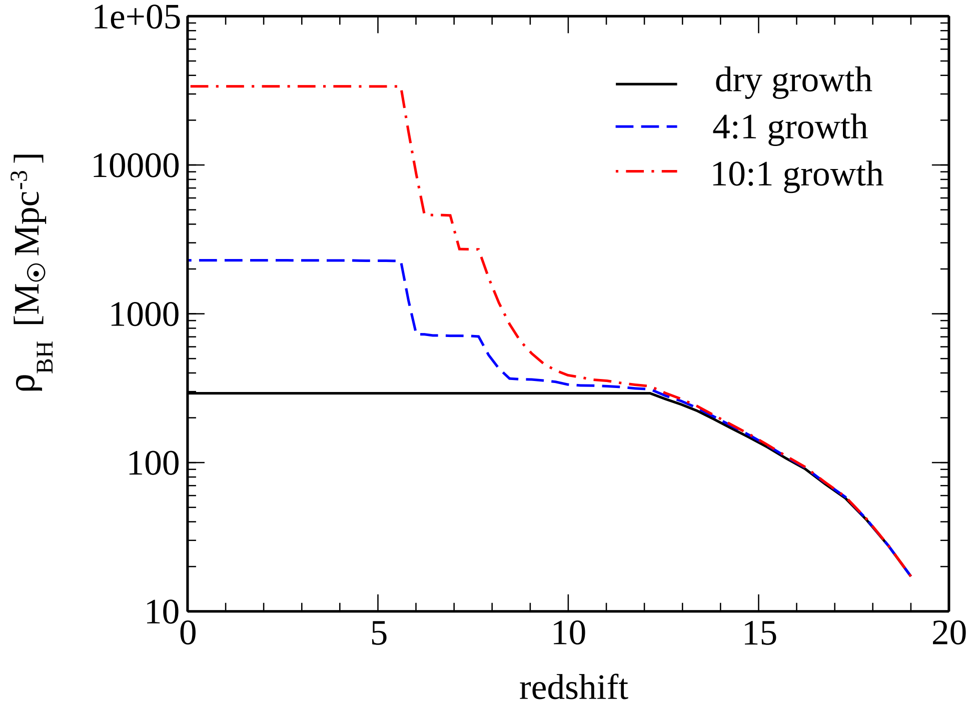

Fig. 3.1 Black hole mass density as a function of redshift. The largest black hole at redshift z=0 is in the 10:1 growth model, and has mass 3×10^7 $M_\odot$. Since we are testing low mass end of SMBH formation, we obtain black hole mass densities well bellow the observed values.

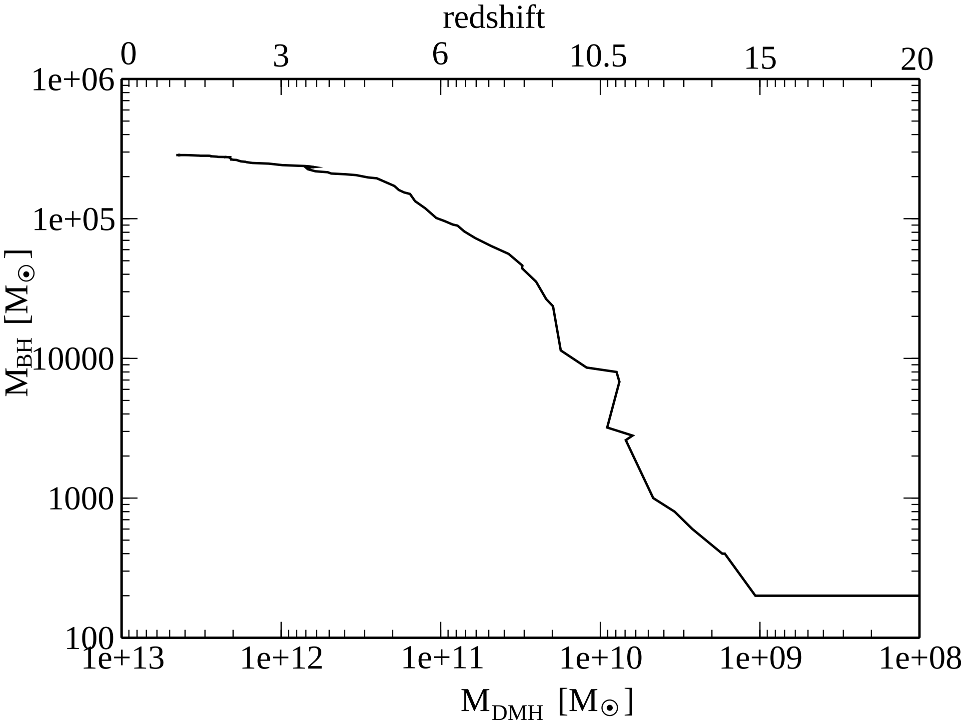

Fig. 3.2 Mass of the SMBH at the center of primary halo as a function of primary halo's mass. The redshift dependence is qualitative only as primary looses a substantial amount of mass at periods of high merger rate. The growth of primary halo and any other DMH can be described as a cycle of steady accretion of the surrounding dark matter followed by rapid growth through mergers with incoming DMHs. This process is best observed at z=11.

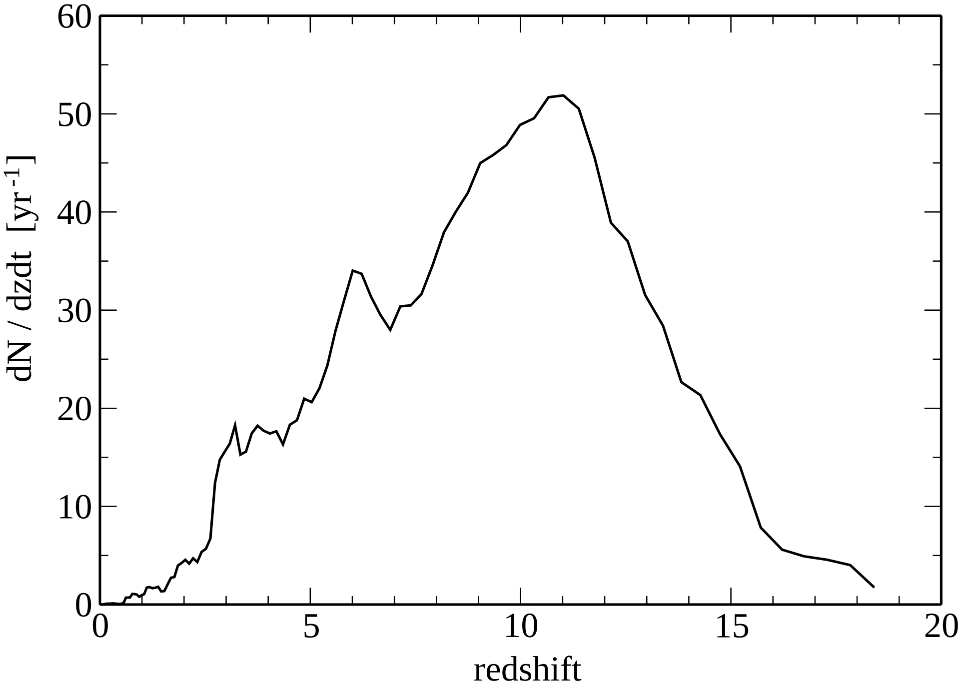

Fig. 3.3 Merger rates per unit time per unit redshift observed at z=0 as a function of redshift. Merger rates reach maximum at z=11, decrease at redshifts z$\lesssim$10 but experience two more peaks with periods of violent mergers around redshifts z=6 and z=3.

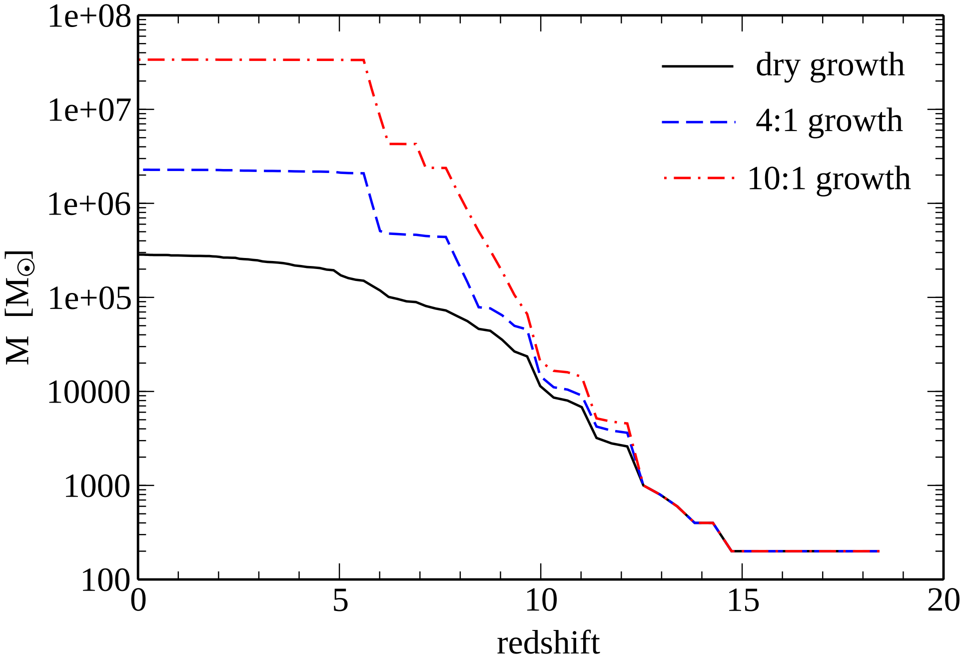

Fig. 3.4 Growth of SMBH in three different accretion scenarios presented as mass of the SMBH as a function of redshift. Black hole mergers are dominant way of growing IMBH at z$\gtrsim$12. Gas accretion is important at 6$\lesssim$z$\lesssim$12. At redshift z=6, SMBH reaches the maximum mass marking the transition of its host AGN into the starburst galaxy.

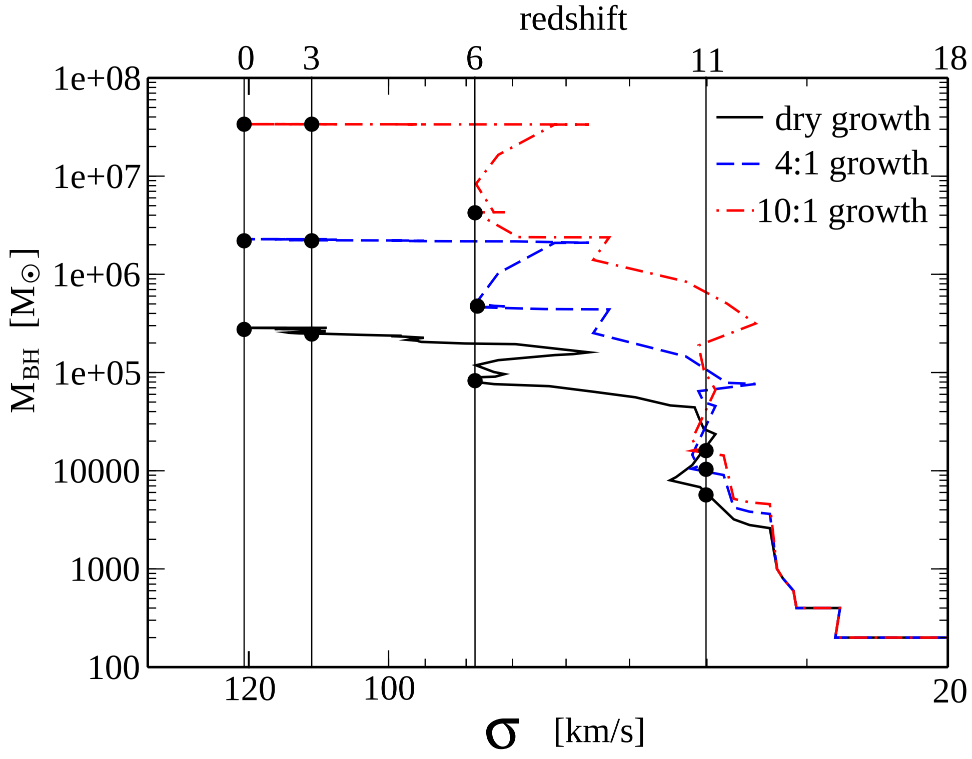

Fig. 3.5 Growth of SMBH in three different accretion scenarios presented as mass of the SMBH as a function of dark matter central velocity dispersion at r=10kpc (σ), and as a function of redshift. Redshift dependence is descriptive, hence filled circles correspond to data points in terms of redshift. Velocity dispersion is σ=120 km^{-1} at z=0 and it fits the M-σ relation for 10:1 growth accretion.

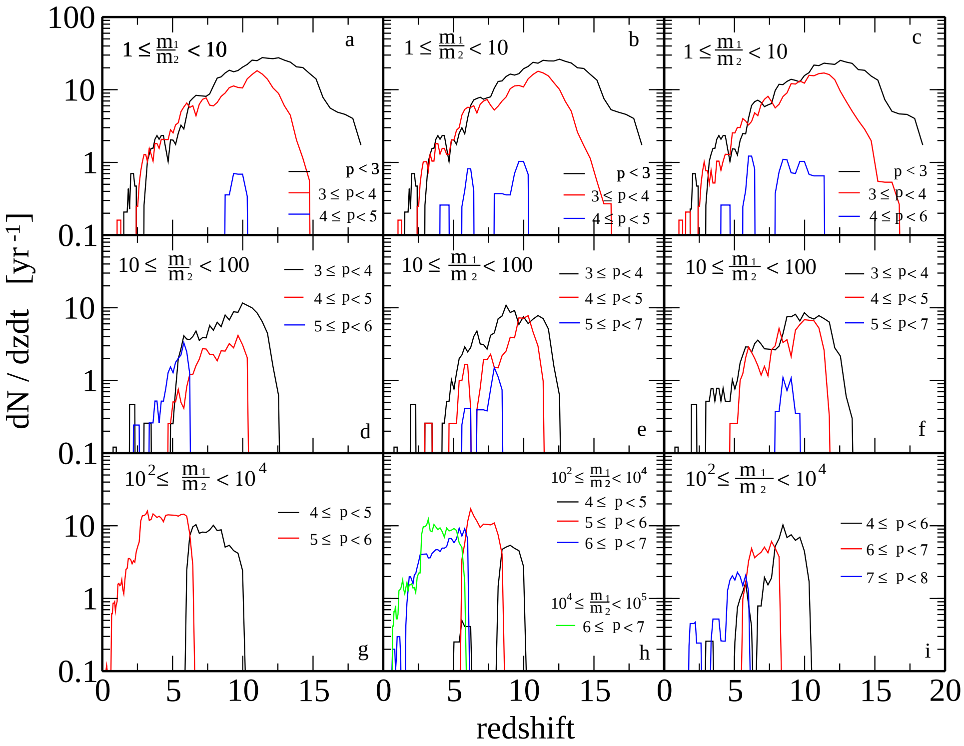

Fig. 3.6 IMBH merger rates as observed at z=0 as a function of redshift and presented for different binary mass ratios and total binary mass ranges, $p = \log\ (m_1 + m_2)$. $1 \lesssim m_1/m_2 < 10$ in a, b, c; $10 \lesssim m_1/m_2 < 100$ in d, e, f; $100 \lesssim m_1/m_2 < 10000$ in g, h, i; dry growth in a, d, g; 4:1 growth in b, e, h; 10:1 growth in c, f, i. Most of the mergers are low mass ratio mergers at z>10 . However, high mass ratio mergers at z<10 (g, h) are in the LISA range and have large merger rates $R \sim 15\ \mathrm{yr}^{-1}$ for a wide range of redshifts $2 < z < 10$.

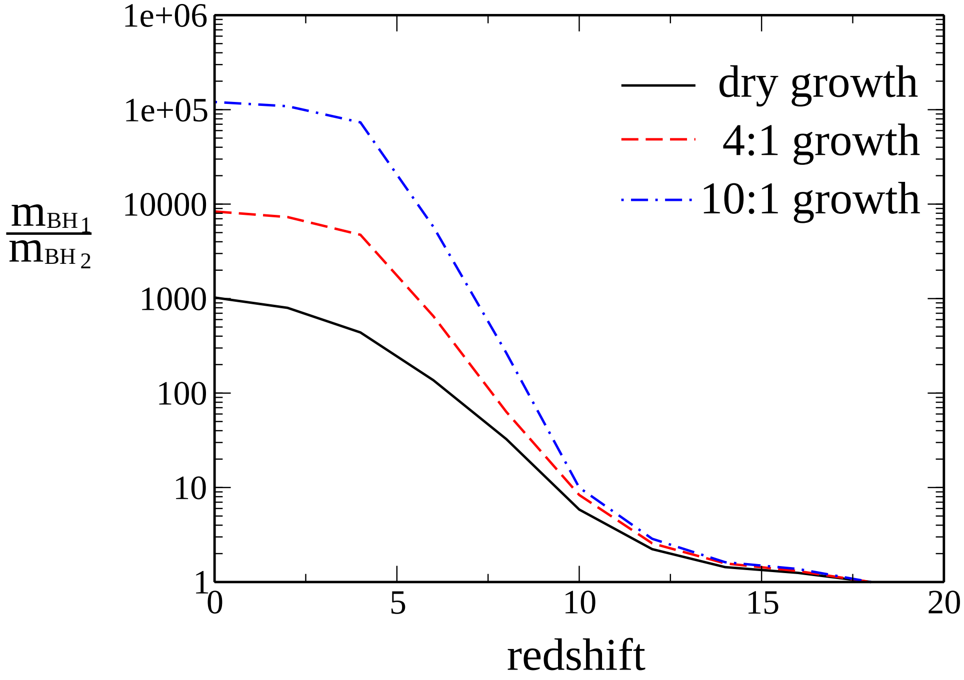

Fig. 3.7 Mass ratio of merging black holes averaged over all mergers at a specific redshift for all three growth models. Black holes grow mostly through mergers at $z > 10$. Differences between three growing models become apparent at $z < 10$ where the increase in mass ratio of merging black holes is due to gas accretion.

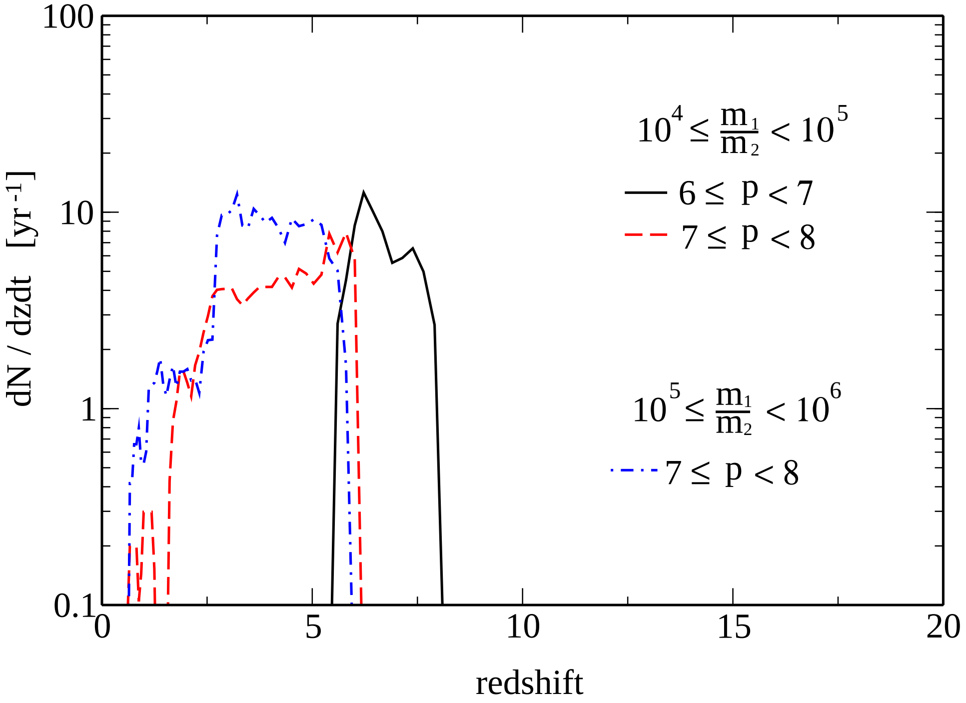

Fig. 3.8 Merger rates observed at z=0 as a function of redshift, presented is the case of 10:1 growth scenario and merger rates for large binary mass and extreme binary mass ratios, $p = \log{(m_1 + m_2)}$. Similar to Figure 5g and 5h, mergers of SMBH with IMBH at $z > 2$ will be observed by LISA, $R \sim 10$ yr^{-1}.

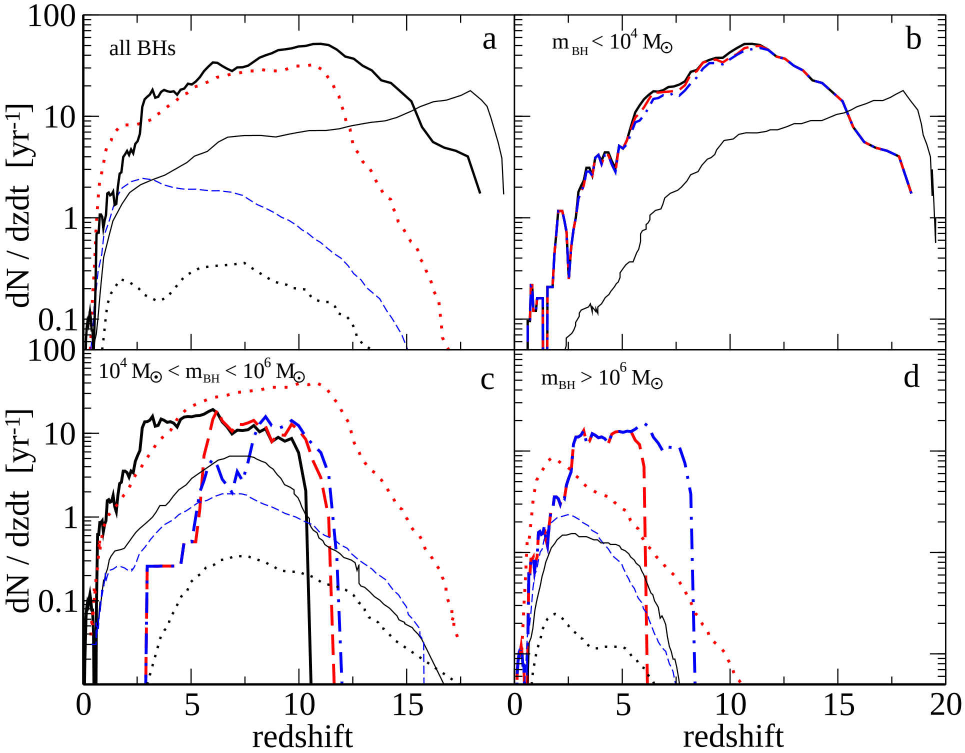

Fig. 3.9 Merger rates observed at z=0 as a function of redshift in different binary mass intervals $m_{BH}=m_1 + m_2$ for four models described in Sesana et al. 2007, VHM in thin black line; KBD in dot-red line; BVRlf in blue-dashed line and BVRhf in black-dot line. Overplotted are merger rates from our N-body simulations for dry growth in thick black line; 4:1 growth in red dashed line and 10:1 growth in blue dashed-dot line. We predict massive black hole merger rates to be larger than those predicted by semi-analitical models in the range $2 < z < 15$. Numerical simulations also depict episodes of violent DMH dynamics which can be seen in multiple peaks at z=11; z=6; and z=3.

Chapter 4

LISA Observations of Supermassive Black Hole Growth

4.1 Introduction

In current theories of structure formation, the first generation of stars forms at redshifts z $\gtrsim$ 12. The seeds of these Population III stars are black holes with masses $\lesssim$ 10^3 $M_\odot$ lying deep within the potential of forming galaxies (Heger et al. 2003; Volonteri et al. 2003; Islam et al. 2003; Wise & Abel 2005; Abel et al. 2000, 2002). Soon after, these seed black holes sink to the centers of their host galaxies. The mergers of galaxies provide an impetus for these black holes to meet and form a bound system. In time, black holes merge and form more massive black holes which accrete gas, and continue their growth. During a galaxy merger, each black hole sinks to the center of the new galaxy potential due to dynamical friction and eventually becomes bound as a binary (Kazantzidis et al. 2005; Escala et al. 2005). Dynamical friction then continues to shrink the orbit until the binary is hard (i.e, the separation between each black hole, a_{BBH}, is such that the system tends to lose energy during stellar encounters) (Heggie et al. 2006). Thereafter, further decay is mediated by 3-body scattering with the ambient stellar background until the binary becomes so close that the orbit can lose energy via gravitational radiation. In studies of a static, spherical potential, it may be difficult for stellar encounters alone to cause the binary to transition between the 3-body scattering phase and the gravitational radiation regime. However, in gas-rich or non-axisymmetric systems the binary hardens efficiently into one that emits copious gravitational radiation (Berczik et al. 2006; Sigurdsson 2003; Holley-Bockelmann & Sigurdsson 2006).

Gravitational waves emitted during inspiral phase (Blanchet 1996) carry information about the masses and spins of the two black holes, some of the orbital elements of the binary, and the distance to the binary (Thorne 1989, 1995b). The inspiral is followed by the plunge phase (Kidder et al. 1993; Ori & Thorne 2000; Lai & Wiseman 1996) which brings information about the dynamics of relativistic gravity in a highly nonlinear, highly dynamic regime. In the final ringdown phase, when one new black hole is formed, gravitational waves carry information about the mass and spin of the final black hole (Teukolsky & Press 1974; Chandrasekhar & Detweiler 1975; Chandrasekhar 1984) . Depending on the black hole mass, these final stages of coalescence emit so much gravitational radiation that they are extremely likely to be detected by the Laser Interferometer Space Antenna (LISA) (Araújo et al. 2007), a planned NASA/ESA mission to detect gravitational waves. It is expected that most of the observable events will be at redshifts 2 $\lesssim$ z $\lesssim$ 7 (Sesana et al. 2004). This means that LISA can be used to map the distribution of black holes as the universe evolves.

Current estimates of the total gravitational wave signal from the cosmological growth and merger lifecycle of black holes have been made using semianalytical models of merger trees, combined with analytic prescriptions for both the black hole merger timescale and gas accretion (Haehnelt 1994; Menou et al. 2001; Wyithe & Loeb 2003; Sesana et al. 2004; Rhook & Wyithe 2005; Sesana et al. 2007). In this study, we use a hybrid method that combines high resolution cosmological N-body simulations for the dark matter halos' merger history with semi-analytical recipes for the black hole dynamics and gas accretion. We track the assembly of black holes over a large range of final masses – from seed black holes to SMBHs – over widely varying dynamical histories. We used the dynamics of dark matter halos to track the evolution of seed black holes in three different gas accretion scenarios. Details of this work can be found in Micic et al. (2007). We use this method to more accurately model different black hole growth scenarios, which will yield different gravitational wave signatures.

After presenting the expected gravitational wave signals from massive black holes mergers in a cosmological context, we proceed with studying the suppression mechanisms to black holes merger rates in the second part of this chapter. The expected gravitational wave signature might be substantially suppressed by various processes which control every black hole merger. We focus on three of the most important: the efficiency of seed black hole formation; gravitational recoil as the result of the merger; and the efficiency of forming black hole binaries through dynamical friction.

It is expected that only a fraction ($\mathrm{f_{POPIII}}$) of first stars collapse into massive black holes. First stars in mass ranges $30\ \mathrm{M_\odot} \lesssim \mathrm{M_{POPIII}} \lesssim 140\ \mathrm{M_\odot}$ and $\mathrm{M_{POPIII}} \gtrsim 260\ \mathrm{M_\odot}$ collapse directly into a black hole. For the first stars with initial mass in range $140\ \mathrm{M_\odot} \lesssim \mathrm{M_{POPIII}} \lesssim 260\ \mathrm{M_\odot}$ pair instability supernovae occurs and the star disperses leaving no remnant (Heger & Woosley 2002). Calculation of $\mathrm{f_{POPIII}}$ would be trivial if the POP III initial mass function is known. Unfortunately, the IMF of the first stars is still very uncertain, mostly because the primordial fragmentation process is still very poorly understood (Nakamura & Umemura 2001; Omukai & Yoshii 2003). If the IMF for the first stars were top heavy (Schneider et al. 2002), ~ 6 % of the total mass in first stars would go into black holes after supernovae collapse. Since half of the mass of each individual first star is ejected during a supernovae (Heger & Woosley 2002), ~ 12 % of first stars produce black hole. We adopt $\mathrm{f_{POPIII}} = 0.1$. Efficiency in seed production is not a function of host halo mass, hence it is expected that merger rates would be suppressed over all redshifts.

The anisotropic emission of gravitational waves which carries away linear momentum from the black hole binary can cause the recoil in the velocity of the final black hole. The first analytical estimates have placed recoil velocity (kick) in the range 10-300 $\mathrm{km\,s^{-1}}$, with the largest recoils smaller than 500 $\mathrm{km\,s^{-1}}$ (Fitchett 1983; Fitchett & Detweiler 1984; Wiseman 1992; Favata et al. 2004; Blanchet et al. 2005; Baker et al. 2006; Damour & Gopakumar 2006). But the recent series of breakthroughs in numerical relativity made it possible to accurately calculate gravitational waveforms for binary black holes mergers and consequent recoil velocities (Herrmann et al. 2007; González et al. 2007a,b; Koppitz et al. 2007; Campanelli et al. 2007b). The amplitude of the kick varies substantially depending on black hole binary orbital configuration and the mass ratio of merging black holes (q). For nonspining, unequal mass binaries with aligned spin axes, the resulting kick is $\mathrm{v_{kick}} \lesssim 90\ \mathrm{km\,s^{-1}}$ (González et al. 2007b); $\mathrm{v_{kick}} \lesssim 500\ \mathrm{km\,s^{-1}}$ for anti-aligned spin axes. Inclusion of spins increases kicks up to $\sim$200 $\mathrm{km\,s^{-1}}$ while in the extreme case of fast spinning black holes, where spin vectors have opposite directions and are in the orbital plane, kicks can be as large as $\sim 4000\ \mathrm{km\,s^{-1}}$ (Campanelli et al. 2007b; González et al. 2007a; Schnittman & Buonanno 2007). Kicks are largest in all of these cases for $0.4 \lesssim \mathrm{q} \lesssim 1$. $\mathrm{q} \sim 1$ dominates high redshift black hole binaries which coalesce at the centers of low mass dark matter halos.

The effect of large kicks combined with low escape velocity from the centers of small dark matter halos at high redshift plays a major role in suppressing the growth of black hole seeds into SMBH. Even the most massive dark matter halo at redshift z$\geq$11 can not retain a black hole that receives $\geq$ 150 $\mathrm{km\,s^{-1}}$ kick (Merritt et al. 2004).

Dynamical friction (Binney & Tremaine 1987) is another mechanism that might suppress SMBH growth. Unlike gravitational recoil which will dominate the outcome of high redshift black hole mergers, dynamical friction is likely to suppress black hole merger rates at low redshifts. When two galaxies merge, the smaller mass galaxy could lose a substantial amount of its mass due to tidal striping. A black hole carried by this galaxy would be deposited into the larger galaxy, and sink toward the center as the "naked" black hole. Dynamical friction is efficient in bringing two black holes together in smaller galaxies with small velocity dispersion. However, the dynamical friction time for massive low redshift galaxies will be larger than the Hubble time, and the black hole binary will not form.

We present our simulation and the method in section 4.2.; gravitational wave signals from black hole mergers in section 4.3.; and suppression mechanisms for black hole merger rates in section 4.4. We discuss our result in the last section.

4.2 Method

4.2.1 Simulation Setup

In our numerical simulations, we use GADGET (Springel et al. 2001b) to evolve a comoving 10 Mpc^3 section of a ΛCDM universe (Ω_{M}=0.3, Ω_Λ=0.7, σ_8=0.9 and h=0.7) with periodic boundary conditions from $z = 40$ to $z = 0$. We refine a sphere of 2 Mpc in the box to simulate at a higher resolution with 4.9$\times10^6$ high-resolution particles (softening length 2 kpc comoving). The rest of the box has 2.0$\times10^6$ low-resolution particles (softening length 4 kpc comoving). The mass of each high resolution particle in this simulation is 8.85$\times10^5\mathrm{M}_\odot$, and the mass of each low-resolution particle is 5.66$\times10^7\mathrm{M}_\odot$. A detailed description of this simulation can be found in a previous chapter.

4.2.2 Analysis

Identification of dark matter structures has been performed by the P-GroupFinder algorithm (Springel et al. 2001a) combined with overdensity algorithm (Lacey & Cole 1994; Warren et al. 1992). The Friend-Of-Friends (FOF) linking length is set to 0.1. Substructures are identified by the SUBFIND algorithm. We seed 200 $\mathrm{M}_\odot$ black hole tracers into $\mathrm{M}_{\mathrm{vir}}\gtrsim10^8\ \mathrm{M}_\odot[(1+\mathrm{z})/10]^{-1.5}$ dark matter halos at 12$\lesssim$z$\lesssim$19. Seeding is followed by the construction of the merger tree for dark matter halos and the black holes until redshift z=0. We study three models for SMBH growth. First, the "dry growth" through mergers of massive black holes only. Second is the "4:1 growth" which is the combination of dry growth with Salpeter gas accretion onto the final black hole following the merger of dark matter halos with mass ratio $\lesssim$ 4:1. The third case is "10:1 growth" where the mass ratio of merging galaxies allowing the black hole accretion must be $\lesssim$ 10:1. Details of this method and the results can be found in previous chapter.

4.3 Gravitational Wave Radiation from Coalescing Black Holes

Two black holes will form a hard binary if dynamical friction and 3-body scattering are efficient in depositing them to the center of galaxy after the galaxy merger. For a black hole binary with components masses M_1 and M_2, separation at which emission of gravitational waves becomes efficient is:

$$a_{gw} = 0.0014\mathrm{pc}[\frac{M_1 M_2 (M_1 + M_2)}{10^{18.3} {M_\odot}^3}]^{1/4} {t_g}^{1/4} \tag{4.1}$$

where $\mathrm{t}_g{}^{1/4}$ is the coalescence timescale in Gyr ($\mathrm{t}_g \sim 1$ Gyr). The theory of gravitational wave emission and all derivations come from Blanchet (1996); Quinlan (1996); Maggiore (2000); Schutz & Ricci (2001). Emitted gravitational radiation carries away angular momentum and orbital separation shrinks even more.

Following the approach of Sesana et al. (2004), a black hole binary begins emitting at frequency:

$$f_{min} = \frac{1}{\pi} \frac{G(M_1 + M_2)^{1/2}}{a_{gw}^3} \tag{4.2}$$

while the upper limit is at the radius of the closest stable circular orbit for two nonrotating black holes:

$$f_{max} = \frac{c^3}{14.7 \pi G} \frac{(M_1 + M_2)^{1/2}}{M_1^{3/2}} \tag{4.3}$$

The characteristic strain h_c is the accumulated signal over time in a certain frequency range obtained by counting the number of events per frequency bin. For a periodic signal with a finite duration with strain amplitude h, the total energy carried by the wave will be proportional to the number of wave cycles n spent at the particular frequency, $\mathrm{h}_c \sim \mathrm{h}\ \mathrm{n}^{1/2}$ where h_c is:

$$h_c(f_r) = \frac{8 \pi^{2/3} G^{5/3} {M_{chirp}}^{5/3} {f_r}^{2/3}}{10^{1/2} c^4 d(z)} \tag{4.4}$$

and $\mathrm{M_{chirp}} = (\mathrm{M_1 M_2})^{3/5} (\mathrm{M_1{+}M_2})^{-1/5}$. When the binary is close to the innermost stable circular orbit (ISCO) the rate at which frequency changes becomes comparable to the frequency itself, and the number of cycles spent in a certain frequency range decreases. As the result characteristic strain becomes comparable to the strain amplitude, $\mathrm{h}_c \sim \mathrm{h}$. The true observable gravitational signal is the maximum characteristic strain for the orbit that has the minimum rate of frequency change.

Knowing the distance to binary black hole at each redshift, we model $\mathrm{h_{c,max}}$ for every merger and obtain the cosmological distribution of gravitational wave signals for black hole mergers. Fig. 4.1 and Fig. 4.2 show $\mathrm{h_{c,max}}$ for each individual merger in our simulation as a function of redshift. Most of the black hole growth is conducted through mergers at high redshifts, $\mathrm{z} \gtrsim 10$. That is why at these redshifts the dry growth model and the 10:1 growth model can not be distinguished. Low mass ratio mergers dominate high redshifts z $\gtrsim$ 10 and for these mergers $h_{c,max}$ is comparable in both cases, dry growth in Fig. 4.1 and 10:1 growth in Fig. 4.2. At redshift z $\lesssim$ 10, gas accretion starts dominating the growth of black holes and supermasive black hole forms at redshift z=6 in the case of 10:1 growth. The increase in signal in Fig. 4.2 at low redshifts is the consequence of already formed supermassive black hole merging with $\lesssim 1000\ M_\odot$ black holes at redshifts z $\lesssim$ 6 in the case of 10:1 growth. Throughout in both figures, signals from different mergers group in streams. This is a consequence of the formation of 2-3 very massive black holes which dominate the merger tree. Most of the mergers are low mass ratio mergers between these very massive black holes and seed black holes.

In the last stages of a merger, the characteristic strain becomes comparable to the strain amplitude as the shift in frequencies starts occurring in less than an orbit. The final orbit is followed by the burst of gravitational radiation described by the strain amplitude h_{max} and presented in Fig. 4.3 for dry growth model and Fig. 4.4 for 10:1 model. Each panel corresponds to the specific redshift. Note that the strain amplitude in the 10:1 model does not increase. An increase might be expected since the mass of the black hole binaries is substantially larger, but the increase in binary mass leads to the decrease in frequency f_r and as the result, the strain amplitude has the same value as in the dry model. Fig. 4.4 shows this shift in signal toward lower frequencies. Even at low redshift and largest binary masses, gravitational waves that come in the form of bursts are not in the LISA range hence the observations must focus on maximum accumulated signal $h_{c,max}$, at the time of ISCO, presented in Fig. 4.5 and Fig. 4.6. Unlike the strain amplitude, where the increase in binary mass is compensated by the decrease in frequency, the characteristic strain is accumulated signal in a frequency range. Although the frequency decreases, the characteristic strain increases due to binary mass.

The resulting gravitational wave background (GWB) is shown in Fig. 4.7 where h_c is integrated for all mergers in the dry model and the 10:1 model compared to the LISA sensitivity curve. h_c in the 10:1 model is well inside the LISA range while gravitational waves will be detected by LISA even in the case of black holes merging without growth through gas accretion. For the dry growth model the signal might be obscured by the Galactic white dwarf binary population. The maximum h_c is at $\sim 10^{-18}$ in the dry model. We predict that the strongest signal from black hole mergers that LISA will detect will be in the characteristic strain range $\sim 10^{-18} \lesssim h_c \lesssim \sim 10^{-16}$. If LISA detects gravitational wave radiation from binary black holes at a characteristic strain higher then $\sim 10^{-18}$, it would mean that gas accretion plays important role in the growth of massive black holes. However, detecting $h_c \gtrsim \sim 10^{-16}$ would be surprising since 10:1 model includes the upper constraint on the efficiency of gas accretion. The contribution to the gravitational wave radiation from massive black hole binaries in different redshift ranges is depicted in Fig. 4.8 and Fig. 4.9. Mergers at redshifts z $\lesssim$ 5 are in the LISA range with an expected strong signal for massive binaries.

4.4 Suppression Mechanisms in SMBH growth

From the moment two galaxies start merging to the time the black holes they carry at their centers coalesce, a number of processes might prevent formation of one final massive black hole. We need to know how many galaxies will be seeded with massive black holes. Dynamical friction leads the galaxy merger and brings black holes close so they can form a binary. To form a hard black hole binary, 3-body scattering with stars must be effective, too. Even if the black holes merge, their end product might be ejected from the galaxy through gravitational recoil. It is important to incorporate these processes into the calculation of the black hole merger rate over Hubble time and estimate the effect on expected gravitational wave signal.

4.4.1 Black Hole Seeds Formation Rate

As already mentioned in the introduction, the detailed physics behind first stars provides a very accurate picture of final stages of evolution of Pop III stars. Stars with initial mass $30\ \mathrm{M}_\odot \lesssim \mathrm{M}_{\mathrm{POPIII}} \lesssim 140\ \mathrm{M}_\odot$ and $\mathrm{M}_{\mathrm{POPIII}} \gtrsim 260\ \mathrm{M}_\odot$ collapse directly into a black hole (Heger & Woosley 2002). Stars at a lower mass end form a neutron star and stars with $140\ \mathrm{M}_\odot \lesssim \mathrm{M}_{\mathrm{POPIII}} \lesssim 260\ \mathrm{M}_\odot$ go through pair instability supernovae leaving no remnant. The lack of understanding of fragmentation of primordial molecular hydrogen gas clouds prevents reproducing the first stars IMF. It is expected that the IMF is top heavy since the accretion rate onto the first stars is large (Stahler et al. 1986; Omukai & Nishi 1998; Ripamonti et al. 2002) and the dust grains are absent in H_2 gas clouds, hence the radiative feedback from the forming star is not strong enough to halt further gas accretion (Omukai & Palla 2003; Bromm & Loeb 2004). The latest constraint of the first star's maximum mass comes from the modeling of the structure of the accretion flow and evolution of protostars and sets the maximum mass to $\sim 300\ \mathrm{M}_\odot$. It is unlikely that the Pop III IMF is anything like Salpeter IMF (power law with -2.35 slope) which is the IMF for the present day stellar populations.

The fraction of the first stars which produce massive black holes could be as low as 10 %, $\mathrm{f}_{\mathrm{POPIII}} = 0.1$, (Schneider et al. 2002). We do note that 10% is a lower constraint and that much higher efficiency would not be unexpected. Since the formation of the first stars is only limited by the minimum mass of the host dark matter halo (Wise & Abel 2005), there is no correlation between the masses of first stars and the masses of their host halos. We randomly select 10% of dark matter halos which can host seed black holes and remove the rest of the seeds from our merger tree. After one hundred realizations which randomly select host halos, we obtain new merger rates presented in Fig. 4.10 Since the number of seeds is ten times lower than in the case of fully efficient formation, the merger rates are depleted at all redshifts. Nevertheless, the maximum merger rate of ~ 10 at redshift $z \sim 6$ is only five times lower than the previous (~ 50 at redshift $z \sim 11$). This is still considered to be a rather large merger rate which is in the LISA range.

The total characteristic strain in Fig. 4.7 is dominated by the rare bright mergers. For that reason, even though a lot of events disappear when efficiency in forming seeds is included, the h_c stays relatively high in both dry and 10:1 models, Fig. 4.11. The change in h_c is more pronounced in the 10:1 growth as the difference in masses of merging black holes increases when gas accretion is added in combination with mergers.

4.4.2 Effects of Dynamical Friction

The dynamical evolution of two merging halos/galaxies is driven by the combined effect of dynamical friction that brings the less massive galaxy (satellite) to the center of the larger halo (primary), and the tidal interaction which strips mass from the satellite (Taffoni et al. 2003). We define mass ratio of merging halos as $\mathrm{Q} = \mathrm{M}_1/\mathrm{M}_2$, where M_1 is the mass of the primary, M_2 is the mass of the satellite, and $\mathrm{M}_1 \gtrsim \mathrm{M}_2$, $\mathrm{Q} \gtrsim 1$. The mass ratio of merging black holes is $\mathrm{q} = \mathrm{m}_1/\mathrm{m}_2$, where m_1 is the black hole smaller in mass, m_2 is the black hole larger in mass, and $\mathrm{m}_1 \lesssim \mathrm{m}_2$, $0 \lesssim \mathrm{q} \lesssim 1$. The more mass that is stripped, the less efficient dynamical friction is. If the dynamical friction time is longer then Hubble time, the black holes carried by their host galaxies will not be brought close enough to form binary.

In the case of equal-mass mergers $\mathrm{Q} \sim 1$, the cuspy potentials of both galaxies are deep enough to allow the survival of their inner regions until orbital decay by dynamical friction is complete (White 1983; Taffoni et al. 2003).

In unequal-mass mergers, the outcome depends on the mass ratio of merging galaxies. For high mass ratios $\mathrm{Q} \gg 1$, the satellite (truncated isothermal profile with core (de Blok & McGaugh 1997) in orbit with $\mathrm{e} = 0.8$) will be stripped of half of its mass making the dynamical friction time scale large (Colpi et al. 1999), while for the much smaller satellites all the mass would be fully striped, leaving its black hole wandering at a distance that prohibits the formation of a close pair. This "naked" SMBH would contribute to a population of wandering SMBHs in galactic halos (Volonteri et al. 2003). At such a distance, the timescale for orbital decay predicted by dynamical friction would exceed a Hubble time.

Since the primary is not spherical in reality but actually triaxial, then some fraction of black holes can fall into the inner halo region on time scale $\sim 10\ \mathrm{t}_{orbital}$ due to centerphilic box or boxlet orbits (de Zeeuw 1985; Zhao et al. 2002; Holley-Bockelmann et al. 2005). In such cases, dynamical friction becomes effective in bringing the IMBHs to the halo center. Also, the dynamical friction assumption that satellite orbits are circular is not realistic. Satellites always have a radial component in their velocity relative to the center of primary. This free-falling greatly reduces the merger timescale.

For the circular orbit of a satellite, the timescale for dynamical friction to bring the satellite and associated black hole to the primary halo center is given by Chandrasekhar formula (Binney & Tremaine 1987):

$$t_{fric} = \frac{1.17}{\mathrm{ln}\Lambda} \frac{\mathrm{r}^2 \mathrm{v_c}}{\mathrm{GM}}, \tag{4.5}$$

where $\ln \Lambda$ is the Coulomb logarithm ((Binney & Tremaine 1987), table 7.1), and the satellite of mass M is at the distance r from the center of the primary halo, with associated circular velocity v_c.

We assume that tidal stripping will remove half of the satellite mass and calculate the circular velocity at halo radius R for every merger host (largest halo in the merger) in our merger tree. If the primary halo merges with more then one satellite, we sort satellites according to their mass in descending order, since more massive satellites will merge first.

We calculate Coulomb logarithm for each merger from:

$$\Lambda = \frac{b_{\max} v_c^2}{\mathrm{G(M+m)}} \tag{4.6}$$

where $\mathrm{b_{max}}$ is effective radius. Typical lnΛ is ~ 10. We compare the dynamical friction time to the Hubble time for each merger and if $\mathrm{t_{dyn.fric}} \gtrsim \mathrm{t_{Hubble}}$, we remove the satellite from the merger tree. The new merger rate which incorporates the effects of dynamical friction are presented in Fig. 4.12 (in red color). We compare them to the previous non-suppressed merger rates. As expected, at high redshifts $\mathrm{z} \gtrsim 11$, most of the merging halos have small mass ratios (mergers of comparable sizes $\mathrm{Q} \sim 1$), and the merger rate is not affected since dynamical friction is efficient. At lower redshifts high mass ratio mergers ($\mathrm{Q} \gg 1$) start dominating the dynamics of the each merger and satellites need more time to sink. Consequently, the merger rate decreases almost four times at $\mathrm{z} \sim 5$.

4.4.3 Gravitational Recoil from Black Hole Mergers

The gravitational recoil (kick) that follows the black hole merger is potentially most effective in suppressing black hole merger rates when compared to other suppression mechanisms. The latest works in numerical relativity have made it possible to precisely calculate the magnitude of the kick for the first time (Fitchett 1983; Fitchett & Detweiler 1984; Wiseman 1992; Favata et al. 2004; Blanchet et al. 2005; Baker et al. 2006; Damour & Gopakumar 2006). However, the kick magnitude is largely dependent on the black hole binary orbital configuration and the mass ratio of merging black holes (q). A better understanding of orientation of black hole spin vectors and the magnitude of spins will constrain kicks inside the astrophysical frame.

We assume four kick ranges for various mass ratios of merging black holes obtained by Baker et al. (2006, 2007) and Campanelli et al. (2007b) and presented in Fig. 4.13. For each black hole merger in our simulation we use a kick velocity corresponding to the black hole mass ratio and we calculate the escape velocity from the center of every halo hosting the black hole merger. If the kick is larger than the escape velocity, the black hole binary is removed from the merger tree. The effects of these four models of kicks on black hole merger rates are presented in Fig. 4.14. The lowest kick velocity is in the case of nonspinning black holes with aligned spin axes. Corresponding merger rates are presented in red (K1). Kicks for nonspinning black holes with anti-aligned spin axes have much larger values and corresponding merger rates are presented in green (K2). K3 is the case of spinning black holes with optimal orbital configuration (blue) and K4 (thin black) presents spinning black holes in the orbital configuration that provides largest kick values (fast spinning black holes, where spin vectors have opposite directions and are in the orbital plane). Most of the low mass-ratio mergers of black holes are high redshift mergers since the first black hole binaries to form are made out Pop III seeds and have comparable masses. For exactly this range of mass ratios ($0.4 \lesssim \mathrm{q} \lesssim 1$) kicks have the largest values. In the K1 case most of the black holes are retained, while in the K3 case there is already a substantial decrease in merger rates at redshifts $\mathrm{z} \gtrsim 6$ (~ 50 % of black holes ejected). This is the result of the gravitational potential at the centers of high redshift halos being large enough to retain merging black holes in K1 case (maximum of 90 $\mathrm{km\,s^{-1}}$ for K1). But not in the K3 case (maximum kicks of 200 $\mathrm{km\,s^{-1}}$ for K3). At lower redshifts z $\lesssim$ 6, as the halos grow in mass and their gravitational potential increases, even the kicks in the K3 case can not reach the escape velocity. K2 (maximum kick of 500 $\mathrm{km\,s^{-1}}$) and K4 (4000 $\mathrm{km\,s^{-1}}$) cases completely deplete merger rates at z $\gtrsim$ 5. At z $\lesssim$ 5 it is not the increase in gravitational potential that retains black holes but the high mass ratio mergers for which kicks have small values even in K2 and K4 case.

4.5 Discussion

We have used the massive black hole merger rates obtained from merger trees in high-resolution cosmological N-body simulations to calculate the expected gravitational wave signal from cosmological massive black hole binaries. We also study the suppressive mechanisms expected to either prevent black holes from merging or depopulate the centers of dark matter halos and in this manner decrease expected black hole merger rates.

The integrated characteristic strain over frequencies that defines binary black hole gravitational wave background, is well inside the LISA range. Gravitational Wave Background (GWB) at redshifts z $\lesssim$ 5 will be observable by LISA even in the black hole growth model that assumes no gas accretion. These results are obtained for models that do not incorporate suppression mechanisms.

Seed black hole formation efficiency, dynamical friction, and gravitational recoil are the three most important suppression mechanisms. Dynamical friction prevents black holes from sinking into gravitational potentials of host galaxies and this effect is strongest at low redshifts. Gravitational recoil as the result of black hole mergers depopulates centers of galaxies from black holes mostly at high redshifts where low mass ratio binaries in low gravitational potentials dominate the merger rate. Low efficiency in producing Pop III seed black holes decreases merger rates overall at all redshifts. These three effects combined might cause substantial drop in black hole merger rates changing the picture of how SMBH grow. At redshifts z $\gtrsim$ 12, the new black hole merger rate is R $\lesssim$ 5 $\mathrm{yr^{-1}}$ when the effects of dynamical friction are combined with $f_{\mathrm{POPIII}} = 0.1$. This is valid if the K1 case of kicks is adopted. For extreme range of kicks, K2 and K4, merger rates at z $\gtrsim$ 12 drop to zero. For the redshift range 7 $\lesssim$ z $\lesssim$ 12, and $f_{\mathrm{POPIII}} = 0.1$, the new merger rate is R $\sim$ 8 $\mathrm{yr^{-1}}$. In the same redshift range dynamical friction reduces merger rates $\sim$ 50 %. If we assume the K1 case of kicks, then all three effects combined produce R $\sim$ 4 $\mathrm{yr^{-1}}$; R $\sim$ 2-3 $\mathrm{yr^{-1}}$ if the K3 is assumed; and R $\sim$ 1 $\mathrm{yr^{-1}}$ in K2 and K4 cases. In the same manner, R $\sim$ 1-3 $\mathrm{yr^{-1}}$ at z $\sim$ 6; R $\sim$ 0.3-1 $\mathrm{yr^{-1}}$ for 2 $\lesssim$ z $\lesssim$ 6; and R $\sim$ 0.1-1 $\mathrm{yr^{-1}}$ at z $\lesssim$ 2.

If kicks are as efficient as presented results show, than there might be no M-σ relation which correlates mass of the SMBH and galaxy velocity dispersion (Tremaine et al. 2002; Ferrarese & Ford 2005; Lauer et al. 2007; Valluri et al. 2004). If there are no constraints on the black hole binary orbital configuration, the amplitude of kicks will be randomly driven from theoretical recoil distributions. This would introduce scatter into the M-σ relation.

Fortunately, recent works (Bogdanović et al. 2007) show that in the mergers of gas rich galaxies, torques from the gas that black holes accrete align the orbit and spins of both black holes. This process would constrain kicks to $\lesssim 200\ \mathrm{km\,s^{-1}}$. We have demonstrated that kicks in this range (K1 and K3) would be important at high redshifts only and would only decrease the mass of SMBH at the galaxy center. If the merging galaxies are gas poor, only small fraction of black holes would be ejected (Bogdanović et al. 2007).

Even when the ejection occurs, the primary halo dominates the dynamics of its local group and a large fraction of ejected black holes sinks toward the primary, eventually reaching the center if the dynamical friction is efficient (Micic et al. 2006).

It is important to understand how all these processes influence the black hole merger rates. Better treatment of the dynamical friction and black hole binary orbital configuration is necessary in order to constrain kick ranges. Our future simulations will address the dynamical friction issue better since we will introduce much higher spatial and mass resolution. Also, as the simulations of the formation of first stars are including increasingly more physics, the fragmentation process of H_2 clouds will be better understood and accurate IMF will be obtained, which will constrain seed black hole formation efficiency.

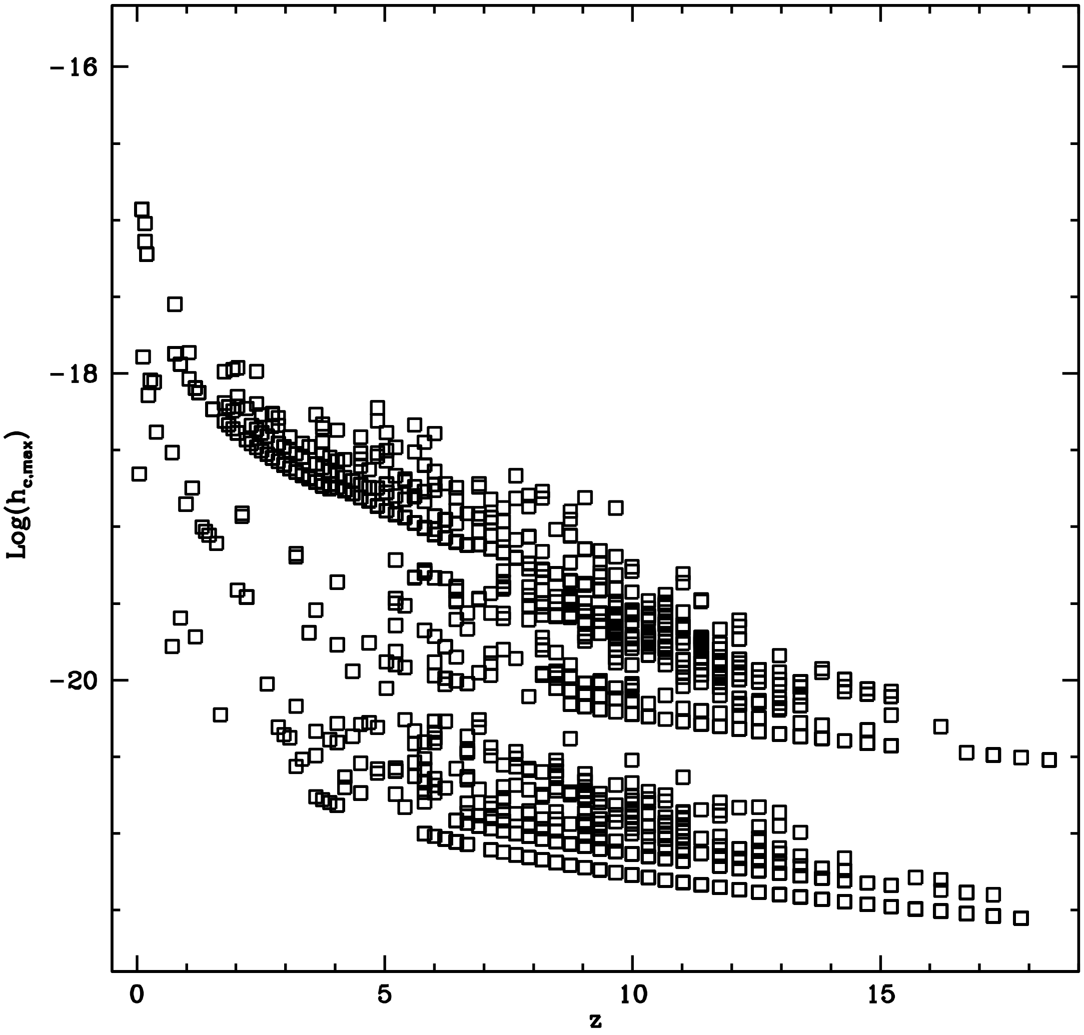

Fig. 4.1 The maximum characteristic strain for all mergers in our simulation as a function of redshift. For the case of dry growth of SMBH. The maximum characteristic strain corresponds to the strongest gravitational wave signature at the most stable orbit.

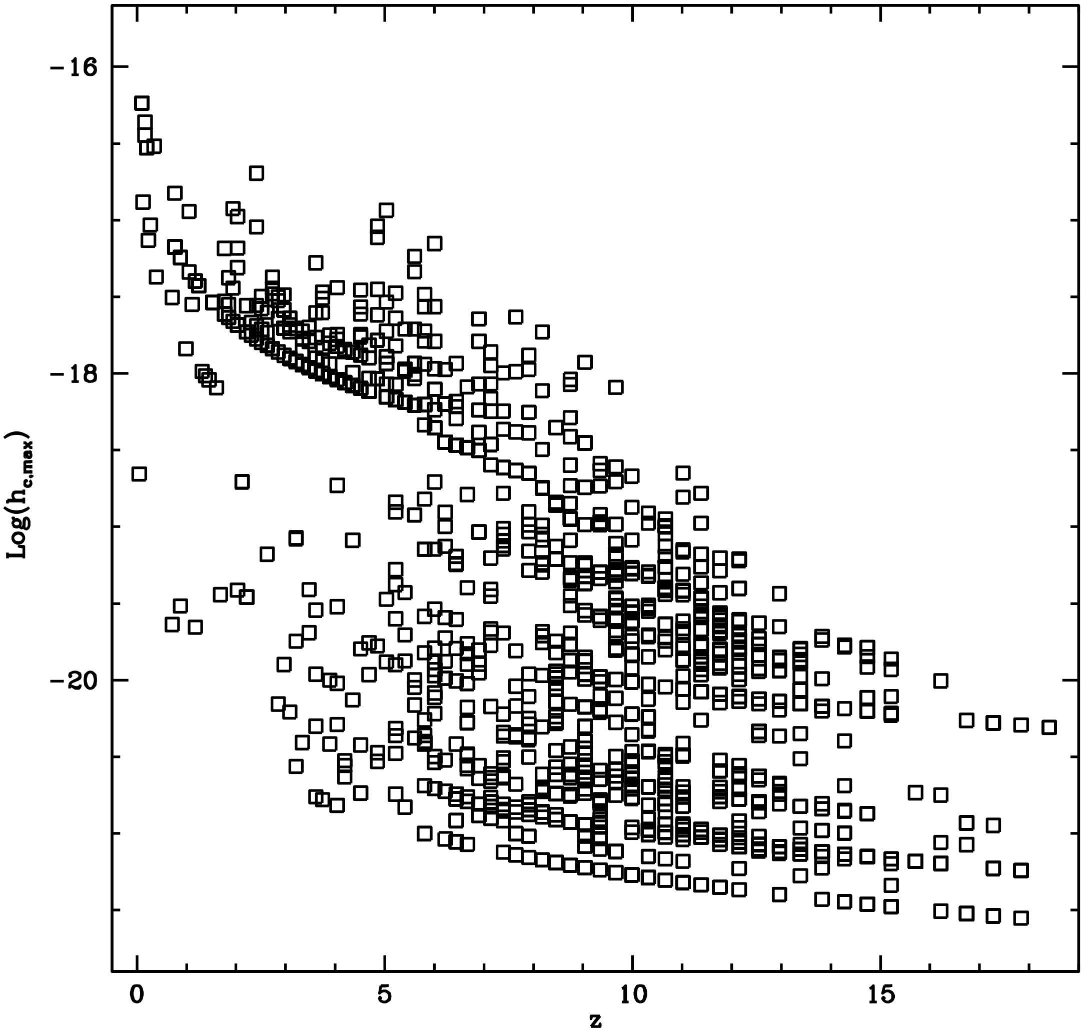

Fig. 4.2 The maximum characteristic strain for all mergers in our simulation as a function of redshift. For the case of 10:1 growth of SMBH. The maximum characteristic strain corresponds to the strongest gravitational wave signature at the most stable orbit.

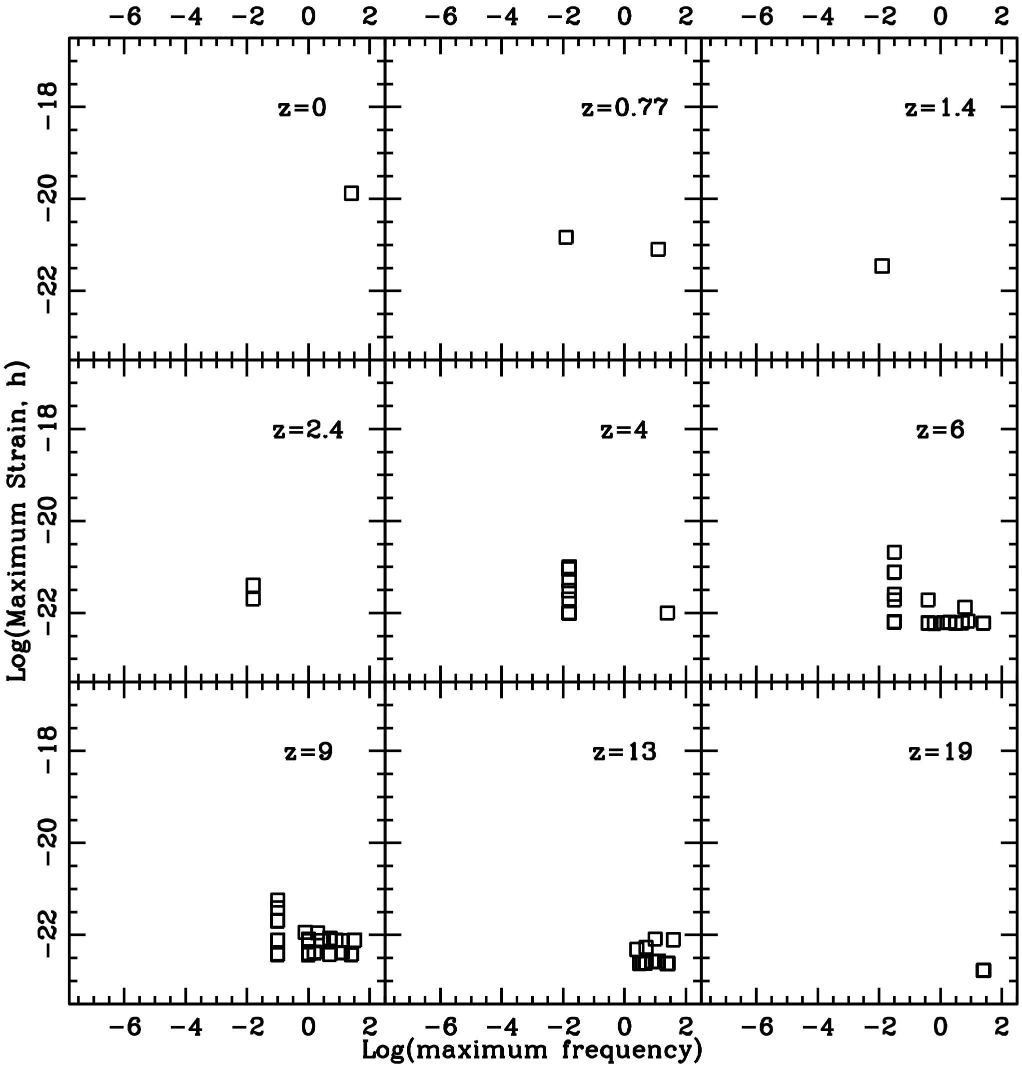

Fig. 4.3 The maximum strain amplitude at various redshifts as a function of maximum frequency. For the case of dry growth of SMBH. The maximum strain amplitude corresponds to the burst at the last orbit.

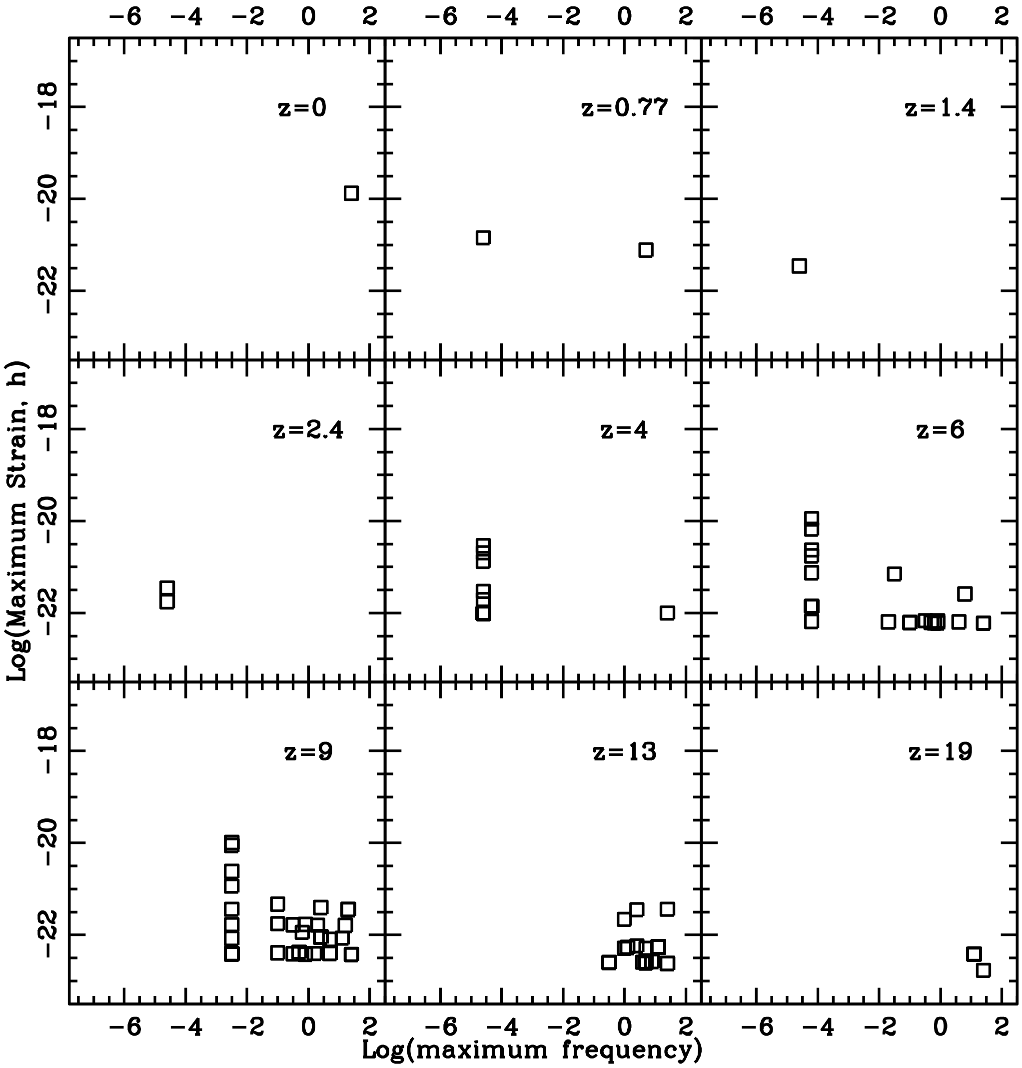

Fig. 4.4 The maximum strain amplitude at various redshifts as a function of maximum frequency. For the case of 10:1 growth of SMBH. The maximum strain amplitude corresponds to the burst at the last orbit.

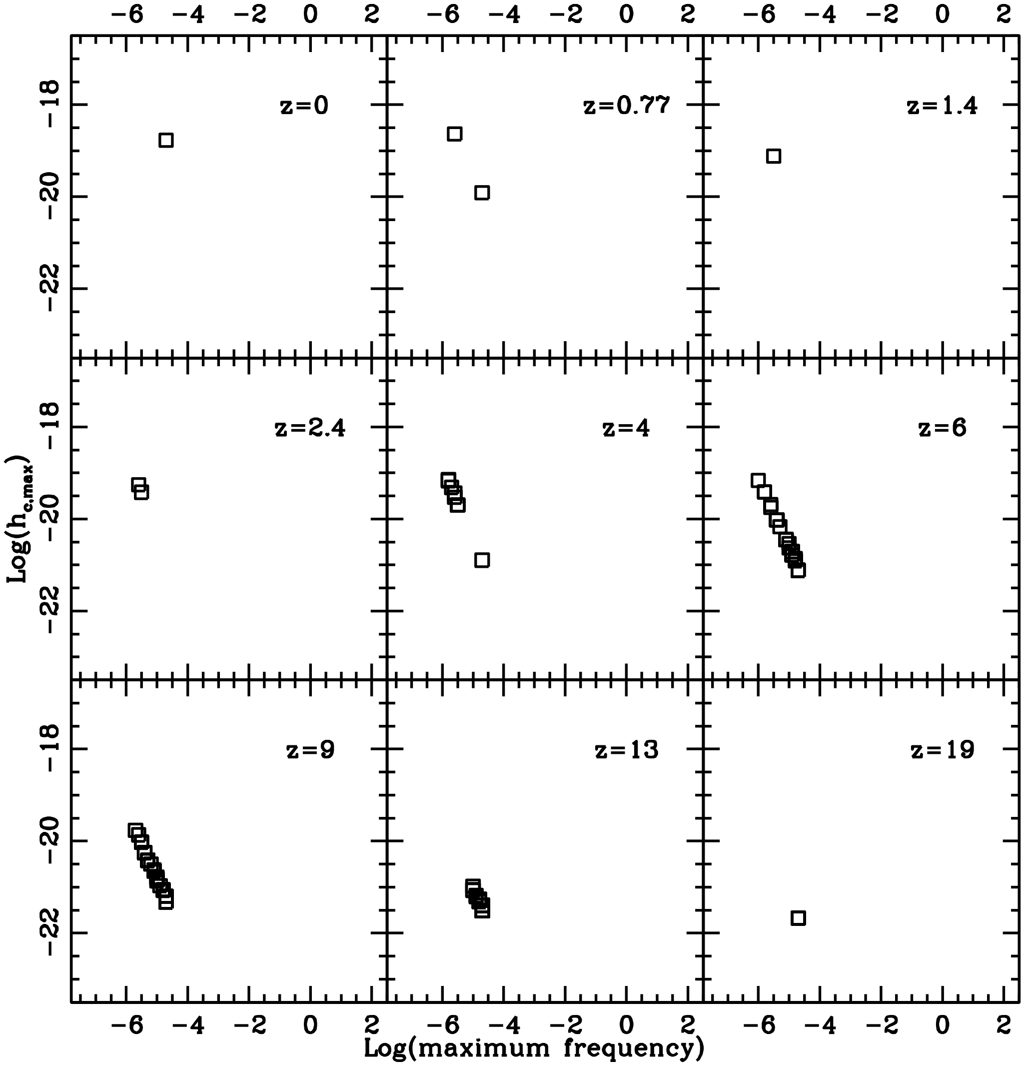

Fig. 4.5 The maximum characteristic strain for all mergers in our simulation at various redshifts as a function of frequency. We show the case of dry growth of SMBH.

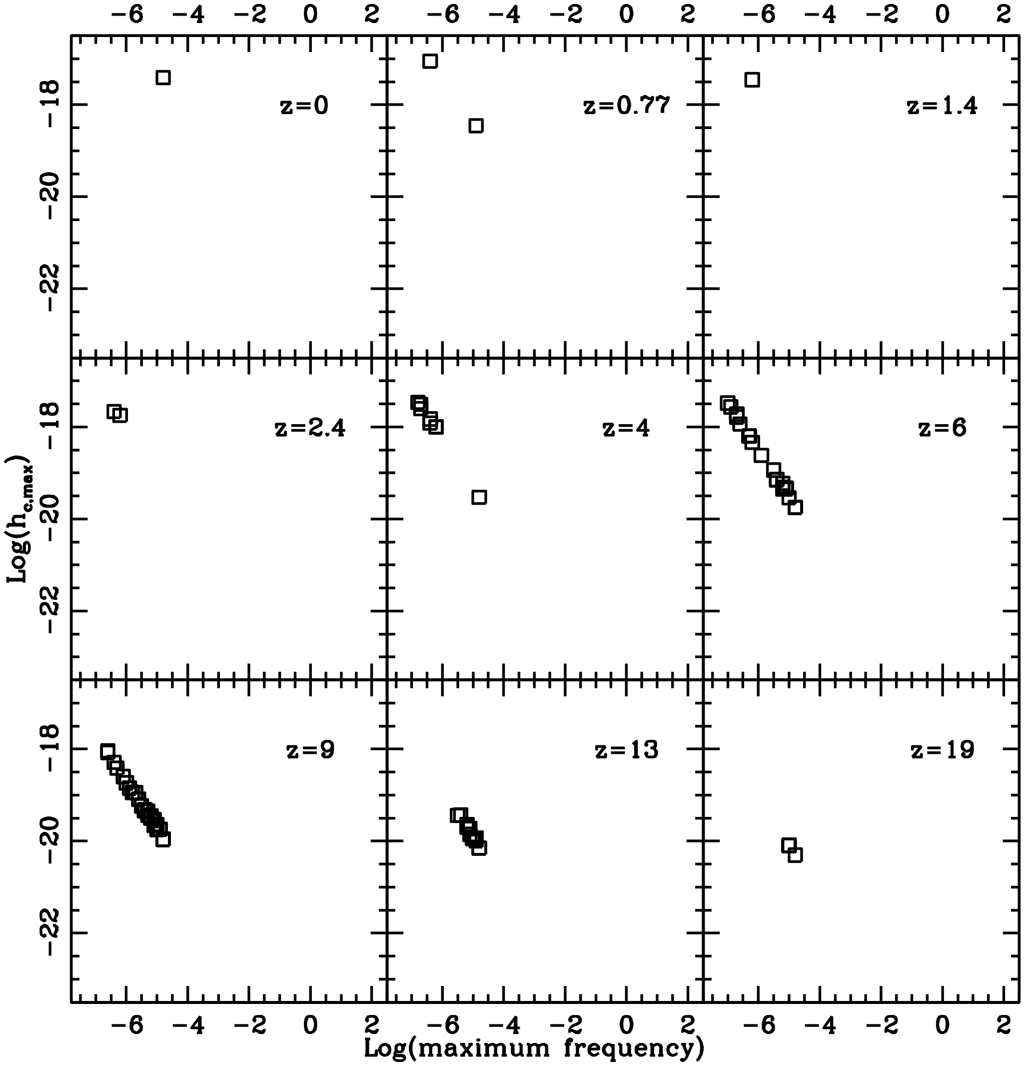

Fig. 4.6 The maximum characteristic strain for all mergers in our simulation at various redshifts as a function of frequency. We show the case of 10:1 growth of SMBH.

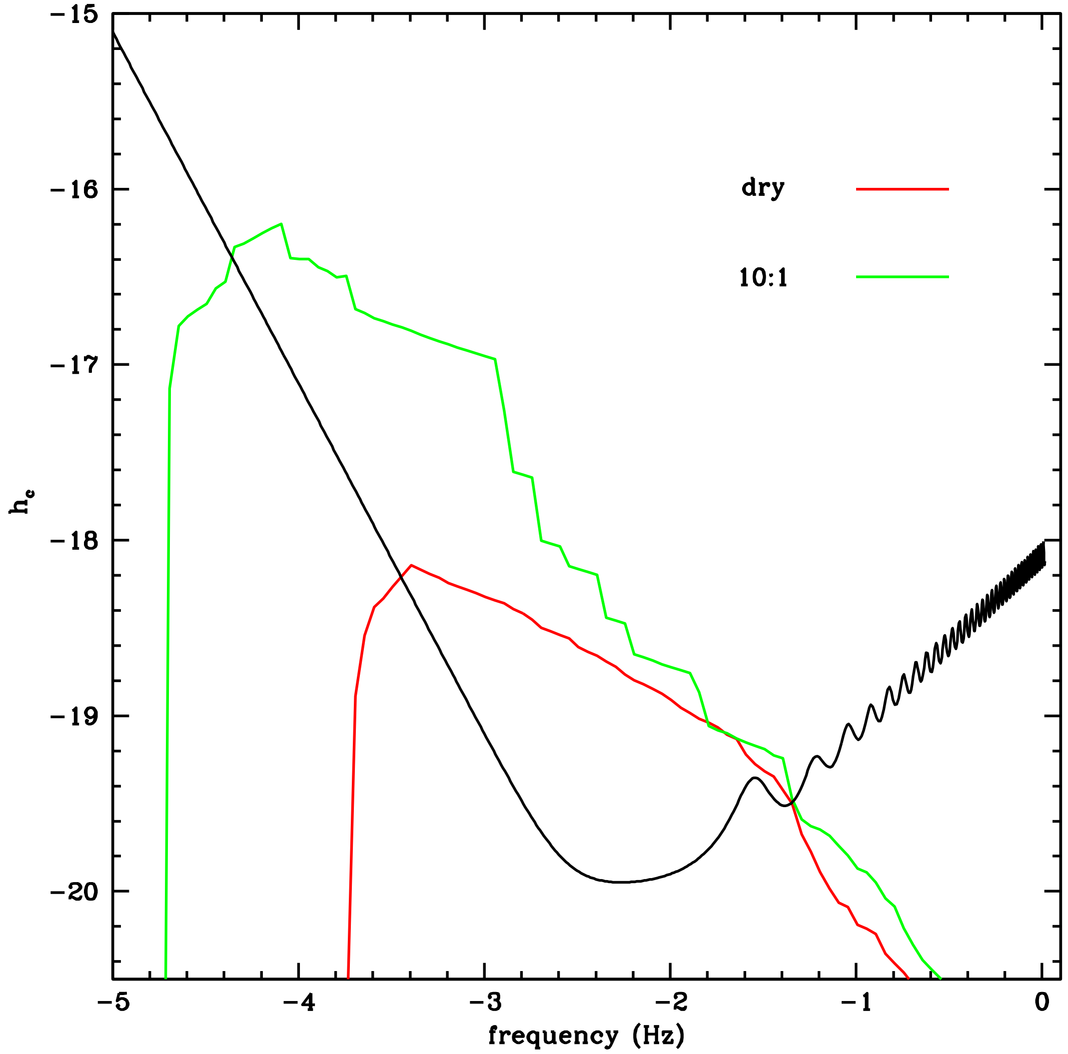

Fig. 4.7 Total characteristic strain as a function of frequency. The characteristic strain is integrated for all redshifts. The case of dry growth is in green and the 10:1 growth is in red. The LISA sensitivity curve in black. The signal in both cases will be observable by LISA.

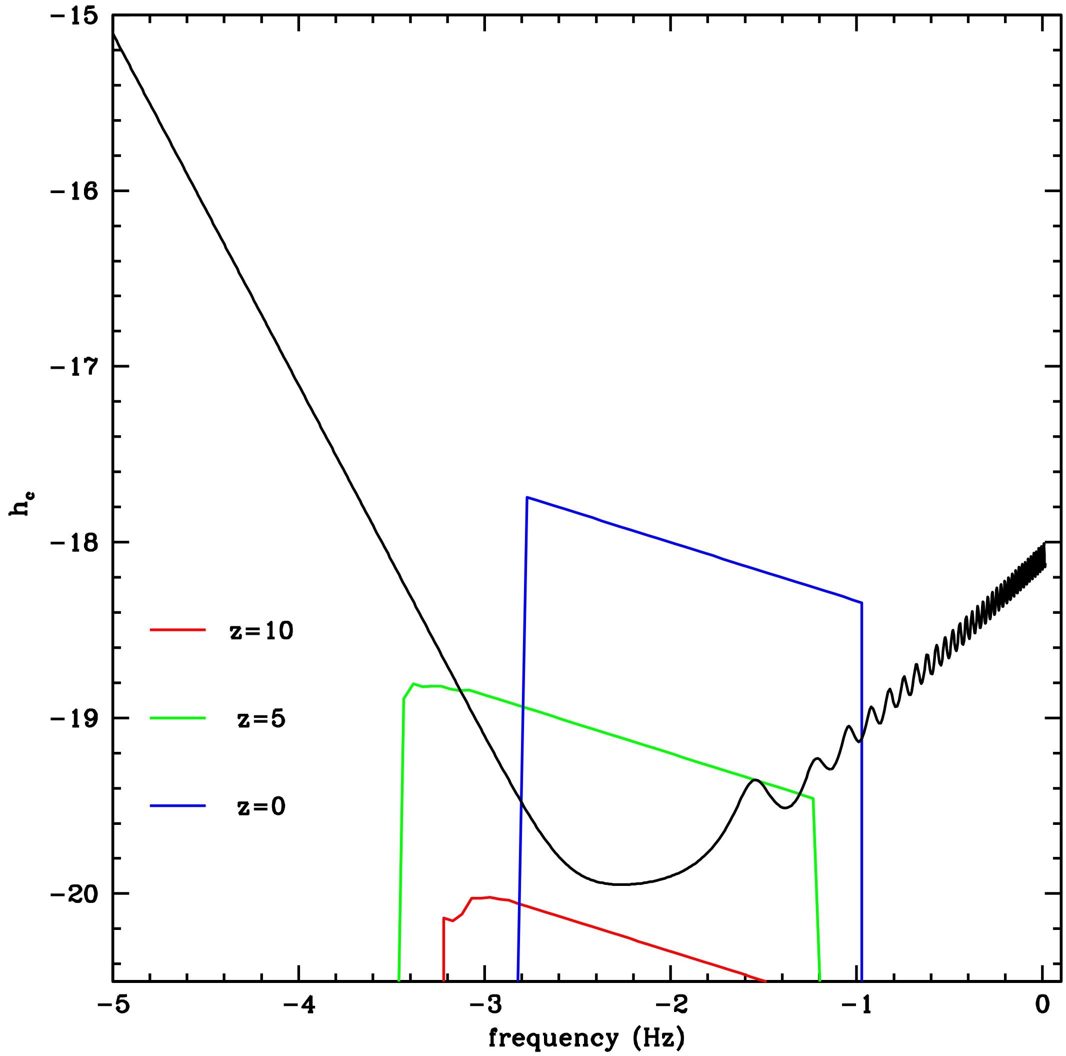

Fig. 4.8 Total characteristic strain as a function of frequency for various redshifts. For the case of dry growth. Mergers of black holes at redshifts z=5 and z=0 will be observable by LISA.

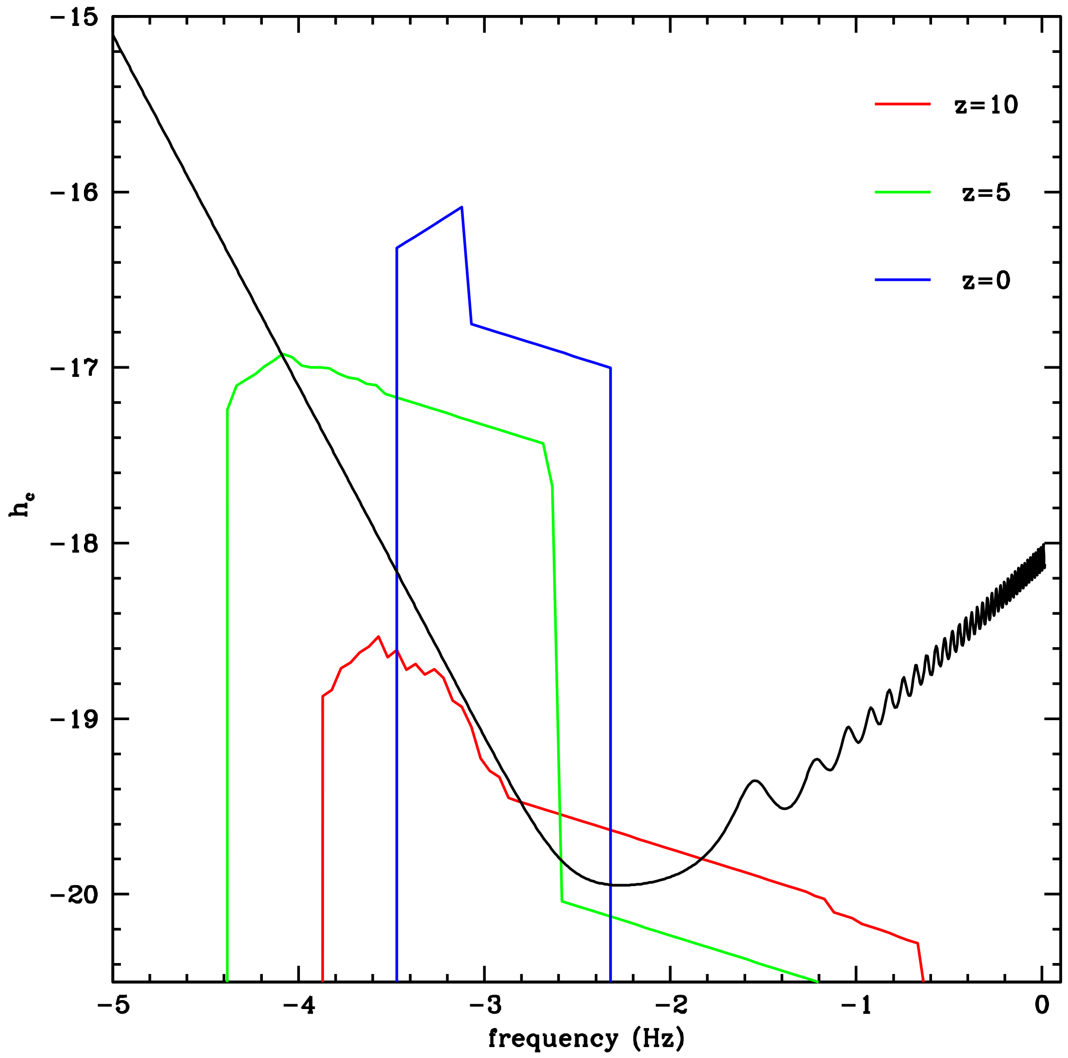

Fig. 4.9 The total characteristic strain as a function of frequency for various redshifts. For the case of 10:1 growth. Mergers of black holes at redshifts z=5 and z=0 will be observable by LISA.

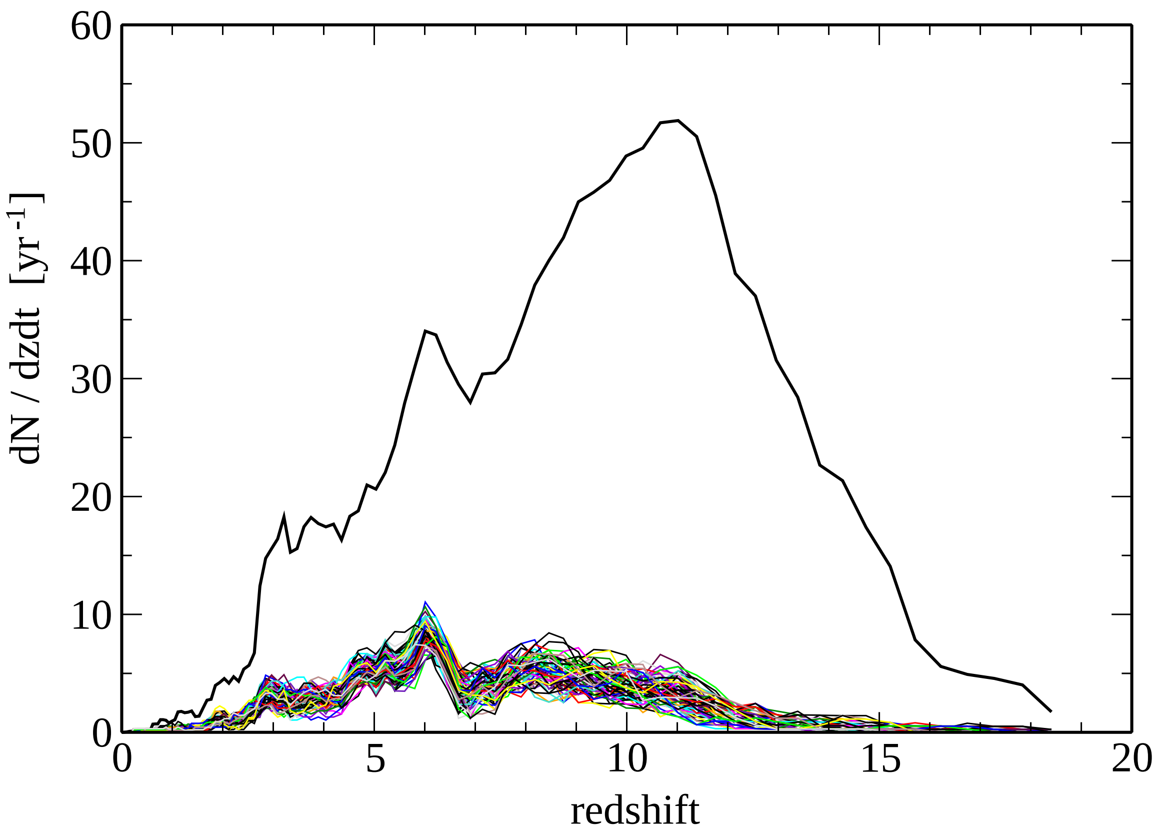

Fig. 4.10 Massive black hole merger rates as a function of redshift in black. Overploted 100 realizations of merger trees for the suppression by seed black hole with an efficiency factor of 0.1.

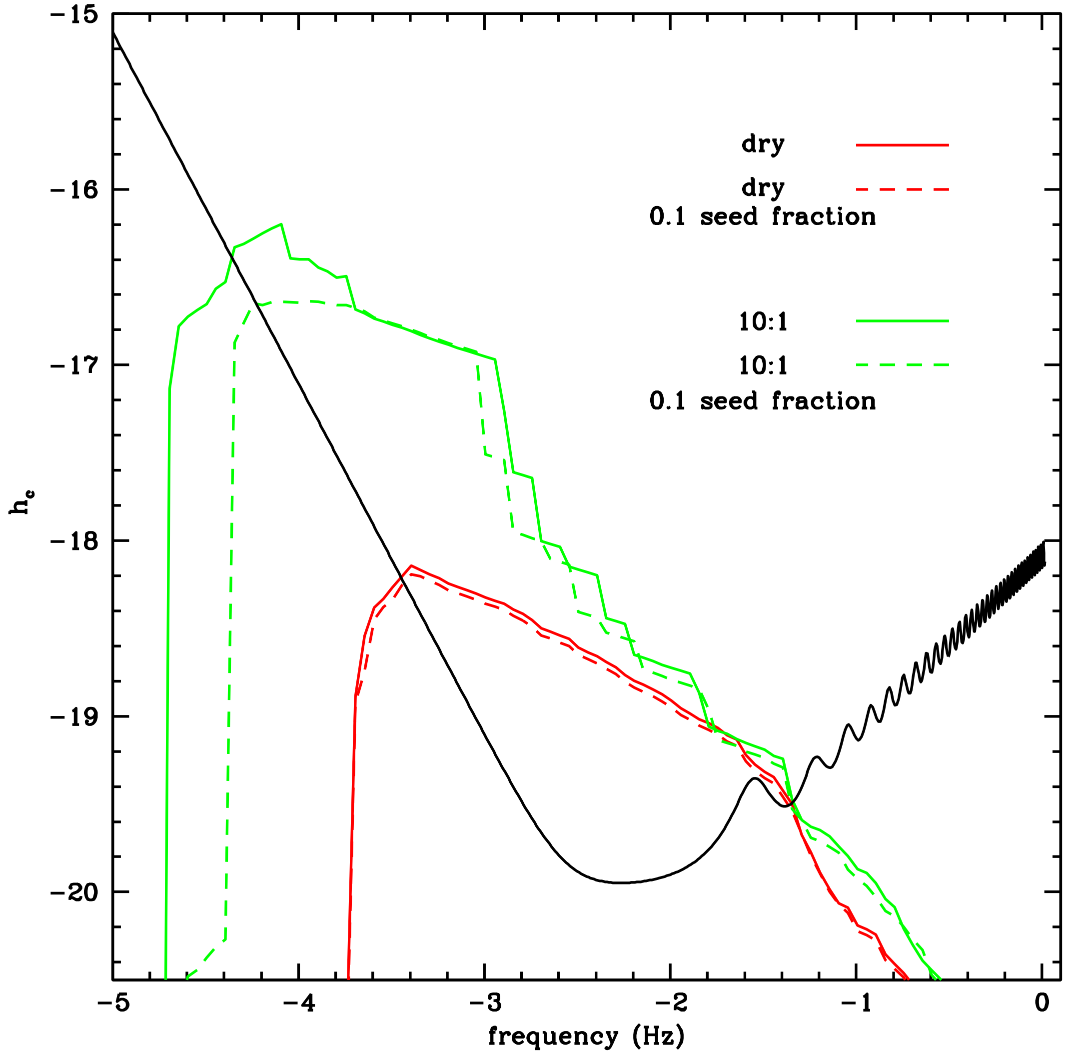

Fig. 4.11 Total characteristic strain for the dry and 10:1 model with the included effect of suppression by the seed formation efficiency.

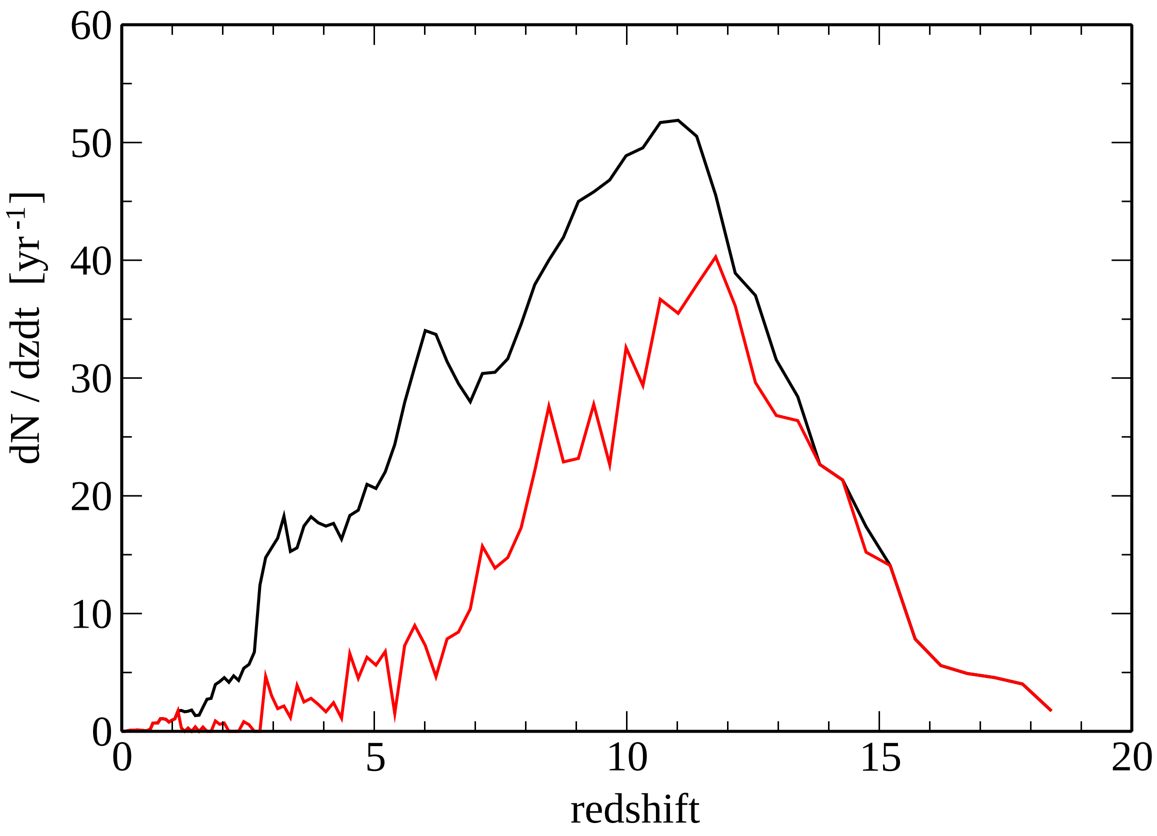

Fig. 4.12 Massive black hole merger rates as a function of redshift in black. Overploted is the merger rate suppression by dynamical friction (in red).

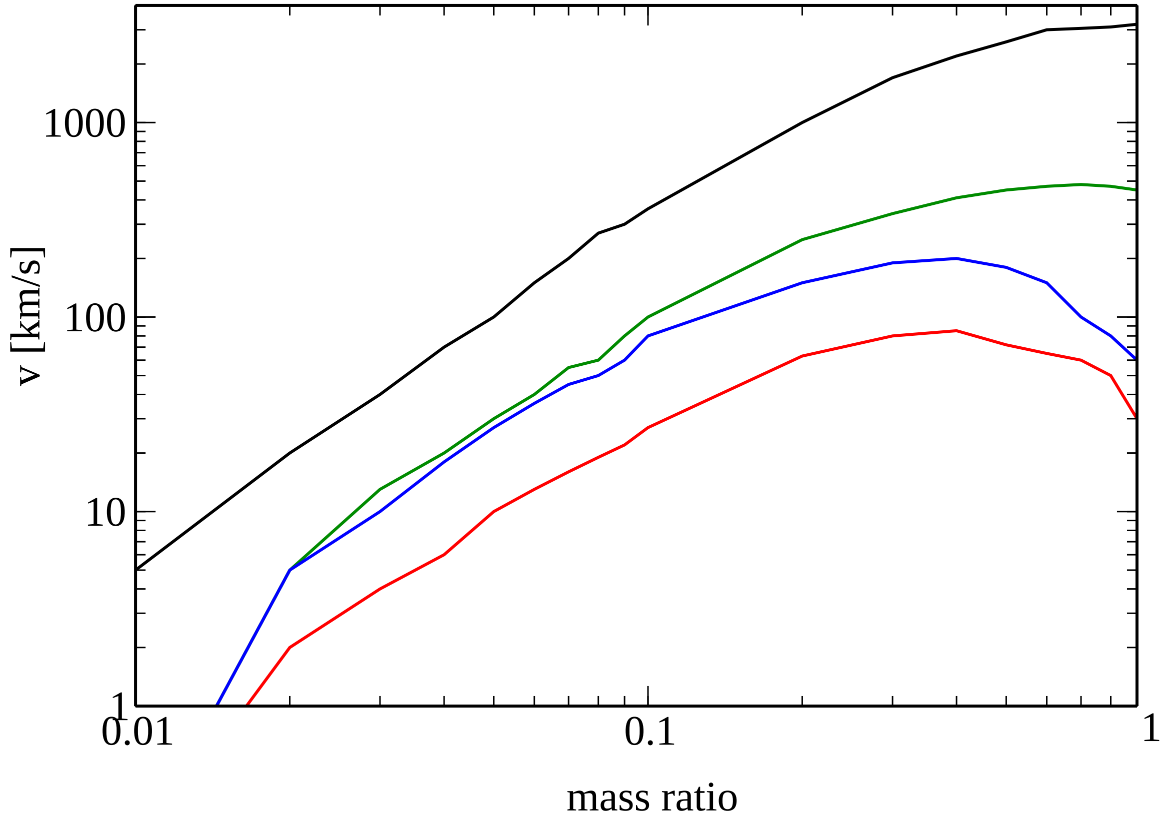

Fig. 4.13 Kicks from Baker et al. (2006, 2007) and Campanelli et al. (2007b). K1 in red is the case of nonspinning black holes with aligned spin axes; K2 in green is nonspinning black holes with anti-aligned spin axes; K3 in blue is case of spinning black holes with optimal orbital configuration; and K4 in black is spinning black holes in the orbital configuration that provides largest kick values (fast spinning black holes, where spin vectors have opposite directions and are in the orbital plane).

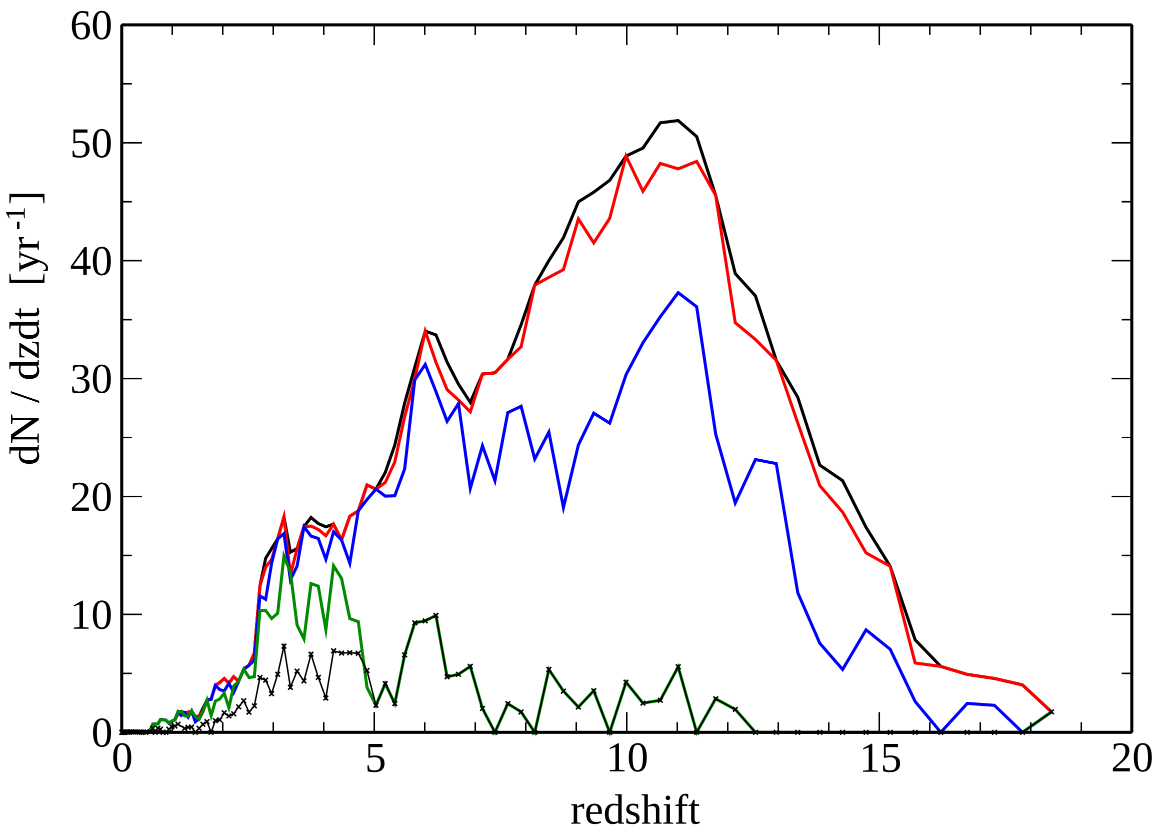

Fig. 4.14 Massive black hole merger rates as a function of redshift in black. Merger rates after gravitational recoils we plotted for K1 in red; K2 in green; K3 in blue; and K4 in thin black.

Chapter 5

Summary

We have performed and analyzed high-resolution collisionless simulations of the evolution of structures in a ΛCDM model. First we studied the effects of gravitational recoil in the broad cosmological context of black hole trajectories and spatial distributions depending on the gravitational potential of dark matter structures in our simulations. For both ranges of kicks (first centered at 75 $\mathrm{km\,s^{-1}}$ and second at 200 $\mathrm{km\,s^{-1}}$) we assume IMBHs are ejected from their host halos in many cases. However, we show that the ejected black holes sink either back toward the center of their host halo or toward the center of the primary halo as the primary dominates the dynamics of its local group. Although almost all of the black holes reach the primary, only a small fraction of them merge at the center in less than a Hubble time, thus reducing the merger rate from R $\sim$ 100 $\mathrm{yr^{-1}}$ to R $\sim$ 4-5 $\mathrm{yr^{-1}}$ for the first range of kicks and to no mergers at all in the second range.

We have followed in detail the formation of dark matter halos and tracked their evolution through a study of their merger tree. The merger tree we made is the first cosmological ($0 \lesssim z \lesssim 20$) N-body merger tree that covers the large dynamical range of structure evolution, $10^7\ \mathrm{M_\odot} \lesssim \mathrm{M_{halo}} \lesssim 10^{13}\ \mathrm{M_\odot}$. From the merger tree we obtain a maximum merger rate of $\sim 55\ \mathrm{yr^{-1}}$. Our original focus was on trajectories of intermediate mass black holes formed in mini-halos at redshifts of 10-20, as they fall into nearby large protogalactic halos. These massive black holes could make an important contribution to the SMBH assembly. We show that the SMBH forms through a combination of mergers of massive black holes and periodic gas accretion. Mergers account for $\sim$ 10% of the final SMBH mass and gas accretion for $\sim$ 90%. A SMBH completes its growth at $z \sim 6$ in both gas accretion growth scenarios reaching the final mass of $\sim 2 \times 10^6\ \mathrm{M_\odot}$ in the dry model (growth through mergers only) and $\sim 3 \times 10^7\ \mathrm{M_\odot}$ in the 10:1 model (growth through mergers combined with accretion). We also identify a population of high redshift ULX sources corresponding to dwarf galaxies which have been tidally stripped by larger galaxy, and we predict $\sim$5-10 ULX sources per galaxy at $z\sim3$. These sources will be observable by planned future X-ray satellites, such as Generation-X.

Once the black hole merger tree is in place, we proceed with calculating the gravitational wave signal from black hole mergers. We predict a characteristic strain in the range $\sim 10^{-18} \lesssim \mathrm{h_c} \lesssim \sim 10^{-16}$, constrained by the dry model at the lower end and the 10:1 model at the higher value of $\mathrm{h_c}$. In this manner, LISA will be able to distinguish between different growth scenarios. We also show that SMBH evolution might be suppressed by various processes, from the efficiency of dynamical friction to the gravitational recoil after black hole mergers. When combined, these suppression mechanisms reduce the merger rates to R $\sim$ 1-10 $\mathrm{yr^{-1}}$ at redshifts $z \gtrsim 2$ and R $\sim$ 0.1-1 $\mathrm{yr^{-1}}$ at $z \lesssim 2$.

Although many black holes sink to the inner kiloparsec of large dark matter halos, current simulations have inadequate resolution to follow the trajectories to smaller radii. For that reason, our numerical approach to the problem stops at the moment two or more dark matter halos merge, and it is continued through the analytical treatment of suppression processes performed after the simulation run through the analysis of the output files. If the black hole tracer particles could be resolved so that they properly account for the dynamics of seed black holes, than the numerical dynamical friction would mimic "real" dynamical friction with reasonable fidelity, and there would be no need for dark matter halos merger trees. By increasing the number of particles, we increase mass and spatial resolution, and we can follow the black hole dynamics properly all the way to the final parsec before merger. In order for dynamical friction to work accurately in numerical simulations, the density of the background (in this case, the primary halo density) needs to be well resolved. Higher resolution gives smaller softening lengths for particles and smaller softening lengths give more realistic dynamical friction.

5.0.1 Simulation with Proper Dynamical Friction

In order to properly treat dynamics of massive black holes, we have been awarded 125000 CPU hours at the Columbia High-End Computing Program. The purpose of this project is to study how stellar to massive black holes interact within a cosmological environment. One of the most exciting advances in computational physics recently has been to simulate the coalescence, merger, and ringdown of two black holes in general relativity. These simulations have shown that when the black holes are spinning, have unequal masses, or are on eccentric orbits, the final black hole receives a kick as fast as 4000 km/s (typical kick velocities are $\sim$ 200 km/s). When black holes have such high kick velocities, they can evacuate dark matter halos at high redshift. Since a typical dark matter halo undergoes many mergers throughout its lifetime, it is now unclear how galaxies retain their supermassive black holes in the face of this repeated onslaught of gravitational wave kicks.

We are running an extremely high resolution N-body simulation of a small cosmological volume to study the dynamics of black hole mergers from seeds to supermassive black holes. We are incorporating the black hole coalescence and the resultant kick velocity "on the fly" within the simulation so that the black hole merger product can thereafter interact self-consistently within the cosmological volume. To achieve this, we simulate a volume about the same mass and size as the Milky Way halo (10 kpc on a side) from redshift 49 to 0 with $\sim$ 28 million particles so that the spatial softening length is on the order of a parsec. To achieve this resolution, we simulate the volume in steps: the first pass identifies the high density regions, and the second (and subsequent) passes zoom in on high density regions by resimulating the volume from a higher redshift –this time including many cloned particles within the high density region. Once our pre-identified black hole particles are within a softening length, we merge the two particles into a more massive single particle, and we apply a kick velocity to this particle selected from a probability distribution function for kick velocity as a function of the merger dynamics and orientation. As we follow the growing black holes within a still collapsing and dynamic volume, we will be also be able to determine the mean distribution of "rogue" black holes in a Milky Way-sized halo.

We are exploring both massive black hole mergers (when the mass ratio between the two black holes is close to one) and extreme mass ratio interactions, or EMRIs (when the mass ratio between the two black holes is very large). Both of these are the primary classes of gravitational wave sources expected for LISA. Most current estimates of the event rate for black hole mergers have either neglected the effect of gravitational wave kicks entirely, or have used typical kick velocities that are much slower than have been demonstrated through proper general relativistic simulations. By including the effect of gravitational wave kicks self consistently within the simulation, we can make much more accurate LISA event rate estimates.

5.0.2 Simulation with Isolated Halos

We have also been awarded with 90,000 CPU hours to run two additional simulations. One has the purpose of confirming the results we have presented in the previous chapters since they are based on a single set of initial conditions. The re-simulation with different random initial conditions is necessary to account for cosmic variance. It also uses WMAP2 results for creation of initial conditions, and we are running it with GADGET-2.

The second simulation is designed to look for "isolated halos". Dark matter halos usually go through a violent merger history as we have showed in the derived merger rates. Large halos ($\sim 10^{12}$ $M_{\odot}$) experience ~ 10 major mergers and up to ~ 1000 minor mergers. However, it is possible that some of the dark matter halos manage to stay isolated throughout the Hubble time, merging less then 100 times. Since the largest halos dominate the dynamics of the system, their gravitational pull creates large voids between them. Inside these voids, isolated halos could grow in size mostly by accreting surrounding dark matter and occasionally merging with other halos. These halos would be able to grow to $\sim 10^{11}$ $M_{\odot}$ but the small number of mergers would leave them without a supermassive black hole at the center. We have found several isolated halos in the low density regions of our simulation box. Fig. 5.1 shows the mass of the SMBH at the center of primary halo as a function of primary mass through out all redshifts. Overplotted are same functions for isolated halos we find in voids. Their masses range from $\sim 4\times10^{9}$ $M_{\odot}$ to $\sim 7\times10^{11}$ $M_{\odot}$ but the corresponding black holes at their centers have less then 3000 $M_{\odot}$. There are examples of objects in this mass range with low mass or no central black hole (globular cluster G1, Sd galaxies, NGC 4395, M33). Since we had focused the high resolution refinement field on high density regions, we have left these voids unresolved. With the next simulation we are doing exactly the opposite. High density regions will be left unresolved while refinement field will be implemented for voids.

5.0.3 Simulation with Downsizing

Perhaps the fact that isolated halos have black holes in the IMBH range is the result of our assumptions about black hole growth. For black hole growth we are using a combination of black hole mergers and periods of gas accretion approximated by Salpeter timescale. With smooth and continues gas accretion, black holes inside isolated halos could also grow to the SMBH range. Recent observation show that the number density of low mass AGNs peaks at $z < 1$ (Cowie et al. 2003; Merloni 2004; Heckman et al. 2004). This effect is called "downsizing" because it suggests that the number density of lower mass AGNs does not peak at redshifts higher than z=3 as previously thought in the classic picture of the quasars luminosity function.

In our small volume simulation, we are plagued by small number statistics, and can not derive the AGN number density. In fact, if we were to scale our simulation up in mass, so that the most massive SMBHs were $O(10^{10})$ $\mathrm{M}_\odot$, the low mass black holes in isolated halos would gain most of their mass at late redshifts compared to the most massive SMBH. A much larger simulation box is necessary to obtain number density of AGNs in range 10^6 $\mathrm{M}_\odot \lesssim \mathrm{M}_{\mathrm{AGN}} \lesssim 10^{10}$ $\mathrm{M}_\odot$.

We will run a large N-body cosmological simulation with $\gtrsim 10^8$ particles in a planned collaboration with prof. David Merritt at Rochester Institute of Technology (RIT). This simulation is designed to test a large cosmological volume ($\sim$ 100 Mpc) and broad dynamical range (100 $\mathrm{M}_\odot \lesssim \mathrm{M} \lesssim 10^{13}$ $\mathrm{M}_\odot$) for evidence of "downsizing" in a build-up of SMBH. We will reproduce the AGN luminosity function for a range of SMBH masses (10^6 $\mathrm{M}_\odot \lesssim \mathrm{M}_{\mathrm{SMBH}} \lesssim 10^8$ $\mathrm{M}_\odot$) and study its behavior at various redshifts. We will run the simulation at the 32-node GRAPE cluster at the RIT. This cluster is the largest facility of its kind anywhere in the world and will provide us with up to hundred times faster simulation runs than previously.

5.0.4 Modeling X-Ray Radiation

With previously described simulations we hope to achieve the proper treatment of massive black hole dynamics through introduction of highly resolved particles that can merge and "feel" dynamical friction in the properly resolved dark matter background density. With this it will be possible to track black holes in any mass range as they sink toward the inner parsecs at the centers of galaxies. In this manner, once the gas is included, we will be able to model both the X-ray radiation from the cosmological population of massive X-ray binaries inside the broad redshift range, and the X-ray radiation from ULX sources interpreted as off-centered IMBHs.

These events are of enormous astrophysical interest as their electromagnetic counterparts are observable in the X-ray and their presence may linger well into the late Universe. Therefore, our work on merger rates and gravitational wave radiation will be followed by modeling of X-ray radiation produced from successive, hierarchical binary black hole mergers.

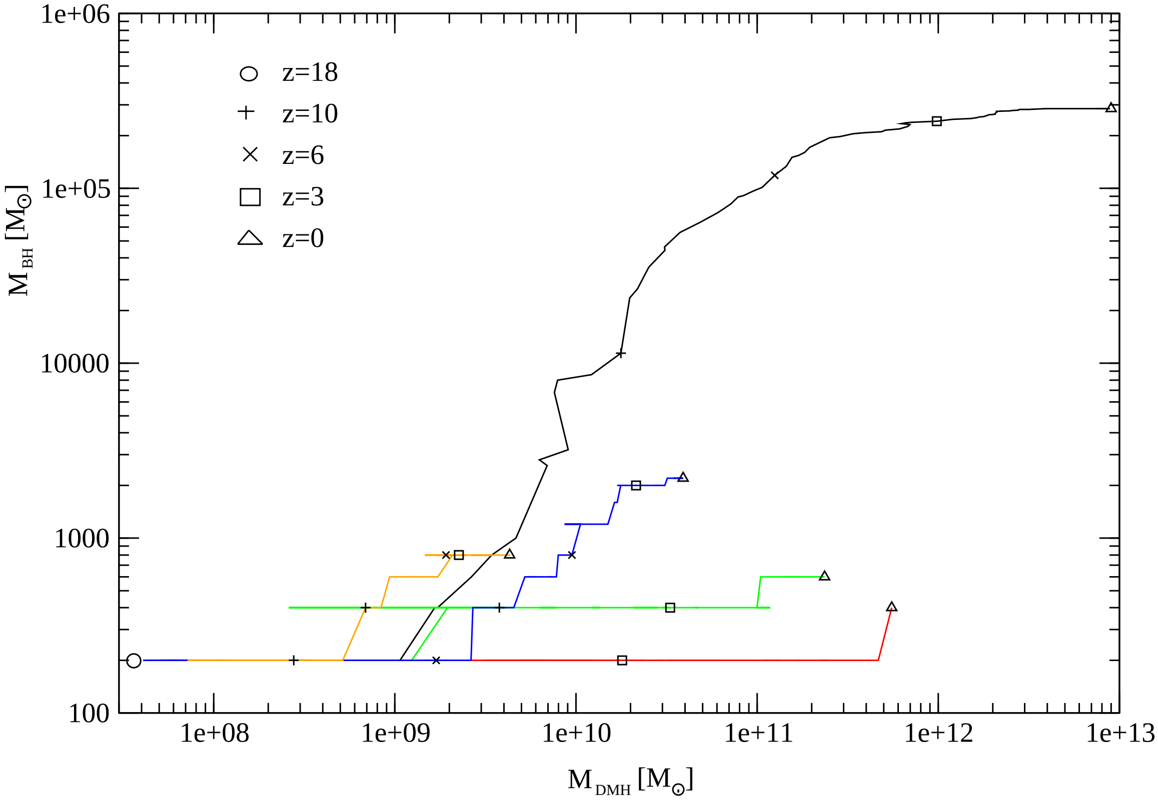

Fig. 5.1 Evolution of SMBH and its host dark matter halo. The primary SMBH and the primary halo are in black. Overplotted are isolated halos as candidates for galaxies with or without an IMBH at the center.

Bibliography

Aarseth, S. 2005, astro-ph/0511565

Aarseth, S. J., Turner, E. L., & Gott, III, J. R. 1979, ApJ, 228, 664

Abel, T., Anninos, P., Norman, M. L., & Zhang, Y. 1998, ApJ, 508, 518

Abel, T., Anninos, P., Zhang, Y., & Norman, M. L. 1997, New Astronomy, 2, 181

Abel, T., Bryan, G. L., & Norman, M. L. 2000, ApJ, 540, 39

—. 2002, Science, 295, 93

Agol, E. & Kamionkowski, M. 2002, MNRAS, 334, 553

Agol, E., Kamionkowski, M., Koopmans, L. V. E., & Blandford, R. D. 2002, ApJ, 576, L131

Aller, M. C. & Richstone, D. 2002, AJ, 124, 3035

Araújo, H., Boatella, C., Chmeissani, M., Conchillo, A., García-Berro, E., Grimani, C., Hajdas, W., Lobo, A., Martínez, L., Nofrarias, M., Ortega, J. A., Puigdengoles, C., Ramos-Castro, J., Sanjuán, J., Wass, P., & Xirgu, X. 2007, Journal of Physics Conference Series, 66, 2003

Armitage, P. J. & Natarajan, P. 2002, ApJ, 567, L9

Audit, E., Teyssier, R., & Alimi, J.-M. 1998, A&A, 333, 779

Baker, J. G., Boggs, W. D., Centrella, J., Kelly, B. J., McWilliams, S. T., Miller, M. C., & van Meter, J. R. 2007, astro-ph/0702390

Baker, J. G., Centrella, J., Choi, D.-I., Koppitz, M., van Meter, J. R., & Miller, M. C. 2006, ApJ, 653, L93

Bardeen, J. M., Bond, J. R., Kaiser, N., & Szalay, A. S. 1986, ApJ, 304, 15

Barnes, J. & Hut, P. 1986, Nature, 324, 446

Begelman, M. C., Blandford, R. D., & Rees, M. J. 1980, Nature, 287, 307

Bender, R., Kormendy, J., Bower, G., Green, R., Thomas, J., Danks, A. C., Gull, T., Hutchings, J. B., Joseph, C. L., Kaiser, M. E., Lauer, T. R., Nelson, C. H., Richstone, D., Weistrop, D., & Woodgate, B. 2005, ApJ, 631, 280

Bennett, C. L., Halpern, M., Hinshaw, G., Jarosik, N., Kogut, A., Limon, M., Meyer, S. S., Page, L., Spergel, D. N., Tucker, G. S., Wollack, E., Wright, E. L., Barnes, C., Greason, M. R., Hill, R. S., Komatsu, E., Nolta, M. R., Odegard, N., Peiris, H. V., Verde, L., & Weiland, J. L. 2003, ApJS, 148, 1

Berczik, P., Merritt, D., Spurzem, R., & Bischof, H.-P. 2006, ApJ, 642, L21

Bertschinger, E. & Gelb, J. M. 1991, Computers in Physics, 5, 164

Binney, J. & Tremaine, S. 1987, Galactic dynamics (Princeton, NJ, Princeton University Press, 1987, 747 p.)

Blanchet, L. 1996, Phys. Rev. D, 54, 1417

—. 2003, astro-ph/0304014

Blanchet, L., Qusailah, M. S. S., & Will, C. M. 2005, ApJ, 635, 508

Bode, P., Ostriker, J. P., & Xu, G. 2000, ApJS, 128, 561

Bogdanović, T., Reynolds, C. S., & Miller, M. C. 2007, ApJ, 661, L147

Bond, J. R., Arnett, W. D., & Carr, B. J. 1984, ApJ, 280, 825

Bower, R. G. 1991, MNRAS, 248, 332

Bromm, V., Coppi, P. S., & Larson, R. B. 1999, ApJ, 527, L5

—. 2002, ApJ, 564, 23

Bromm, V., Ferrara, A., Coppi, P. S., & Larson, R. B. 2001a, MNRAS, 328, 969

Bromm, V., Kudritzki, R. P., & Loeb, A. 2001b, ApJ, 552, 464

Bromm, V. & Loeb, A. 2003, ApJ, 596, 34

—. 2004, New Astronomy, 9, 353

Buyle, P., Baes, M., & Dejonghe, H. 2004, in IAU Symposium, Vol. 220, Dark Matter in Galaxies, ed. S. Ryder, D. Pisano, M. Walker, & K. Freeman, 317–+

Campanelli, M., Lousto, C., Zlochower, Y., & Merritt, D. 2007a, ApJ, 659, L5

Campanelli, M., Lousto, C. O., Zlochower, Y., & Merritt, D. 2007b, astro-ph/0702133

Chandrasekhar, S. 1984, S&T, 67, 428

Chandrasekhar, S. & Detweiler, S. 1975, Royal Society of London Proceedings Series A, 344, 441

Ciardi, B. & Ferrara, A. 2005, Space Science Reviews, 116, 625

Colbert, E. J. M. & Ptak, A. F. 2002, ApJS, 143, 25

Colpi, M., Mayer, L., & Governato, F. 1999, ApJ, 525, 720

Cornish, N. J. & Levin, J. 2002, astro-ph/0207016

Couchman, H. M. P. 1991, ApJ, 368, L23

Couchman, H. M. P. & Rees, M. J. 1986, MNRAS, 221, 53

Cowie, L. L., Barger, A. J., Bautz, M. W., Brandt, W. N., & Garmire, G. P. 2003, ApJ, 584, L57

Crowder, J. & Cornish, N. J. 2005, Phys. Rev. D, 72, 083005

Damour, T. & Gopakumar, A. 2006, Phys. Rev. D, 73, 124006

Danzmann, K. 2003, Advances in Space Research, 32, 1233

Davis, M., Efstathiou, G., Frenk, C. S., & White, S. D. M. 1985, ApJ, 292, 371

de Blok, W. J. G. & McGaugh, S. S. 1997, MNRAS, 290, 533

de Zeeuw, T. 1985, MNRAS, 216, 273

Dehnen, W., McLaughlin, D. E., & Sachania, J. 2006, MNRAS, 369, 1688

Dekel, A. & Rees, M. J. 1987, Nature, 326, 455

Efstathiou, G., Davis, M., White, S. D. M., & Frenk, C. S. 1985, ApJS, 57, 241

Eisenstein, D. J. & Hut, P. 1998, ApJ, 498, 137

Eisenstein, D. J. & Loeb, A. 1995, ApJ, 439, 520

El-Zant, A., Shlosman, I., & Hoffman, Y. 2001, ApJ, 560, 636

Erickcek, A. L., Kamionkowski, M., & Benson, A. J. 2006, MNRAS, 371, 1992

Escala, A., Larson, R. B., Coppi, P. S., & Mardones, D. 2005, ApJ, 630, 152

Fabbiano, G. 1989, ARA&A, 27, 87

Fabbiano, G. & White, N. E. Compact stellar X-ray sources in normal galaxies (Compact stellar X-ray sources), 475–506

Fan, X., Strauss, M. A., Schneider, D. P., Becker, R. H., White, R. L., Haiman, Z., Gregg, M., Pentericci, L., Grebel, E. K., Narayanan, V. K., Loh, Y.-S., Richards, G. T., Gunn, J. E., Lupton, R. H., Knapp, G. R., Ivezić, Ž., Brandt, W. N., Collinge, M., Hao, L., Harbeck, D., Prada, F., Schaye, J., Strateva, I., Zakamska, N., Anderson, S., Brinkmann, J., Bahcall, N. A., Lamb, D. Q., Okamura, S., Szalay, A., & York, D. G. 2003, AJ, 125, 1649

Favata, M., Hughes, S. A., & Holz, D. E. 2004, ApJ, 607, L5

Ferrarese, L. 2002, ApJ, 578, 90

Ferrarese, L. & Ford, H. 2005, Space Science Reviews, 116, 523

Ferrarese, L. & Merritt, D. 2000, ApJ, 539, L9

Filippenko, A. V. & Ho, L. C. 2003, ApJ, 588, L13

Fitchett, M. J. 1983, MNRAS, 203, 1049

Fitchett, M. J. & Detweiler, S. 1984, MNRAS, 211, 933

Flores, R. A. & Primack, J. R. 1994, ApJ, 427, L1

Foschini, L., Di Cocco, G., Ho, L. C., Bassani, L., Cappi, M., Dadina, M., Gianotti, F., Malaguti, G., Panessa, F., Piconcelli, E., Stephen, J. B., & Trifoglio, M. 2002, A&A, 392, 817

Freitag, M., Gürkan, M. A., & Rasio, F. A. 2006, MNRAS, 368, 141

Fryer, C. L. 1999, ApJ, 522, 413

Fryer, C. L., Holz, D. E., & Hughes, S. A. 2002, ApJ, 565, 430

Fryer, C. L., Woosley, S. E., & Heger, A. 2001, ApJ, 550, 372

Fukushige, T., Makino, J., & Kawai, A. 2005, PASJ, 57, 1009

Galli, D. & Palla, F. 1998, A&A, 335, 403

Gao, L., White, S. D. M., Jenkins, A., Frenk, C. S., & Springel, V. 2005, MNRAS, 363, 379

Gebhardt, K., Bender, R., Bower, G., Dressler, A., Faber, S. M., Filippenko, A. V., Green, R., Grillmair, C., Ho, L. C., Kormendy, J., Lauer, T. R., Magorrian, J., Pinkney, J., Richstone, D., & Tremaine, S. 2001a, ApJ, 555, L75

Gebhardt, K., Kormendy, J., Ho, L. C., Bender, R., Bower, G., Dressler, A., Faber, S. M., Filippenko, A. V., Green, R., Grillmair, C., Lauer, T. R., Magorrian, J., Pinkney, J., Richstone, D., & Tremaine, S. 2000, ApJ, 543, L5

Gebhardt, K., Lauer, T. R., Kormendy, J., Pinkney, J., Bower, G. A., Green, R., Gull, T., Hutchings, J. B., Kaiser, M. E., Nelson, C. H., Richstone, D., & Weistrop, D. 2001b, AJ, 122, 2469

Gebhardt, K., Rich, R. M., & Ho, L. C. 2005, ApJ, 634, 1093

Gerhard, O. 2001, ApJ, 546, L39

Ghez, A. M., Duchêne, G., Matthews, K., Hornstein, S. D., Tanner, A., Larkin, J., Morris, M., Becklin, E. E., Salim, S., Kremenek, T., Thompson, D., Soifer, B. T., Neugebauer, G., & McLean, I. 2003, ApJ, 586, L127

Ghez, A. M., Salim, S., Hornstein, S. D., Tanner, A., Lu, J. R., Morris, M., Becklin, E. E., & Duchêne, G. 2005, ApJ, 620, 744

Ghosh, P. & White, N. E. 2001, ApJ, 559, L97

Gingold, R. A. & Monaghan, J. J. 1977, MNRAS, 181, 375

González, J. A., Hannam, M., Sperhake, U., Brügmann, B., & Husa, S. 2007a, Physical Review Letters, 98, 231101

González, J. A., Sperhake, U., Brügmann, B., Hannam, M., & Husa, S. 2007b, Physical Review Letters, 98, 091101

Graham, A. W., Erwin, P., Caon, N., & Trujillo, I. 2001, ApJ, 563, L11

Guainazzi, M., Rodriguez-Pascual, P., Fabian, A. C., Iwasawa, K., & Matt, G. 2004, MNRAS, 355, 297

Gürkan, M. A., Freitag, M., & Rasio, F. A. 2004, ApJ, 604, 632

Guth, A. H. 1981, Phys. Rev. D, 23, 347

Guth, A. H. 2004, in Measuring and Modeling the Universe, ed. W. L. Freedman, 31–+

Haehnelt, M. G. 1994, MNRAS, 269, 199

Haiman, Z., Abel, T., & Rees, M. J. 2000, ApJ, 534, 11

Haiman, Z. & Loeb, A. 2001, ApJ, 552, 459

Haiman, Z., Rees, M. J., & Loeb, A. 1997, ApJ, 476, 458

Haiman, Z., Thoul, A. A., & Loeb, A. 1996, ApJ, 464, 523

Hansen, B. M. S. & Milosavljević, M. 2003, ApJ, 593, L77

Heckman, T. M., Kauffmann, G., Brinchmann, J., Charlot, S., Tremonti, C., & White, S. D. M. 2004, ApJ, 613, 109

Heger, A., Fryer, C. L., Woosley, S. E., Langer, N., & Hartmann, D. H. 2003, ApJ, 591, 288

Heger, A. & Woosley, S. E. 2002, ApJ, 567, 532

Heggie, D. C., Hut, P., Mineshige, S., Makino, J., & Baumgardt, H. 2006, astro-ph/0611950

Herrmann, F., Hinder, I., Shoemaker, D., Laguna, P., & Matzner, R. A. 2007, ApJ, 661, 430

Hockney, R. W. & Eastwood, J. W. 1981, Computer Simulation Using Particles (Computer Simulation Using Particles, New York: McGraw-Hill, 1981)

Hohl, F. 1978, AJ, 83, 768

Hollenbach, D. & McKee, C. F. 1989, ApJ, 342, 306

Holley-Bockelmann, K., Mihos, J. C., Sigurdsson, S., & Hernquist, L. 2001, ApJ, 549, 862

Holley-Bockelmann, K. & Richstone, D. 1999, ApJ, 517, 92

Holley-Bockelmann, K. & Sigurdsson, S. 2006, astro-ph/0601520

Holley-Bockelmann, K., Sigurdsson, S., Ciardullo, R., Feldmeier, J., Mihos, C., & McBride, C. 2005, in Bulletin of the American Astronomical Society, Vol. 37, Bulletin of the American Astronomical Society, 522–+

Hornschemeier, A. E., Brandt, W. N., Alexander, D. M., Bauer, F. E., Garmire, G. P., Schneider, D. P., Bautz, M. W., & Chartas, G. 2002, ApJ, 568, 82

Hu, J., Shen, Y., Lou, Y.-Q., & Zhang, S. 2006, MNRAS, 365, 345

Ibata, R., Chapman, S., Ferguson, A. M. N., Lewis, G., Irwin, M., & Tanvir, N. 2005, ApJ, 634, 287

Islam, R. R., Taylor, J. E., & Silk, J. 2003, MNRAS, 340, 647

Jeans, J. H. 1928, Astronomy and cosmogony (Cambridge [Eng.] The University press, 1928.)

Jernigan, J. G. & Porter, D. H. 1989, ApJS, 71, 871

Kauffmann, G. & Haehnelt, M. 2000, MNRAS, 311, 576

Kazantzidis, S., Mayer, L., Colpi, M., Madau, P., Debattista, V. P., Wadsley, J., Stadel, J., Quinn, T., & Moore, B. 2005, ApJ, 623, L67

Kidder, L. E., Will, C. M., & Wiseman, A. G. 1993, Phys. Rev. D, 47, 3281

King, A. R., Davies, M. B., Ward, M. J., Fabbiano, G., & Elvis, M. 2001, ApJ, 552, L109

Klein, R. I., Fisher, R. T., McKee, C. F., & Truelove, J. K. 1999, in Astrophysics and Space Science Library, Vol. 240, Astrophysics and Space Science Library, ed. S. M. Miyama, K. Tomisaka, & T. Hanawa, 131–+

Komossa, S. 2003, in American Institute of Physics Conference Series, Vol. 686, The Astrophysics of Gravitational Wave Sources, ed. J. M. Centrella, 161–174

Komossa, S., Burwitz, V., Hasinger, G., Predehl, P., Kaastra, J. S., & Ikebe, Y. 2003, ApJ, 582, L15

Kong, A. K. H., Rupen, M. P., Sjouwerman, L. O., & Di Stefano, R. 2005, astro-ph/0503465

Koppitz, M., Pollney, D., Reisswig, C., Rezzolla, L., Thornburg, J., Diener, P., & Schnetter, E. 2007, astro-ph/0701163

Kormendy, J. & Gebhardt, K. 2001, astro-ph/0105230

Kormendy, J. & Richstone, D. 1995, ARA&A, 33, 581

Koushiappas, S. M., Bullock, J. S., & Dekel, A. 2004, MNRAS, 354, 292

Lacey, C. & Cole, S. 1993, MNRAS, 262, 627

—. 1994, MNRAS, 271, 676

Lai, D. & Wiseman, A. G. 1996, Phys. Rev. D, 54, 3958

Laor, A. 2001, ApJ, 553, 677

Lauer, T. R., Faber, S. M., Richstone, D., Gebhardt, K., Tremaine, S., Postman, M., Dressler, A., Aller, M. C., Filippenko, A. V., Green, R., Ho, L. C., Kormendy, J., Magorrian, J., & Pinkney, J. 2007, ApJ, 662, 808

Lehmer, B. D., Brandt, W. N., Hornschemeier, A. E., Alexander, D. M., Bauer, F. E., Koekemoer, A. M., Schneider, D. P., & Steffen, A. T. 2006, AJ, 131, 2394

Lepp, S. & Shull, J. M. 1984, ApJ, 280, 465

Lucy, L. B. 1977, AJ, 82, 1013

Lynden-Bell, D., Faber, S. M., Burstein, D., Davies, R. L., Dressler, A., Terlevich, R. J., & Wegner, G. 1988, ApJ, 326, 19

Macfarland, T., Couchman, H. M. P., Pearce, F. R., & Pichlmeier, J. 1998, New Astronomy, 3, 687

Machacek, M. E., Bryan, G. L., & Abel, T. 2001, ApJ, 548, 509

Mack, K. J., Ostriker, J. P., & Ricotti, M. 2006, astro-ph/0608642

Madau, P., Pozzetti, L., & Dickinson, M. 1998, ApJ, 498, 106

Madau, P. & Rees, M. J. 2001, ApJ, 551, L27

Maggiore, M. 2000, Phys. Rep., 331, 283

Makino, J., Fukushige, T., Koga, M., & Namura, K. 2003, PASJ, 55, 1163

Makino, J. & Taiji, M. 1998, Scientific Simulations with Special-Purpose Computers–the GRAPE Systems (Scientific Simulations with Special-Purpose Computers–the GRAPE Systems, by Junichiro Makino, Makoto Taiji, pp. 248. ISBN 0-471-96946-X. Wiley-VCH , April 1998.)

Martin, P. G., Schwarz, D. H., & Mandy, M. E. 1996, ApJ, 461, 265

Mather, J. C., Cheng, E. S., Cottingham, D. A., Eplee, Jr., R. E., Fixsen, D. J., Hewagama, T., Isaacman, R. B., Jensen, K. A., Meyer, S. S., Noerdlinger, P. D., Read, S. M., Rosen, L. P., Shafer, R. A., Wright, E. L., Bennett, C. L., Boggess, N. W., Hauser, M. G., Kelsall, T., Moseley, Jr., S. H., Silverberg, R. F., Smoot, G. F., Weiss, R., & Wilkinson, D. T. 1994, ApJ, 420, 439

Menou, K., Haiman, Z., & Narayanan, V. K. 2001, ApJ, 558, 535

Merloni, A. 2004, MNRAS, 353, 1035

Merritt, D. 2004, in Coevolution of Black Holes and Galaxies, ed. L. C. Ho, 263–+

Merritt, D. & Ferrarese, L. 2001a, MNRAS, 320, L30

—. 2001b, ApJ, 547, 140

Merritt, D., Milosavljević, M., Favata, M., Hughes, S. A., & Holz, D. E. 2004, ApJ, 607, L9

Merritt, D. & Poon, M. Y. 2004, ApJ, 606, 788

Micic, M., Abel, T., & Sigurdsson, S. 2006, MNRAS, 372, 1540

Micic, M., Holley-Bockelmann, K., Sigurdsson, S., & Abel, T. 2007, astro-ph/0703540

Mihos, J. C. & Hernquist, L. 1994, ApJ, 425, L13

Mii, H. & Totani, T. 2005, ApJ, 628, 873

Milosavljević, M. & Merritt, D. 2003a, ApJ, 596, 860

Milosavljević, M. & Merritt, D. 2003b, in American Institute of Physics Conference Series, Vol. 686, The Astrophysics of Gravitational Wave Sources, ed. J. M. Centrella, 201–210

Miralda-Escudé, J. & Gould, A. 2000, ApJ, 545, 847

Moore, B. 1994, Nature, 370, 629

Nagashima, M., Yahagi, H., Enoki, M., Yoshii, Y., & Gouda, N. 2005, ApJ, 634, 26

Nakamura, F. & Umemura, M. 2001, ApJ, 548, 19

Navarro, J. F., Frenk, C. S., & White, S. D. M. 1997, ApJ, 490, 493

Norman, M. L. & Bryan, G. L. 1999, in Astrophysics and Space Science Library, Vol. 240, Astrophysics and Space Science Library, ed. S. M. Miyama, K. Tomisaka, & T. Hanawa, 19–+

Olive, K. A., Steigman, G., & Walker, T. P. 2000, Phys. Rep., 333, 389

Omukai, K. 2000, ApJ, 534, 809

Omukai, K. & Nishi, R. 1998, ApJ, 508, 141

—. 1999, ApJ, 518, 64

Omukai, K. & Palla, F. 2003, ApJ, 589, 677

Omukai, K. & Yoshii, Y. 2003, ApJ, 599, 746

Ori, A. & Thorne, K. S. 2000, Phys. Rev. D, 62, 124022

O'Shea, B. W. & Norman, M. L. 2007, ApJ, 654, 66

Ostriker, J. P. 2000, Physical Review Letters, 84, 5258

Owen, F. N., Odea, C. P., Inoue, M., & Eilek, J. A. 1985, ApJ, 294, L85

Padmanabhan, T. 1993, Structure Formation in the Universe (Structure Formation in the Universe, by T. Padmanabhan, pp. 499. ISBN 0521424860. Cambridge, UK: Cambridge University Press, June 1993.)

Peebles, P. J. E. 1970, AJ, 75, 13

—. 1972, General Relativity and Gravitation, 3, 63

—. 1980, The large-scale structure of the universe (Research supported by the National Science Foundation. Princeton, N.J., Princeton University Press, 1980. 435 p.)

—. 1993, Principles of physical cosmology (Princeton Series in Physics, Princeton, NJ: Princeton University Press, —c1993)

Porciani, C., Dekel, A., & Hoffman, Y. 2002, MNRAS, 332, 325

Portegies Zwart, S. F., Baumgardt, H., Hut, P., Makino, J., & McMillan, S. L. W. 2004, Nature, 428, 724

Portegies Zwart, S. F., McMillan, S. L. W., & Gerhard, O. 2003, ApJ, 593, 352

Portinari, L., Chiosi, C., & Bressan, A. 1998, A&A, 334, 505

Press, W. H. & Schechter, P. 1974, ApJ, 187, 425

Ptak, A. & Colbert, E. 2004, ApJ, 606, 291

Quinlan, G. D. 1996, New Astronomy, 1, 35

Reed, D. S., Bower, R., Frenk, C. S., Jenkins, A., & Theuns, T. 2007, MNRAS, 374, 2

Rhook, K. J. & Wyithe, J. S. B. 2005, MNRAS, 361, 1145

Riess, A. G., Nugent, P. E., Gilliland, R. L., Schmidt, B. P., Tonry, J., Dickinson, M., Thompson, R. I., Budavári, T., Casertano, S., Evans, A. S., Filippenko, A. V., Livio, M., Sanders, D. B., Shapley, A. E., Spinrad, H., Steidel, C. C., Stern, D., Surace, J., & Veilleux, S. 2001, ApJ, 560, 49

Ripamonti, E., Haardt, F., Ferrara, A., & Colpi, M. 2002, MNRAS, 334, 401

Roberts, T. P. & Warwick, R. S. 2000, MNRAS, 315, 98

Rubin, V. C., Thonnard, N., & Ford, Jr., W. K. 1980, ApJ, 238, 471

Ruszkowski, M. & Begelman, M. C. 2003, ApJ, 586, 384

Saslaw, W. C., Valtonen, M. J., & Aarseth, S. J. 1974, ApJ, 190, 253

Schaerer, D. 2002, A&A, 382, 28

—. 2003, A&A, 397, 527

Schneider, R., Ferrara, A., Ciardi, B., Ferrari, V., & Matarrese, S. 2000, MNRAS, 317, 385

Schneider, R., Ferrara, A., Natarajan, P., & Omukai, K. 2002, ApJ, 571, 30

Schnittman, J. D. & Buonanno, A. 2007, ApJ, 662, L63

Schödel, R., Ott, T., Genzel, R., Hofmann, R., Lehnert, M., Eckart, A., Mouawad, N., Alexander, T., Reid, M. J., Lenzen, R., Hartung, M., Lacombe, F., Rouan, D., Gendron, E., Rousset, G., Lagrange, A.-M., Brandner, W., Ageorges, N., Lidman, C., Moorwood, A. F. M., Spyromilio, J., Hubin, N., & Menten, K. M. 2002, Nature, 419, 694

Schutz, B. F. & Ricci, F. 2001, in Gravitational Waves, 11–+

Sesana, A., Haardt, F., Madau, P., & Volonteri, M. 2004, ApJ, 611, 623

Sesana, A., Volonteri, M., & Haardt, F. 2007, MNRAS, 377, 1711

Shapiro, S. L. 2004, in Coevolution of Black Holes and Galaxies, ed. L. C. Ho, 103–+

Shapiro, S. L. 2005, ApJ, 620, 59

Sheth, R. K., Mo, H. J., & Tormen, G. 2001, MNRAS, 323, 1

Sigurdsson, S. 2003, Classical and Quantum Gravity, 20, 45

Smith, B. D. & Sigurdsson, S. 2007, ApJ, 661, L5

Smith, B. D., Sigurdsson, S., & Abel, T. 2007, astro-ph/0706.0754

Smoot, G. F., Bennett, C. L., Kogut, A., Wright, E. L., Aymon, J., Boggess, N. W., Cheng, E. S., de Amici, G., Gulkis, S., Hauser, M. G., Hinshaw, G., Jackson, P. D., Janssen, M., Kaita, E., Kelsall, T., Keegstra, P., Lineweaver, C., Loewenstein, K., Lubin, P., Mather, J., Meyer, S. S., Moseley, S. H., Murdock, T., Rokke, L., Silverberg, R. F., Tenorio, L., Weiss, R., & Wilkinson, D. T. 1992, ApJ, 396, L1

Soltan, A. 1982, MNRAS, 200, 115

Spergel, D. N., Bean, R., Doré, O., Nolta, M. R., Bennett, C. L., Dunkley, J., Hinshaw, G., Jarosik, N., Komatsu, E., Page, L., Peiris, H. V., Verde, L., Halpern, M., Hill, R. S., Kogut, A., Limon, M., Meyer, S. S., Odegard, N., Tucker, G. S., Weiland, J. L., Wollack, E., & Wright, E. L. 2007, ApJS, 170, 377

Spergel, D. N. & Steinhardt, P. J. 2000, Physical Review Letters, 84, 3760

Springel, V., White, S. D. M., Tormen, G., & Kauffmann, G. 2001a, MNRAS, 328, 726

Springel, V., Yoshida, N., & White, S. D. M. 2001b, New Astronomy, 6, 79

Stahler, S. W., Palla, F., & Salpeter, E. E. 1986, ApJ, 302, 590

Sugimoto, D., Chikada, Y., Makino, J., Ito, T., Ebisuzaki, T., & Umemura, M. 1990, Nature, 345, 33

Taffoni, G., Mayer, L., Colpi, M., & Governato, F. 2003, MNRAS, 341, 434

Tan, J. C. & McKee, C. F. 2004, ApJ, 603, 383

Tegmark, M., Silk, J., Rees, M. J., Blanchard, A., Abel, T., & Palla, F. 1997, ApJ, 474, 1

Teukolsky, S. A. & Press, W. H. 1974, ApJ, 193, 443

Thorne, K. S. Gravitational radiation (Three Hundred Years of Gravitation), 330–+

Thorne, K. S. 1995a, in New York Academy Sciences Annals, Vol. 759, Seventeeth Texas Symposium on Relativistic Astrophysics and Cosmology, ed. H. Böhringer, G. E. Morfill, & J. E. Trümper, 127–+

Thorne, K. S. 1995b, in Particle and Nuclear Astrophysics and Cosmology in the Next Millenium, ed. E. W. Kolb & R. D. Peccei, 160–+

Tremaine, S., Gebhardt, K., Bender, R., Bower, G., Dressler, A., Faber, S. M., Filippenko, A. V., Green, R., Grillmair, C., Ho, L. C., Kormendy, J., Lauer, T. R., Magorrian, J., Pinkney, J., & Richstone, D. 2002, ApJ, 574, 740

Tumlinson, J., Shull, J. M., & Venkatesan, A. 2003, ApJ, 584, 608

Uehara, H. & Inutsuka, S.-i. 2000, ApJ, 531, L91

Valluri, M., Merritt, D., & Emsellem, E. 2004, ApJ, 602, 66

Vecchio, A., Wickham, E. D., & Stevens, I. R. 2004, in Presented at the Society of Photo-Optical Instrumentation Engineers (SPIE) Conference, Vol. 5500, Gravitational Wave and Particle Astrophysics Detectors. Edited by Hough, James; Sanders, Gary H. Proceedings of the SPIE, Volume 5500, pp. 183-193 (2004)., ed. J. Hough & G. H. Sanders, 183–193

Vine, S. & Sigurdsson, S. 1998, MNRAS, 295, 475

Volonteri, M., Haardt, F., & Madau, P. 2003, ApJ, 582, 559

Volonteri, M. & Rees, M. J. 2005, ApJ, 633, 624

Wang, J.-M., Chen, Y.-M., & Zhang, F. 2006, ApJ, 647, L17

Warren, M. S., Quinn, P. J., Salmon, J. K., & Zurek, W. H. 1992, ApJ, 399, 405

Weinberg, M. D. 1989, MNRAS, 239, 549

White, S. D. M. 1976, MNRAS, 177, 717

—. 1978, MNRAS, 184, 185

—. 1983, ApJ, 274, 53

Willott, C. J., McLure, R. J., & Jarvis, M. J. 2003, ApJ, 587, L15

Wise, J. H. & Abel, T. 2005, ApJ, 629, 615

Wiseman, A. G. 1992, Phys. Rev. D, 46, 1517

Woosley, S. E. & Weaver, T. A. 1995, ApJS, 101, 181

Wyithe, J. S. B. & Loeb, A. 2003, ApJ, 590, 691

Xu, G. 1995, ApJS, 98, 355

Yoo, J. & Miralda-Escudé, J. 2004, ApJ, 614, L25

Yoshida, N., Omukai, K., Hernquist, L., & Abel, T. 2006, ApJ, 652, 6

Yu, Q. 2002, MNRAS, 331, 935

Zezas, A. & Fabbiano, G. 2002, ApJ, 577, 726

Zhao, H., Haehnelt, M. G., & Rees, M. J. 2002, New Astronomy, 7, 385

Zwicky, F. 1933, Helvetica Physica Acta, 6, 110

Vita

Miroslav Micic

Education

The Pennsylvania State University University Park, Pennsylvania, 16802 2001–2007

Ph.D. in Astronomy & Astrophysics, expected in December 2007

Area of Specialization: Numerical Simulations of Structure Formation

Belgrade University Belgrade, Yugoslavia 1995–2000

B.S. in Astrophysics

Awards and Honors

Competitive supercomputer time at Columbia High-End Computing Project 2005–Present
Zaccheus Daniel Foundation for Astronomical Science Grant 2002-2005
Braddock Fellowship 2001-2002

Research Experience

Doctoral Research The Pennsylvania State University 2001–Present

Thesis Advisor: Prof. Steinn Sigurdsson

This research involved obtaining gravitational wave signature from cosmological numerical simulations of black hole merger trees. This research has been funded by the Center for Gravitational Wave Physics at Pennsylvania State University.

Teaching Experience

Teaching Assistant The Pennsylvania State University 2001

A year of teaching ASTR0 011 lab.